ENHANCEMENT OF CORTICAL BONE ABLATION USING ULTRAFAST PULSED LASERS

ENHANCEMENT OF CORTICAL BONE ABLATION USING ULTRAFAST PULSED LASERS

By

FAHAD ALJEKHEDAB, M.Sc., B.Sc.

A Thesis

Submitted to the School of graduate Studies

In Partial Fulfilment of the Requirements for the Degree

Doctor of Philosophy

McMaster University

Doctor of Philosophy (2019) McMaster University

School of Biomedical Engineering Hamilton, Ontario

TITLE: ENHANCEMENT OF CORTICAL BONE ABLATION USING ULTRAFAST PULSED LASERS

Author Fahad Aljekhedab,
M.Sc., B.Sc., King Saud University,
Riyadh, Saudi Arabia

Supervisor Prof. Qiyin Fang
Co-supervisors Prof. Harold Haugen, Assoc. Prof. Greg Wohl

Number of pages xvii, 152

Abstract

The mechanical tools currently used in orthopedic and dental surgery are imprecise and may cause heat damage. Ultrashort pulse lasers are a promising replacement, but their ablation efficiency must be improved. The goal of this thesis was to achieve high ablation efficiency, precision, and minimal collateral damage using an ultrafast laser on bovine hard tissue. This work used two types of lasers: a Ti:Sapphire laser (210 fs, 800 nm, 1 kHz) and a fiber laser (1 ps, 1035 nm, 100 kHz - 1 MHz).

This thesis begins with a review of the literature on laser-tissue interactions and the effect of certain laser parameters on the ablation process. The next section uses a Ti:Sapphire laser and bovine bone to explore the properties of laser-tissue interactions, including ablation threshold and incubation coefficient. Results showed that as the number of incident pulses goes up, ablation threshold goes down. The threshold range went from 1.08 ± 0.15 J/cm^2 at 25 incident pulses to 0.73 ± 0.12 J/cm^2 at 1000 pulses. The incubation coefficient, S, was calculated to be 0.90 ± 0.02.

The relationship between ablation depth and fluence, scanning speed, and number of successive passes was characterized as a first step towards preparing large-cavity with high removal efficiency using a Ti:Sapphire and fiber lasers. Depth increased with fluence and number of passes, but it decreased with scanning speed.

The influence of environmental conditions including air, compressed air flow, still water and flowing water on cavity ablation depth, and rate was investigated using a Ti:Sapphire laser with aim to enhance ablation efficiency. Findings showed that the deepest

cavities and fastest ablation rates were achieved with compressed air flow. Air flow also resulted in the most precise cuts, the smoothest surfaces, and the absence of microcracks. This thesis also used a fiber laser to explore the effect of fluence and repetition rate on removal rate and ablation quality. Results indicated that ablation rate increases with fluence and pulse rate. When the repetition rate exceeded 600 kHz, the laser caused thermal and mechanical damage, indicated by the presence of amorphous carbon. The effect of environmental conditions and laser parameters such as repetition rate provide valuable insights into the ultrafast laser ablation mechanisms for medicine and biology field.

Acknowledgments

I would first like to thank almighty God, who gave me the opportunity and wisdom needed for graduate study.

After that, I sincerely thank my supervisor, Professor Qiyin Fang, for his support, guidance, valuable advice, and encouragement over the past four years. I learned a lot from his ethics, patience, and attention to detail, which allowed me to improve my research and my life as a whole. He also provided the perfect environment for the research involved in this thesis. I am lucky to have a supervisor as great as him. Special thanks to My first co-supervisor professor Harold Haugen for his generous assistance in my experiments. He provided the laboratory and equipment used in this study. When I had questions, he always had time to discuss and solve my seemingly unsolvable problems. My second co-supervisor, Dr. Greg Wohl, has also earned my gratitude for his guidance in the physiological aspects of this project. His constructive comments and insight were immensely helpful. I would also like to thank my supervisor committee, Dr. Munir El-Desouki. he also provided valuable discussion.

I would also like to thank Dr. Wenbin Zhang. He gave me direction during the early stages of this thesis, and the discussions I had with him were always valuable. Two summer students, Jonathan Favero and Ada Iliescu, were a tremendous help in my experiments, as was the technical training and assistance I received from Chris Butcher in the Canadian Center for Electron Microscopy (CCEM). All of you have my thanks.

This thesis could not have happened without the generous funding provided by King Abdulaziz City for Science and Technology (KACST).

Finally, thank you to my loving wife, Rehab, and my two sons, Abdulaziz and Mohammed, for their boundless help and support.

Table of Contents

Contents

List of Figures

List of Tables

List of Abbreviations

CW	Continuous-Wave
HAZ	Heat Affected Zone
Ti:Sapphire	Titanium: Sapphire
SEM	Scanning Electron Microscopy
EDS	Energy Dispersive X-ray Spectroscopy
HA	Hydroxyapatite
Ca	Calcium
P	Phosphate
O	Oxygen
H	Hydrogen
MGP	Matrix Gla-Proteins
CT	Computed Tomography
μa	Absorption coefficient
μs	Scattering coefficient
$I(x)$	Intensity at a distance x from the surface (depth)
I_0	Incident intensity
IR	Infrared
NIR	Near-infrared
Tm:YAG	Thulium: Yttrium-Aluminum-Garnet
Ho:YAG	Holmium: Yttrium-Aluminum-Garnet
Nd:YAG	Neodymium: Yttrium-Aluminum-Garnet
Er:YAG	Erbium: Yttrium-Aluminum-Garnet
PDT	Photodynamic Therapy
τ_r	Thermal relaxation time
UV	Ultraviolet
XeF	Xenon Fluoride
XeCl	Xenon Chloride
KrF	Krypton Fluoride
Nd:YLF	Neodyminum: Yttrium-Lithium-Fluoride
K	the number of photons required for ionization
ArF	Argon Fluoride
Yb:KYW	Ytterbium: Potassium-Yttrium-Tungstate
Ho:YSGG	Holmium: Yttrium-Scandium-Gallium-garnet
Nd:YVO_4	Neodymium: Yttrium-Vanadate-garnet
DPSS	Diode-Pumped Solid State
CPA	Chirped-Pulse Amplifier
FWHM	Full Width Half Maximum
WDM	Wavelength De-Multiplexing
SM	Single Mode
AOM	Acoustic Optical Modulator
f	objective lens focal length

TFP	Thin Film Polarizer
HWP	Half-Wave Plate
ω_o	Spot size
b	Depth of focus
CCD	Charged-Couple Device
BS	Beam Splitter
D	Spot diameter
N.A.	Numerical Aperture
KDP	Potassium Dihydrogen Phosphate
InGaAs	Indium Gallium Arsenide
SHG	Second Harmonic Generation
AREB	Animal Research Ethics Board
CCEM	Canadian Centre for Electron Microscopy
Ra	Average roughness
Rz	Mean peak to valley height of roughness profile
F_o	Peak fluence
F_{th}	Threshold fluences
S	Incubation coefficient
N_{eff}	The effective number of incident pulses on each spot
v	Scanning speed
He-Ne	Helium-Neon
Z_R	Rayleigh length for the objective lens
C	Carbon
EDX	Energy Dispersed X-ray
Er:YSGG	Erbium: Yttrium-Scandium-Gallium-Garnet
Cr:YSGG	Chromium: Yttrium-Scandium-Gallium-Garnet

Chapter 1: Introduction

1.1 Motivation

Many surgical procedures require bones and teeth to be drilled and cut. For example, when a patient has a condylar fracture in their femur, an orthopedic surgeon must create cylindrical holes in the bone so a metal plate can be screwed into place, as shown in Fig. 1a [1]. When a patient has a spinal fracture, the surgeon creates pilot-holes and inserts pedicle screws to achieve a solid spine fusion. The pedicle screws grab onto the spinal segments and act as firm anchor points for an anterior rod, shown in Fig. 1b [2]. Spinal surgery also requires removing bone spurs from the nerve root [3]. Bone lesions or tumors, such as an osteoid osteoma, must be surgically extracted by cutting bone [4]. In knee replacement procedures, the surgeon must create holes so the implant can be screwed into place, as demonstrated in Fig. 1c [5]. Dental implant procedures require drilling to the bone layer, shown in Fig. 1d [6].

At present, hand-held instruments like mechanical saws, diamond drills and carbide drills are used to remove, shape, or cut hard tissue [7-9]. Despite improvements in technology, mechanical instruments are still associated with many complications. The friction caused by drilling and sawing bone tissue generates heat. Mechanical saw blades can raise the temperature of the operated region by 21 ^{o}C [10]. This heat can damage tissue, leading to changes in protein structure and enzyme activity [11]. Bone necrosis and tissue carbonization were observed after using mechanical cutting tools [12]. Oscillating mechanical tools cause significant vibrations in the surrounding target tissue, which may

fracture thin and fragile bones, causing pain and discomfort for the patient [13]. Conventional high-speed cutting tools can also cause severe hemorrhaging [14]. Furthermore, hand instruments may be difficult to control well enough to make linear cuts, a necessity when there are nearby vascular or neural structures. These drawbacks can negatively impact the healing process [15]. Piezoelectric or ultrasonic devices have been available for use in orthopedic surgeries for many years, but they have not yet replaced conventional mechanical cutting tools [16].

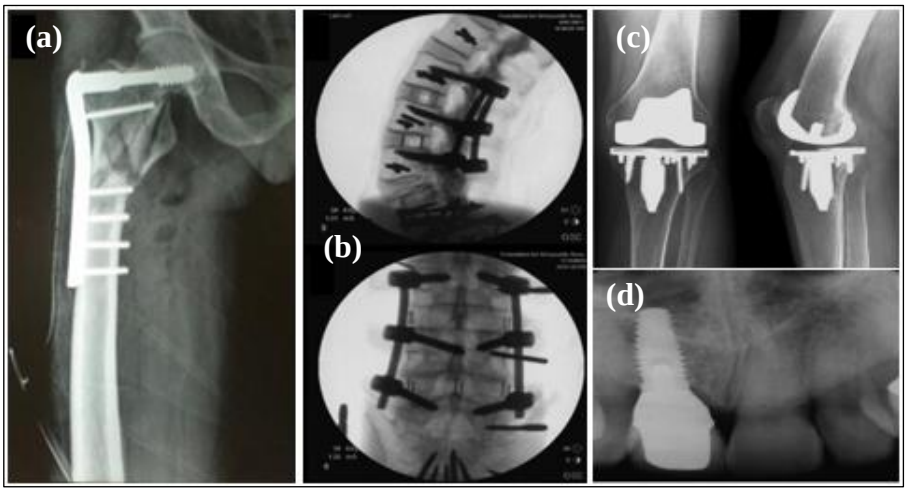

Figure 1: (a) Screws in a proximal femoral bone [1], (b) Spinal stabilization by pedicle screws [2], (c) Knee implant designs with pegs [5], and (d) A hole in the bone layer for inserting an implant [6]. Reprinted with permission from [1, 2, 5, 6]

1.2 Ultrafast laser ablation of bone

Laser ablation is the process of removing material from a target by irradiating it with an intense laser. This technique sidesteps some of the complications of mechanical cutting tools. It allows for precise removal of tissue through non-contact intervention, and it creates minimal mechanical stress [17]. Orthopedic and dental researchers have investigated several types of lasers, continuous wave (CW) and pulse with pulse durations

ranging from milliseconds to femtoseconds [18, 19]. CW and long pulse lasers achieved more precise cuts than mechanical tools, but the lasers' heat diffused beyond the ablation area and into other regions, known the heat affected zone (HAZ), causing thermal damage, shown in Fig. 2a [18]. Shockwaves created microcracks inside the ablated material and propelled molten matter outside the ablation area [20]. These limitations come from the thermal processes governing CW and long pulse lasers.

As the pulse becomes shorter into the picosecond regime, the peak intensity can reach 10^{12}-10^{16} W/cm^2, which would induce plasma-mediated ablation in the beam's focal point [21]. During a single pulse, high electric fields ionize molecules in the ablation area, forming plasma that absorbs incoming laser pulses and heats the tissue to several thousand degrees, quickly removing material from the surface. Due to the short duration limiting the thermal diffusion, the total energy needed to achieve the high temperature is small and confined in the small volume. Hence when it's diffused into surround tissue, the temperature drops very quickly [22]. Thus, ultrashort pulse lasers can precisely remove material with causing minimal tissue damage from heat and shockwaves, as shown in Fig. 2b [23]. A literature review was conducted to better understand tissue-light interaction and the effect of laser pulse duration on the ablation process.

The goal of this study is to learn how different ultrashort laser parameters affect the bone ablation process. The laser's fluence, pulse duration, scanning speed, and number of successive passes affect ablation precision, heat dissipation, and shockwave generation. This study aims to determine ideal laser and processing parameters for achieving optimal

ablation rates. Another goal of this study is to gain a better understanding of properties such as threshold fluence and the incubation coefficient, both of which provide information on how a laser will interact with tissue.

Surgical applications often require a significant amount of material to be removed. It has been shown that ultrafast lasers have low ablation rates [24]. An ultrafast laser's rate mainly depends on laser pulse repetition rate and fluence. High repetition rate and fluence can increase ablation rate. Oscillators and regenerative amplifier configurations are often used to study ultrashort pulse laser ablation. These lasers' repetition rates are limited to the kHz range. Thus, high fluence, 20 times threshold fluence, can be used to increase the ablation rate. During large-scale ablation, such as cavity preparation, ablation debris can reduce ablation rate by absorbing the incident laser beam. Water or air flow may reduce the effects of ablation debris. In this thesis, Ti:Sapphire laser ablation was tested under various environmental conditions using high fluence with the goal of improving ablation efficiency.

Recently, ultrashort fiber lasers with high average power and high repetition rate have been developed [25]. Lasers with these features can perform hard tissue ablation with high efficiency, but these same factors may also cause thermal damage to surrounding tissue. Before ultrashort fiber laser ablation can become a clinical reality, we must learn how parameters such as power and repetition rate affect the bone ablation process. This thesis examines those parameters as well as the effect of water cooling on ultrashort fiber laser ablation. The results of these experiments could make ultrashort lasers a viable replacement for traditional mechanical tools.

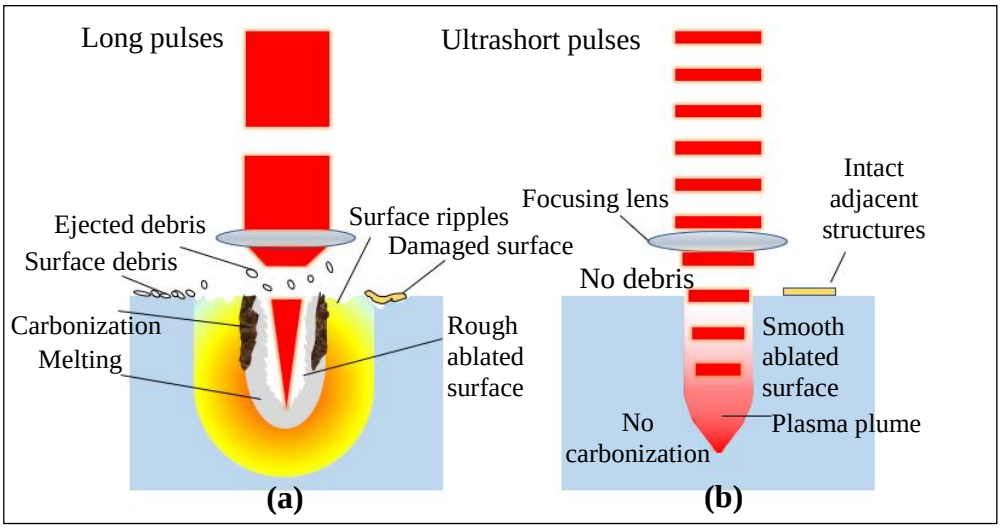

Figure 2: The effect of long (a) and ultrashort (b) pulse duration on the ablation process.

1.3 Organization of the dissertation

Before ultrashort pulse lasers can be used for bone ablation, we must determine the best possible laser and processing parameters, such as laser fluence, repetition rate, and scanning speed, to achieve optimal ablation rates. In this project, the effects of these parameters on ablation rates were investigated using two ultrashort laser systems: Ti:Sapphire and fiber lasers. The thesis is organized as follows:

In Chapter 2, we summarized relevant background information including bone anatomy and physiology at the macroscopic and microscopic levels; optical properties of bone. Section 2 explains the fundamental physics of light propagation into tissue based on its optical properties, such as absorption and scattering. In section 3, the different ablation mechanisms and the laser parameters required to minimize collateral damage are outlined. Section 4 briefly reviews several studies that investigated the use and limitations of long pulse (> 10 ps) and short pulse (< 10 ps) lasers in hard tissue ablation.

In chapter 3, the laser system setups and experimental methods used in this study are described. Section 1 goes over the ultrashort laser systems, including the Ti:Sapphire and fiber lasers. Section 2 and 3 describe the experimental setups of each laser and the characterization procedures of the laser beam, respectively. Section 4 explains how cortical bone samples were prepared. The various characterization methods used in the project, including optical microscopy, infinite focus microscopy, scanning electron microscopy (SEM), Energy dispersive X-ray spectroscopy (EDS), and micro-Raman spectroscopy, are outlined in section 5.

Chapter 4 presents the experimental investigation of Ti:Sapphire laser ablation on cortical bone. In section 1, the ablation threshold of bovine cortical bone is studied at various incident pulse numbers. Section 1 also examines the effect of pulse number on ablation threshold (incubation coefficient), including single-pulse ablation. Section 2 examines the effect of various ablation parameters, such as laser fluence, scanning speed, number of passes, and pulse duration, on the ablation depth. Learning these parameters will make the ablation process as efficient as possible, which was the aim of the next chapter.

In chapter 5, experimental results from large-scale tissue removal procedures using the Ti:Sapphire laser are presented. Chapter 5 examines the effects of various experimental environments on the ablation process, i.e., applying the airflow, putting a layer of water on the bone sample. The goal of these experiments was to increase the rate of tissue removal during ablation. Section 1 describes how scanning different layers in different environments can affect ablation depth and rate. In section 2, SEM is used to learn the

morphology of the ablation cavities, including cut geometry, roughness, and cavity shape. Section 3 examines the thermal effect of laser ablation on bone samples using micro-Raman spectroscopy.

In Chapter 6, we studied bone ablation with a picosecond fiber laser at different laser and processing parameters. Laser ablation depth is affected by various parameters, including as beam spot size, repetition rate, scanning speed, and passing number, each of which was studied in Sections 2, 3, 4, and 5 respectively.

The aforementioned parameters were used to improve the ablation process in chapter 7, which covers the effect of fiber laser fluence and pulse repetition rate on cavity preparation. Section 1 describes the ablation rate as a function of fluence at various repetition rates. Surface morphology was investigated using SEM and infinite focus microscopy. EDS and micro-Raman spectroscopy were also used to examine the thermal effect of laser ablation. Section 2 demonstrates the effects of a layer of water on ablation rate and cavity morphology. Collateral effects, such as thermal and mechanical damage, were also evaluated.

In chapter 8, the major conclusions of this project are summarized, and future directions for further research in ultrashort laser ablation of hard tissue are briefly outlined.

1.4 Contributions

The latest ultrashort fiber lasers have high power and repetition rates, making them well-suited for hard tissue ablation. Indeed, some studies have used this new technology to ablate hard tissue. However, several questions remain before lasers can be used safely and

effectively in dental and medical procedures. Laser ablation can cause thermal and mechanical damage to surrounding tissue, beside long machining time. The literature review including several studies on the relationship between pulse duration and the ablation process will help future researchers discover new ways to improve ablation efficiency while minimizing damage.

The ultrashort laser bone ablation properties, such as threshold fluence and the incubation coefficient, are important considerations when ablating hard tissue. The determination of these properties will help to develop knowledge of laser and material interaction required for this technology to become a clinical reality. The same is true of laser fluence, scanning speed, pulse duration, repetition rate and the number of successive passes. With the right parameters, an ultrashort laser system can ablate tissue with precision and minimal collateral damage. Several experiments were conducted in this thesis to find the best possible laser parameters. In every experiment, a Ti:Sapphire and fiber laser systems were used to ablate samples of bovine cortical bone.

Before ultrashort pulse lasers can be used in practice, their ablation rates must be improved. This study found that when airflow is applied to the removal area, the laser's ablation rate becomes faster by 1.6 and 2 times compared to only air and water conditions, respectively. Also, high fluence and repetition rate can help to enhance ablation efficiency. Clear improvement of ablation rate, about four times, was observed when high fluence (~10 F_{th}) was applied than ablation near the threshold. Faster ablation rate, 1.5 times, was achieved at higher repetition rate, 600 kHz, compared to 100 kHz. These findings will have

positive impact on future micromachining processes not only in the medical and dental fields but also for any micromachining technology required high ablation rate with minimal collateral damage.

Chapter 2: Background

2.1 Bone histology

Bones are an important part of the skeletal system. They have significant mechanical, synthetic, and metabolic functions. Bones protect delicate organs, such as the heart and brain, and their rigid structure serves as the foundation of the human body and provides load support. Bones come in many shapes and sizes, but all bones have organic and inorganic components. The organic components give bones their resilience, while the inorganic components give bones their hardness. Bones contain bone marrow, which is made of hematopoietic stem cells that produce blood cells. They also store important minerals, such as calcium and phosphorus, as well as some fats. Bone tissue has a complex internal and external structure on the macroscopic and microscopic levels. The tissue's structure and composition determine its optical properties, which in turn affect light interaction with the tissue and thus laser ablation process.

2.1.1 Bone anatomy

Bones usually have a layered structure with two types, each with its own microstructure and porosity. Cortical bone usually found on the outer layer, also called compact bone, is dense and solid. It is filled with organic materials and inorganic salts, leaving tiny spaces (5 to 10%) for a porosity. Cortical bone makes up 80% of the total skeletal mass of the human body; the remainder (20%) consists of cancellous bone comprising the bone's internal tissue, also known as trabecular or spongy bone. Cancellous bone is far more porous (50-90%) [26] thanks to its spongy structure. The medullary cavity inside of cancellous bone contains many empty spaces. Most human bones contain both

cortical and cancellous bone. Cortical bone is the main component of long bones, such as the arm and leg bones, which need to be strong and rigid. Cortical bone gives the bone's outer shell a smooth, white, solid appearance. Cancellous bone is more flexible than cortical bone and is usually located at the ends of long bones, surrounded by a thin shell of cortical bone [27].

As with all biological tissues, cortical and cancellous bones are made of several structures that can be arranged in a hierarchy of various structural levels [28]. The first unit of the cortical bone hierarchy is the osteon, also known as the Haversian system, a macrostructure illustrated in Fig. 3. Osteons contain osteocytes, which are arranged in concentric tissue layers, called lamellae, around the Haversian canal. The central canal consists of blood vessels that carry blood to and from the Haversian systems. Central canals are several millimeters long and 0.5 mm in diameter, and they generally run parallel to the bone's surface [29]. In the nanostructure (Fig. 3), Lamellae are comprised of fibers made from collagen, organic proteins, and inorganic proteins. These fibers are appropriately named collagen fibers. In the internal tissue, the first unit in the cancellous bone hierarchy is the trabecula, which does not contain blood vessels. Trabeculae contain red bone marrow, where all blood cells are made [30]. The trabeculae also contain lamellae, which are also made of collagen fibers. These lamellae are arranged longitudinally along the length of the trabeculae. In the nanostructure, cancellous bone comprises the same components of cortical bone.

2.1.2 Bone physiology

Bone tissue is made of three types of cells, all of which begin with "Osteo," the Greek word for bone. Osteoblast cells play a critical role in the maintenance, repair, and remodeling of human bones. They are large cells capable of dissolving and rebuilding bone tissue using a protein mixture called osteoid, which turns into bone through mineralization [31]. Osteoblasts come from red bone marrow, and they can be found on the surface of osteon seams. Osteocytes are the most common bone tissue cell. They are responsible for molecular synthesis and modification, and they transmit signals to the nervous system via glutamate transporters. Experiments show that the destruction of osteocytes results in reduced bone formation, loss of cancellous bone, and increased bone resorption [32]. Osteocytes and their associated processes are located inside spaces known lacunae. Osteoclasts play an important role in calcium homeostasis [27]. They are also responsible for the process of bone resorption, where bone tissue is broken down and transferred elsewhere. Osteoclasts are large cells with five nuclei, and they can be found inside resorption bays, which are pits in the bone surface.

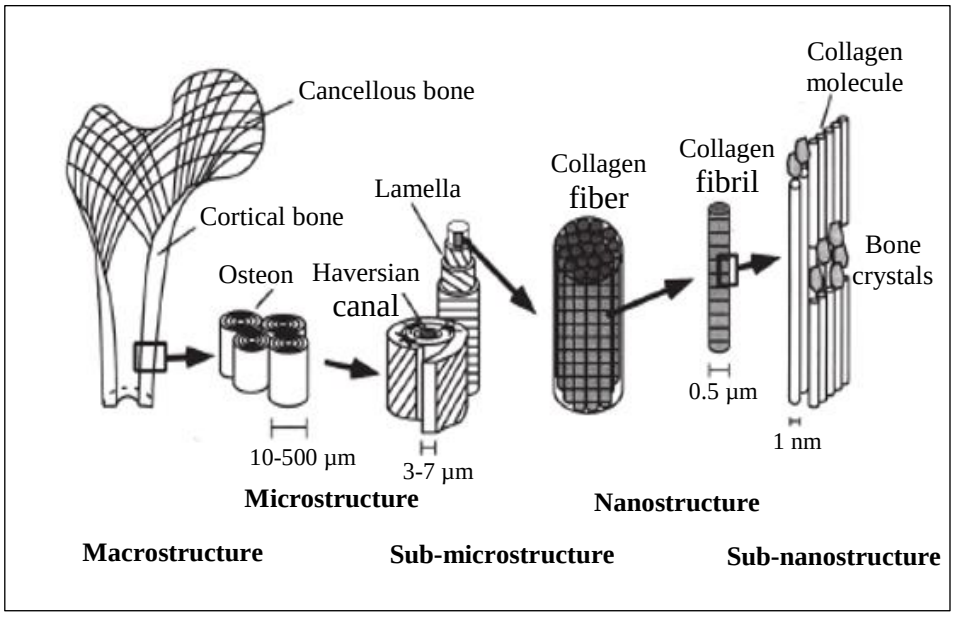

Figure 3: The hierarchical structure of human bone [33]. Reprinted with permission from [33]

2.1.3 Bone composition

Cortical and trabecular bone tissues are biologically identical. They consist of inorganic salts and organic matrices [29]. By weight, roughly 70% of bone is made of inorganic components, and 30% is made of organic materials. Inorganic and organic components comprise 65 and 35% of bone volume respectively [34]. Inorganic components include crystalline hydroxyapatite (50% of total bone mass), water, carbonates, and phosphates; the last three have inorganic salt weights of 20, 5, and 1% respectively [35, 36]. The organic matrix primarily consists of collagen (90% of total organic bone mass), non-collagenous proteins, lipids, and proteoglycan. Table 1 summarizes the composition of human bone.

The inorganic component of bone is primarily made of calcium and phosphate complexes that form hydroxyapatite crystals (HA), giving bone its compressive strength.

These crystals have a small plate shape (20-50 nm long, 15 nm wide, and 2-5 nm thick) and chemical formula of $Ca_{10}(PO_4)_6(OH)_2$ [37]. The crystal possesses a calcium to phosphate (Ca:P) ratio between 1.3 and 2 (per weight) [38]. The ratio changes over time due to gradual fluctuations in the matrix composition, which are subject to nutrition and biomineralization [38]. The HA crystals may contain impurities, such as carbonate replacing phosphate groups [39]. Trace minerals including magnesium, potassium, sodium, and strontium can be found in place of calcium ions [40]. Chloride and fluoride sometimes replace the hydroxy1 groups [41]. Bone strength and quality come from mineral inorganic phase containing Ca^{2+}, PO_4^{3-}, and OH^- ions in hard tissues [42]. Impurities decrease bone resorption due to reduced solubility [42].

Calcium (Ca) and phosphate (P) have more Z elements than other components of inorganic bone salts. The most abundant cation in the body is calcium, which is released into the body through bone resorption. Roughly 99% of the human body's calcium is inside bone mineral phase. Extracellular and intracellular fluids contain the rest. A similarly high percentage (85%) of the body's phosphate can be found in bone mineral phase. Calcium and phosphorous interact during several essential processes into the body due to various physicochemical factors [43]. The Ca:P ratio is therefore a suitable biomarker for bone metabolism, growth, development, and mineral homeostasis [44].

The organic component of bone largely contains type I collagen (90%) and non-collagenous proteins (10%). Fibers made of type I collagen are, on average, 300 nm long and 1.5 nm in diameter [45]. Type I collagen has a triple helical structure comprising three

polypeptide chains, each of which contain 1050 amino acids. These chains are known as alpha chains. There are two α1(I) chains and one α2(I) chain per structure [45]. Type I collagen's triple-helical structure comes from glycine, proline, and hydroxyproline. Glycine's side chain consists of a single hydrogen atom that fits into the center of the triple helix. Hydrogen bonds cross-link with hydroxyproline and other charged residues to form linear molecules that gather in parallel to one-another, eventually producing collagen fibers, which give bones their tensile strength [46]. Non-collagenous proteins contain proteoglycans, phosphoproteins, glycoproteins, and matrix Gla-proteins (MGP) [47].

To investigate the change of bone components that may result from laser ablation, several techniques have been used, including synchrotron radiation micro-CT [48], inductively coupled plasma optical emission spectroscopy [49], chemical analysis [50], solid-state nuclear magnetic resonance [51] and Raman spectroscopy [52], as well as a variety of X-ray methods, such as X-ray diffraction [47], small-angle X-ray scattering [53], X-ray fluorescence [54], and energy dispersive X-ray analysis [55].

Table 1: Main components of bone

Type of material	Bone component	Percentage
Inorganic	hydroxyapatite	50%
	water	20%
	carbonates	5%
	phosphates	1%
Organic	collagen	20%
	non-collagenous proteins	2%

2.2 Light propagation in tissues

Interactions between light and tissue are affected by the properties of both [56]. Both types of properties are important to consider when studying laser ablation, as they affect the propagation of light through tissue. Understanding the optical properties of tissue

can lead to the development of ablation strategies with greater efficiency and reduced thermal effects. Photons propagate through tissue in all directions and may be scattered or absorbed by tissues of various sizes (10s nm to 100s μm) [57]. The photons' behavior is chiefly determined by two optical properties of the tissue: the absorption coefficient (μ_a) and the scattering coefficient (μ_s). Knowledge of these coefficients will help determine the ideal laser parameters for precise ablation. Several methods have been used to determine the above-mentioned optical coefficients, such as the measurement and analysis of laser-induced mechanical and thermal transients [58, 59]. Several overviews of the effects of light-tissue interactions, including reflection, absorption, and scattering, are provided below.

2.2.1 Reflection

Reflection occurs when electromagnetic radiation comes back from the tissue it irradiates. The reflecting surface acts as a physical boundary between the tissue and the surrounding air. There are two types of reflection: specular and diffuse. When the tissue's surface has small irregularities compared to the incident light wavelength, specular reflection occurs. When the surface is rough, it causes diffuse reflection. Diffuse reflectance is common among biological tissues, and it plays significant role when transparent tissues, such as those of the cornea, are irradiated. Reflection has a negligible effect on the laser ablation process compared to absorption and scattering [35].

2.2.2 Absorption

Several factors can affect the ability of biological tissue to absorb laser light. These factors include the electronic constitution of the tissue's atoms and molecules, the wavelength of laser beam, the thickness of the absorbing tissue layer, and internal properties such as tissue concentration and temperature absorbing agents. Optical absorption can be quantified using Lambert's law, expressed in the following equation [35]:

$$\boldsymbol{I(x) = I_0\, e^{-\mu_a x}} \quad (1)$$

where $\boldsymbol{x}$ denotes the optical axis, $I(x)$ is the intensity at a distance $\boldsymbol{x}$ from the surface (depth), I_0 is the incident intensity, and μ_a is the absorption coefficient, which is measured in reciprocal centimeters (cm^{-1}). In the depth of $1/\mu_a$ from surface as known absorption length, the light (at least 63% of it) is absorbed [60].

The optical absorption properties of tissue are expressed by the absorption coefficient (μ_a). When the absorption coefficient is above 500 cm^{-1}, it is considered strong. The main absorbers of light in biological tissues are water molecules and macromolecules, including proteins and pigments, whose absorption coefficients changed based on the wavelength of the light [35]. In the hard tissue, the dominant chromophores for laser are water, collagen, and minerals, all of which form the main components of bone.

Water comprises 60-80% of biological tissue. Its absorption coefficient greatly affects the depth at which light can penetrate tissue, making it an important factor to consider when performing laser ablation [60]. As shown in Fig. 4, water molecules mainly contribute to absorption of light in the IR spectrum. Water's absorption coefficient

increases rapidly when the wavelength of light increases from 800 nm ($\mu_a \approx 0.1$ cm^{-1}) to 2940 nm ($\mu_a \approx 12000$ cm^{-1}). Water is far better at absorbing NIR light than other components of hard tissue [61]. It also shows a high absorption coefficient in the middle and far infrared wavelengths. At wavelengths of 6.1 μm, water absorption coefficient reaches 2740 cm^{-1}. Organic components of bone, such as collagen fibrils, have absorption peaks at 6.1, 6.5, and 7.9 μm. Collagen's absorption coefficient is double that of water when exposed to light with a 6.1 μm wavelength [61]. The mineral components of hard tissue, such as calcium and phosphate apatite, have several absorption peaks between 3.1 and 11.1 μm [62].

The chief absorber of visible light is melanin, with an absorption coefficient of 1000 cm^{-1} in the visible spectrum, as illustrated in Fig. 4. Proteins also mainly absorb light in the visible range. Melanin and proteins also have high absorption coefficients in the ultraviolet range, whereas water has a negligible absorption coefficient in the visible and ultraviolet (180-400 nm) spectra. At wavelengths of ≤ 170 nm, water absorbs 100 times more than at longer wavelengths (240-290 nm) [61].

The absorption coefficient of bone is determined by its main chromophores. Different components of bone can have drastically different absorption components at various wavelengths. Table. 2 shows the absorption coefficient of three main bone components at different laser wavelengths [61]. When a CO_2 laser with a 10.6 μm wavelength is used, hydroxyapatite becomes the main absorber, with an absorption coefficient of μ_a = 3475 cm^{-1}. Water and collagen have lower absorption coefficients at μ_a = 817 and 222 cm^{-1} respectively. The same laser with a wavelength of 9.5 μm elicits a

higher absorption coefficient from collagen (μ_a = 560 cm^{-1}) and an even greater absorption coefficient from hydroxyapatite μ_a = 5494 cm^{-1} [63]. When exposed to an erbium laser (2.94 µm), water's absorption coefficient is 11850 cm^{-1}, while collagen and minerals have absorption coefficients of μ_a = 1330 and 648 cm^{-1} respectively. Lasers with wavelengths of about 2 µm, such as the Tm:YAG (2 µm) and Ho:YAG (2.12 µm) lasers, induce high absorption coefficients in water molecules, as do lasers in the 10 µm range, such as CO_2 lasers [64].

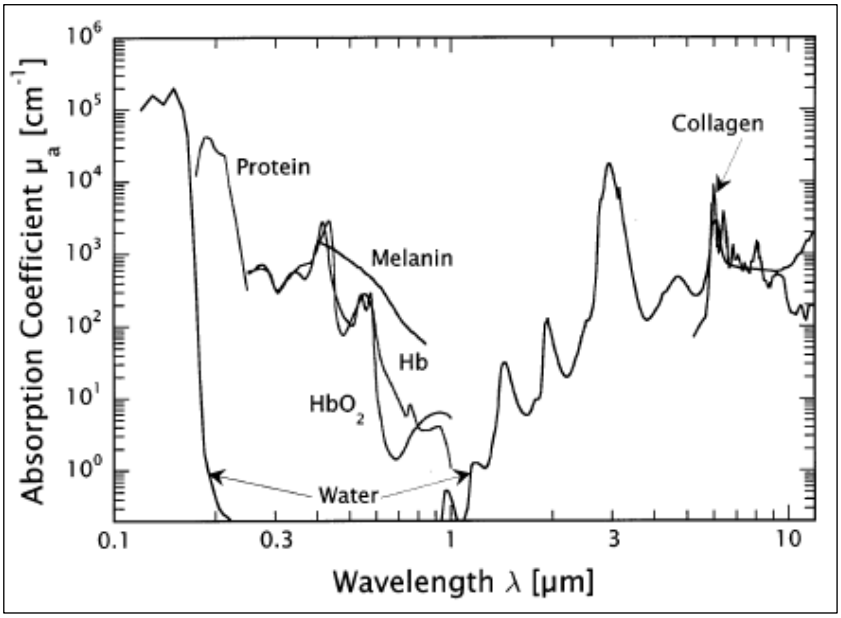

Figure 4: Optical absorption coefficients of biological tissue chromophores [61]. Reprinted with permission from [61]

Table 2: Absorption coefficient of main bone components at various laser wavelengths

Bone components	Absorption coefficient (cm^{-1})				
	Diode 0.98 µm	Nd:YAG 1.064 µm	Er:YAG 2.94 µm	CO_2 9.6 µm	CO_2 10.6 µm
Hydroxyapatite	1.2	1.2	648	5494	3475
Collagen	0.37	0.29	1330	560	222
Water	0.48	0.14	11850	817	817

2.2.3 Scattering

Scattering occurs when photons change direction from a straight trajectory. There are two types of scattering: elastic and inelastic. When particles in a medium are smaller than the incident light's wavelength, the scattered photons will have roughly the same wavelength as the incident light. This is called elastic scattering. A special type of elastic scattering, called Rayleigh scattering, is inversely proportional to the fourth power of the wavelength [35]. Inelastic scattering happens when energy is transferred between the incident light and the medium through which it passes, resulting in scattered light with a different wavelength from the incident light. Lasers with long wavelengths are used to penetrate deep into biological tissue, where inelastic scattering can occur.

The direction light propagates through a material is governed by the orientation of the material's components. Collagen fibrils in bone are oriented in a way that scatters light in many directions. This can cause unwanted redistribution of a laser beam's energy [65]. The same bones from different animals often have different scattering coefficient. The human skull has a scattering coefficient of 25-18 mm^{-1} at wavelengths of 650-950 nm [66], while a pig's skull has a scattering coefficient of 35-27 mm^{-1} at the same range of wavelengths [65]. The same type of bone from the same animal can also have different scattering coefficients. For example, mineralized tissue in a pig's skull bone has a higher scattering coefficient than unmineralized tissue [67]. A material's scattering coefficient is inversely proportional to the wavelength of the incident light. Visible light produces high scattering coefficients, so the laser beam's wavelength must be carefully considered to minimize scattering during laser ablation.

The scattering and absorption coefficients of hard tissue are greatly affected by changes in temperature [35]. In experiments, the absorption coefficient of water exposed to holmium (2.1 μm) and thulium (2.14 μm) laser radiation dropped sharply (63%) when the temperature increased from 20 to 100 ^{0}C [68]. Bone sample preparation processes such as dehydration can also affect these coefficients [69].

2.3 Laser-tissue interaction mechanisms

Many interactions occur when biological tissue is exposed to a laser beam. These interactions change based on the properties of the laser and tissue. The optical properties of tissue components, such as absorption and scattering coefficients, determine the total transmission of the tissue at certain wavelengths. Laser parameters, such as wavelength, pulse duration, repetition rate, applied energy, spot size, and power density, govern the types of interactions that take place. There are five types of interactions affected by the exposure time and power density of the laser beam: photochemical interaction, thermal interaction, photoablation, photodisruption, and plasma-induced ablation, all shown in Fig. 5 [35].

The graph below shows the effects of power densities between 1 and 1000 J/cm^2, a considerably smaller range than the fifteen orders of magnitude of exposure time. This time scale can be divided into several sections, each of which produces a different interaction. First section (>1 s) produces photochemical interactions. The second section (1 s to 1 μs) produces thermal interactions. The third (1 μs to 1 ns) causes photoablation. The fourth (<1 ns) results in photodisruption and plasma-induced ablation. Interactions in nearby sections

can occur simultaneously. For example, photochemical interactions and thermal effects can happen at the same time. Thermal effects and plasma-induced ablation were both observed during laser ablation with ultrashort laser pulses and high repetition rates [35]. These interactions occur most frequently during laser ablation of hard tissues. They will both be discussed later in this chapter.

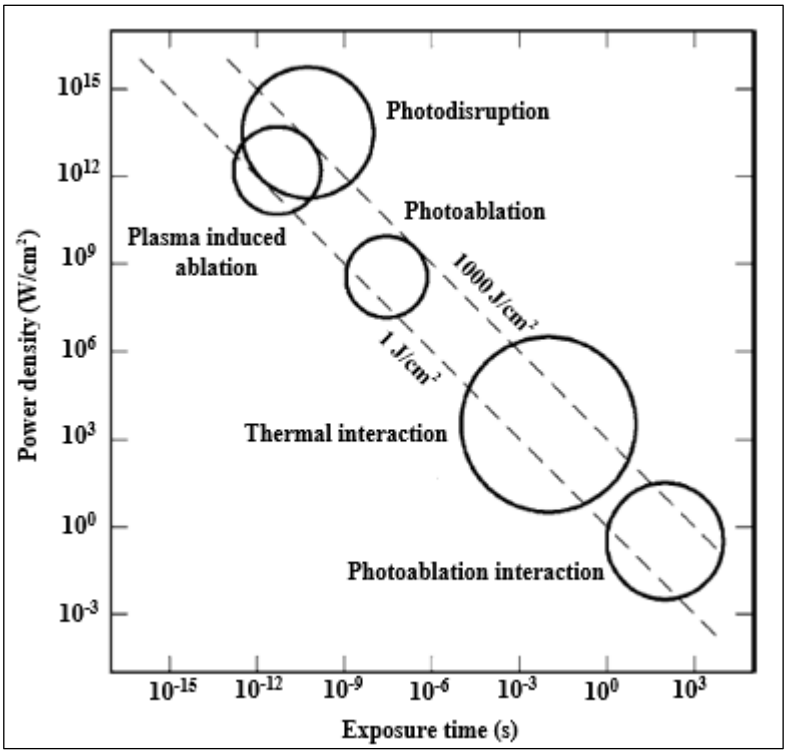

Figure 5: Graph of laser-tissue interactions. The 1 J/cm^2 and 1000 J/cm^2 energy density lines are used to demonstrate the energy density range of each interaction [35]. Reprinted with permission from [35].

2.3.1 Photochemical interaction

Photochemical interactions take place at very low power densities (≤1 W/cm^2) and during long exposure times (seconds to CW). During photochemical interactions, light induces chemical effects and reactions within biological tissues. When photons excite molecules or atoms, they can cause bond breakage, resulting in ablative photochemical

decomposition [35]. When the power density exceeds the threshold irradiance, the bond dissociation rate exceeds the recombination rate, and tissue can be removed [70]. Photochemical interactions have therapeutic applications, such as photodynamic therapy (PDT) for cancer, as well as low-level laser therapy (LLLT) for healing wounds [71]. Lasers with visible wavelengths, such as rhodamine dye lasers (630 nm) or ultraviolet lasers, achieve high optical penetration depths in tissue, making them well-suited for causing photochemical interactions [72].

2.3.2 Photothermal interaction

In photothermal interactions, photons are absorbed by tissue and converted into thermal energy, raising the local temperature of the tissue. The rise in temperature is determined by the wavelength, exposure time, and power density of the laser beam, as well as the properties of the tissue. Thermal effects can be induced by continuous wave or pulsed laser radiation (>1 μs) with power density of $10\text{-}10^6$ W/cm^2. Thermal mechanism is controlled by the peak value of temperature which can cause tissue coagulation to vaporization [35].

Thermal mechanisms occur in several steps: heat generation, heat transport, heat effects, and tissue damage, as shown in Fig. 6. The exposure time and power density of the laser beam determine the amount of heat generated, as does the absorption coefficient of the tissue. The high absorption coefficient of tissue will induce a thermal effect. The main components of hard tissue (water, collagen, and minerals) preferentially absorb laser radiation in the IR spectrum, such as CO_2 (10.6 μm), Er:YAG (2.94 μm), and Nd:YAG

(1.06 μm) lasers, making these lasers well-suited for causing thermal effects. At a microscopic level, photothermal effects occur in molecular vibration-rotation bands that absorb photon energy and transform it into thermal energy. This process excites the molecule, causing inelastic collisions with other molecules nearby. The resulting non-radiative decay leads to an increase in the kinetic energy and temperature of the medium [35].

During heat transport, photon energy is redistributed throughout the tissue in a process called thermal diffusion. Heat transport is governed by the tissue's thermal relaxation time (τ_r), the amount of time needed to reduce the tissue's local peak temperature by 63% [73]. When the pulse duration is longer than the tissue's thermal relaxation time, thermal energy diffuses beyond the tissue's optical penetration depth and causes undesirable thermal damage to surrounding tissues. Lasers with shorter pulse durations cause minimal thermal damage. Water has a thermal relaxation time of about 1 μs [74], so lasers with a pulse duration of <1 μs cause minimal thermal damage to human biological tissue, which is 70% water. However, these lasers with high repetition rates have been shown to generate heat more quickly than it can be transported through the tissue, causing severe thermal damage [75].

Heat effects are determined by the highest temperature reached by the tissue, as well as the amount of time the tissue spends at this temperature before thermal relaxation occurs. Thermal effects can cause different kinds of tissue damage, including coagulation, vaporization, carbonization, and melting, as shown in Fig. 6 [71]. If the tissue reaches 60

^{o}C, collagen and protein denaturation occurs, resulting in cell necrosis, tissue coagulation, and darkening of the surrounding tissues. At 100 ^{o}C, water in the tissue starts to boil, creating high pressure and micro-explosions inside the tissue. As pressure increases, the bubbles will grow enough to overcome surface tension, creating shock waves and ejecting heated material. Vaporization is considered a thermomechanical effect because it causes mechanical ruptures in the tissue [76]. Above 100 ^{o}C, the tissue starts to carbonize and generate smoke, blackening the surrounding tissues. Laser ablation should never result in carbonization, because lower temperatures already necrotize the tissue. At 300 ^{o}C, the tissue melts, creating fractures and gas bubbles [35].

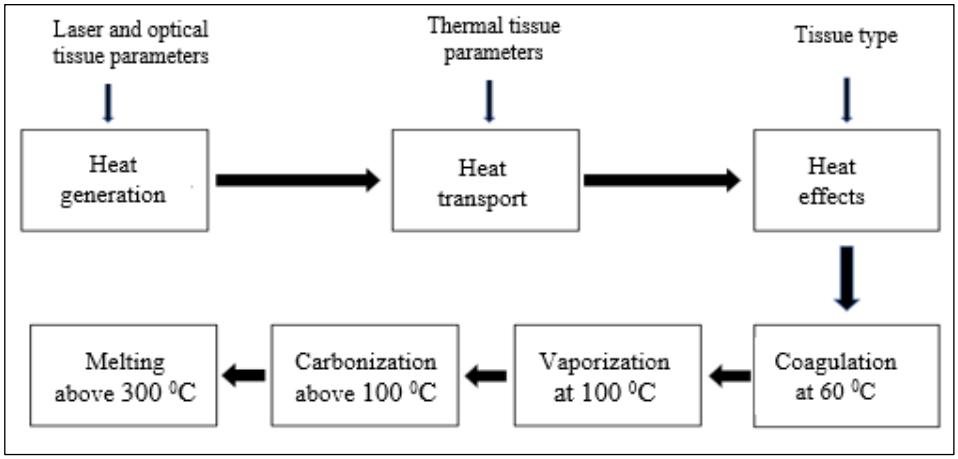

Figure 6: The steps of thermal interaction: heat generation, heat transport, heat effects, and tissue damage.

2.3.3 Photoablation

Photoablation is caused by lasers with power densities of 10^{7}-10^{10} W/cm^{2} and pulse durations in the nanosecond range. During photoablation, photon energy electronically excites molecules in the tissue, breaking the chemical bonds that hold the molecules together. When the molecules dissociate, fragments escape from the material's surface [35].

To break molecular bonds, the laser must produce photons of energy greater than the amount of chemical energy holding the molecules together. UV wavelength lasers, such as excimer lasers (XeF at 351 nm, XeCl at 308 nm, and KrF at 248 nm), are suitable for tissue photoablation [77]. This laser has a shorter pulse duration (nanosecond range) than the thermal relaxation time of the tissue (measured in microseconds), allowing it to precisely remove material with minimal carbonizing or melting surrounding tissues. However, there is a drawback: UV radiation is toxic to cells [35].

2.3.4 Photodisruption ablation

High-energy laser pulses (10^{11}-10^{16} W/cm^2) create plasmas when interacting with tissue. The plasma electrons diffuse away from the beam's focal point and into surrounding tissue, creating shock waves that extend beyond the plasma boundary. When soft tissues are exposed to high-energy lasers, tensile stresses in the tissue's liquid environment create cavitation. When the bubbles burst, they release high-speed jets of liquid that can damage nearby tissue. These mechanical effects are the result of plasma-induced ablation, and they comprise the process of photodisruption.

When material is removed without vaporizing tissue, it is referred to as cold ablation. Photomechanical ablation requires less energy than photothermal mechanisms. A Nd:YAG laser (pulse duration of 15 ns to 100 μs) can remove material with less energy than it takes to boil the liquid inside the tissue [78]. Several laser systems, such as the Nd:YLF laser (pulse duration of 100s of ns), are needed to use this ablation technique.

2.3.5 Plasma-mediated ablation

This type of ablation is also known as laser-induced optical breakdown. When the tissue's surface is exposed to an intense electric field exceeding the Coulomb electric fields (10^7 V/cm) of the atoms or molecules in the tissue, they will be ionized, forming plasma and inducing optical breakdown [35]. The effectiveness of this technique depends on the strength of the electric field, which is determined by the power density of the laser. A high intensity of laser (10^{11} W/cm^2) can produce the intense electric field needed for optical breakdown. As mentioned earlier, standard laser ablation is determined by linear photon absorption and thermal effects. In plasma-induced ablation, the plasma formation cannot be induced by linear absorption, because photon energy by itself cannot ionize an electron [79]. Plasma generation is achieved through nonlinear absorption by two mechanisms: Q-switched and mode-locked laser pulses. Q-switched pulses in the nanosecond range can heat the tissue to more than 1000 K, resulting in thermal ionization (thermionic emission) with nonionizing side effects. Mode-locked laser pulses in the picosecond and femtosecond range produce such a high intensity of photons that the tissue can absorb two or more photons simultaneously, providing energy for ionization (multiphoton ionization). The multiphoton ionization rate is proportional to I^k, where I is the laser intensity, and k is the number of photons required for ionization [61]. Ultrashort pulse lasers (ps to fs) have a lower threshold for plasma formation than short pulse lasers (ns). To summarize, ultrashort laser systems (500 ps to 100 fs) with high power density (10^{11}-10^{13} W/cm^2) are used for plasma mediated ablation.

Multiphoton absorption or electron tunneling ionization excite bound electrons to the material's conduction band, a phenomenon referred to as multiphoton ionization, demonstrated in Fig. 7. This electron acts as a "seed" for two other processes: inverse bremsstrahlung and avalanche ionization. During inverse bremsstrahlung, the free electron in the conduction band can linearly absorb incoming photons and accelerate to higher energy states within the same band [61]. The electron continues to gain kinetic energy until it exceeds the conduction band energy, at which point it collides with and ionizes a nearby molecule, freeing another electron (impact ionization). These two free electrons, each with less individual energy, absorb more incoming photons, accelerate, and strike other molecules, releasing two additional electrons and eventually forming plasma. This process is referred to as avalanche ionization.

Fig. 7 illustrates multiphoton ionization and avalanche ionization. These processes repeat many times over a few picoseconds, generating plasma with a high free electron density of $>10^{21}$ electrons/cm^3 [80]. At this point, the incident laser photons can be observed by electrons via free-carrier absorption, rapidly increasing the temperature of the plasma and electrons to several thousand Kelvin [81]. Hot plasma expands outward (hydrodynamic expansion), forming cavitation bubbles that send shockwaves through surrounding tissue. These shockwaves contribute to ablation through mechanical disruption [82]. The extremely hot plasma vaporizes tissue in the laser's focal area, resulting in successful ablation [83].

Plasma-mediated ablation transfers photon energy to mechanical energy with up to 90% efficiency, as observed Vogel and Venugopalan in bulk water [61]. This efficient transfer of energy results in clean, precise ablation with minimal collateral thermal and mechanical effects, but only if the suitable laser parameters are used. The size of the affected region is determined by the amount of laser energy going into the tissue. Collateral damage can be avoided by minimizing the deposited energy and maintaining a sufficiently high laser intensity.

Because plasma has a high absorption coefficient, plasma-mediated ablation can be used on tissues that are transparent or weakly absorbing laser beam. When plasma builds up, it shields the target area against additional laser photons in a process known as plasma shielding. The resulting decrease in ablation efficiency can be observed over time [35].

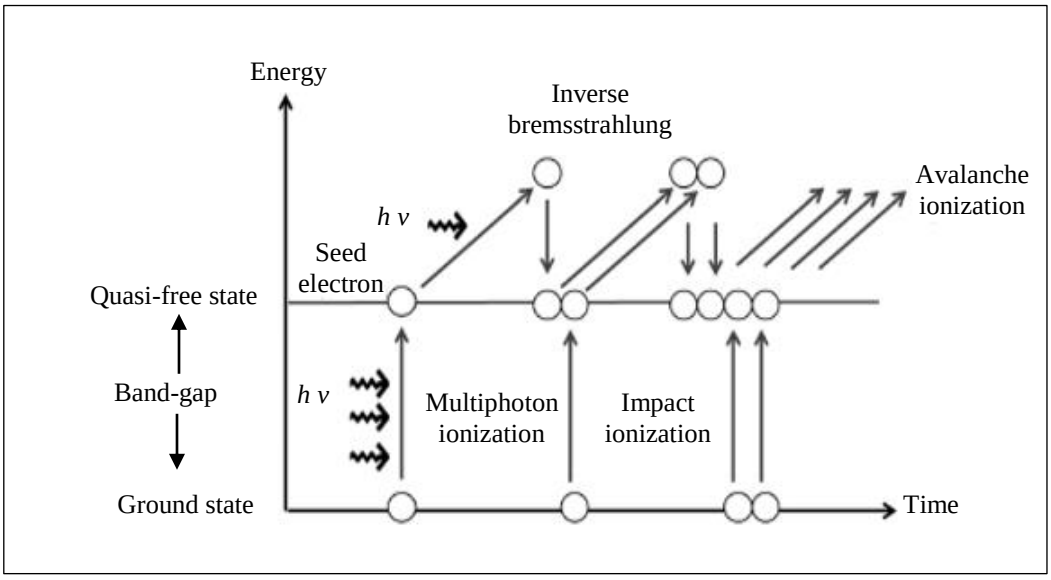

Figure 7: The process of plasma-mediated ablation, including multiphoton ionization and avalanche ionization [61]. Reprinted with permission from [61]

2.4 Previous works of hard tissue laser ablation

In numerous orthopaedic and dental procedures, mechanical tools such as carbide and low-speed diamond drills, oscillating saws, and ultrasonic cutters are used to remove, shape, or cut hard tissues. While these mechanical tools have high ablation rates, they pose significant drawbacks. For example, they can cause significant mechanical vibrations in tissue, leading to excessive material loss and intense pain [84]. Mechanical instruments are also reported to cause severe thermal damage to adjacent tissue, resulting in cell death and delayed healing [85, 86]. Because these devices are difficult to control, they can cause undesirable nonlinear cuts. Laser ablation can overcome many of these limitations. Several types of lasers with various wavelengths and pulse durations have been investigated for ablation.

In 1964, Stern and Sognnaes performed hard tissue laser ablation for the first time, with Goldman et al. following suit the same year [87, 88]. They used a pulsed ruby laser (λ = 694 μm) to study the effects of a laser beam on dental hard tissues. The researchers observed severe collateral thermal damage and tooth cracking. As a result, these studies have not gained clinical relevance. Since then, other types of lasers have been evaluated for hard tissue ablation. These lasers include mid-infrared lasers such as CO_2 lasers (λ = 10.6 μm), near-infrared lasers such as Nd:YAG (λ = 1.064 μm), and UV lasers such as excimer lasers. This section of the chapter provides an overview of the long pulse (> 10 ps) and short pulse (< 10 ps) lasers that have been used over the years, including their strengths and weaknesses.

2.4.1 Long pulse lasers (> 10 ps)

- CO_2 laser

Hydroxyapatite, the main component of hard tissue, highly absorbs CO_2 laser photons (wavelength of 9-11 μm), requiring only tens of watts of power to remove material. The absorbed photon energy is converted to thermal energy, and the resulting thermal interactions cause hydroxyapatite to melt. For this reason, CO_2 lasers were considered for hard tissue ablation.

Numerous studies on hard tissue ablation have been carried out using CW and long pulse (100s of μs) CO_2 lasers [89-92]. The researchers observed severe tissue charring in the surrounding tissue within a few millimeters of the ablated area, as well as necrosis in the ablated area itself. Mechanical side effects, such as cracking, fracturing, and flaking, were also present, as shown in Fig. 8a [92]. This thermal and mechanical damage delayed the healing process. Forrer et al. made remarkable improvements on the process of CO_2 laser ablation [93]. By using a CO_2 laser with short pulse duration (1.8 μs) and relatively low fluence (15 J/cm^2), they reduced the amount of thermal damage to within 10-15 μm of the ablated area. Rosa et al. also reported similar results (8 μm) using a CO_2 laser with a 5 μs pulse duration [94], and Henn et al. noted reduced carbonization and mechanical effects when using a pulsed CO_2 laser (80 μs pulse duration) [95].

More recently, efforts have been made to reduce collateral thermal damage by cooling the ablation area. Several cooling methods have been used, such as putting a layer of water on the sample or using an air-water spray [96, 97]. For example, Ivanenko et al. reduced the thermal interaction zone to within 2-6 μm of the ablated area using an air-water

spray and a CO_2 laser with a 400 ns pulse duration [96]. Despite these successes, water cooling did not completely prevent peripheral thermal damage [15, 96, 98], which causes chemical changes in the tissue [99]. Water cooling can also reduce ablation efficiency(AE), as the water partially absorbs the laser beam [100].

- Er:YAG laser

Water absorbs Er:YAG laser light (2.94 μm) 15 times more than CO_2 lasers (10.6 μm). When hard tissue is exposed to Er:YAG laser irradiation, the water inside the tissue boils. The sudden vaporization of water causes microexplosions that remove material [101, 102]. Due to these thermal (vaporization) and mechanical (microexplosions) effects, the interactions between Er:YAG lasers and hard tissue are said to be thermomechanical in nature.

Many studies have investigated the feasibility of hard tissue removal using Er:YAG lasers [103- 105], which are shown to cause less thermal damage than CO_2 lasers. However, some studies show that the mechanical stress of Er:YAG laser ablation causes large microcracks up to 300 μm deep in tissue [104]. Niemz et al. and Harashima et al. found that, when used on dental tissue, Er:YAG lasers cause non-uniform ablation, leading to a rough and irregular tissue surface, as shown in Fig. 8b [104, 106]. Er:YAG ablation also causes the ejection of organic and inorganic tissue microparticles. Some studies reported thermal damage on a scale of a few absorption lengths (5 μm), with charring in adjacent tissue [107, 108]. Sasaki et al. observed a change in the bone tissue's calcium (Ca) to phosphorus (P) ratio after Er:YAG laser ablation, delaying the healing process [109]. In summary, Er:YAG laser ablation has many drawbacks.

To overcome the disadvantages of Er:YAG laser ablation, many researchers have tried using water sprays to reduce thermomechanical effects [110, 111]. When Armengol et al. used a water spray during Er:YAG laser ablation, the temperature only rose by 0.96 ℃, compared to 3.55 ℃ without water [110]. Kang and Welch reported an absence of carbonization when applying a 500 μm water layer to bone tissue [111]. While these studies succeeded in eliminating thermal damage, Kuscer and Diaci noted that a portion of the laser irradiation was attenuated by water before reaching the bone, reducing ablation efficiency (AE) [100].

- Ho:YAG laser

Ho:YAG laser irradiation (wavelength 2.12 μm) can vaporize hard tissue, as it is highly absorbed by water. Many studies have used Ho:YAG lasers for hard tissue ablation, with less than favorable results. Ho:YAG lasers penetrate deeper into tissue than Er:YAG lasers, and they require more energy to reach the vaporization threshold [112]. Due to these factors, Ho:YAG lasers cause far more tissue damage than Er:YAG lasers. Romano et al. reported extreme thermal damage extending up to 300 μm around the ablation area when using Ho:YAG laser (pulse duration 250 μs, fluence 120 J/cm^2) [113]. Charlton et al. noted thermal damage within 80 μm of the ablation area, with charred tissue extending 7 μm deep, slightly deeper than the 5 μm caused by Er:YAG laser ablation [107]. When Niemz performed Ho:YAG ablation on a dentin sample, he observed cracks and melted tissue, as shown in Fig. 8c [104]. Despite these thermal interactions, Ho:YAG lasers are far less damaging than CO_2 lasers, which cause charring 300 μm deep [107].

- Nd:YAG laser

The main components of hard tissue, including water and hydroxyapatite, have weak absorbing Nd:YAG laser radiation (wavelength 1.064 μm). However, Nd:YAG lasers can still remove material by breaking the chemical bonds of the tissue, because the laser's wavelength (1.064 μm) corresponds to 1.17 eV of photon energy. Many experiments on Nd:YAG laser ablation have been performed. Niemz demonstrated that an Nd:YAG laser (pulse duration 30 ps) can create precise cavities in dental tissue, as shown in Fig. 8d [114]. However, Nuss et al. reported tissue damage within 10-15 μm of the ablation area when using an Nd:YAG laser (pulse duration 10 ns) [115]. In addition, Gaspirc and Skaleric observed thermal damage and a change in the chemical nature of dental tissue after Nd:YAG laser irradiation [116], causing the dentin to take on a rougher surface [117].

- Excimer lasers

Excimer lasers produce various UV wavelengths, including 193 nm (ArF), 248 nm (KrF), and 308 (XeCI). Studies using excimer lasers noted precise removal of tissue, low thermal effects, an absence of tissue necrosis or mechanical damage, and no delays in the healing process [118, 119]. Despite of potentially undesirable health effects from UV radiation, Excimer lasers cause less damage because they have short pulse durations (10s of ns), which induce gentle photoablation. However, Sarkar et al. observed thermal damage in an area of 60-70 μm using a 351 nm excimer laser, as well as 1-3 μm of thermal damage using 193 and 308 nm lasers [120].

The table below summarizes thermal side effect of hard tissue ablation using long pulse laser (> 10 ps).

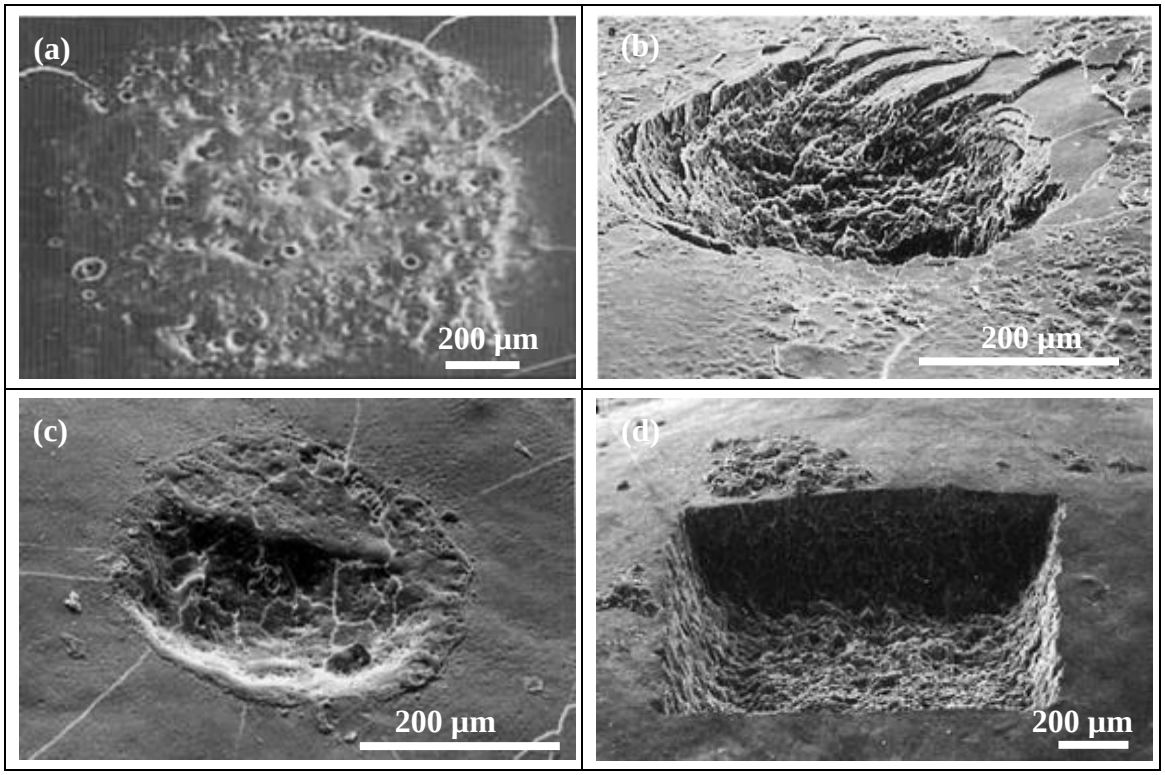

Figure 8: Cavities made by several types of lasers in human dentin. (a) CO_2 laser with a pulse duration of 100 µs and a repetition rate of 10 Hz [92], (b) Er:YAG laser with a pulse duration of 90 µs and a repetition rate of 1 Hz [104], (c) Ho:YAG laser with a pulse duration of 3.8 µs and a repetition rate of 1 Hz [104], and (d) Nd:YLF laser with a pulse duration of 30 ps and a repetition rate of 1 kHz [114]. Reprinted with permission from [92, 104, 114**]**

Table 3: Summary of long pulse laser ablation of hard tissue, shows the thermal damage zone resulted from ablation process.

Laser	Pulse duration (µs)	Tissue	Thermal damage zone (µm)	Authors
CO_2 (9.6 µm)	1.8	Pig bone	10-15	Forrer et al.[93]
	5	Human dentin	8	Rosa et al. [94]
	0.4	Pig bone	2-6	Ivanenko et al. [96]
Er:YAG (2.94 µm)	200	Cortical bone	5	Charlton et al. [107]
	300	Bovine skull	25-40	Fried et al.[108]
Ho:YAG(2.12µm)	250	Cortical bone	300	Romano et al. [113]
	250	Cortical bone	80	Charlton et al. [107]
Nd:YAG (1.06 µm)	0.01	Pig skull	10-15	Nuss et al. [115]
XeF laser (351 nm)	0.02	Pig bone	60-70	Sarkar et al.[120]
ArF lasers (193 nm)	0.01	Pig bone	1-3	Sarkar et al. [120]

2.4.2 Short pulse lasers (< 10 ps)

The short pulse regime (<10 ps) removes material through plasma-mediated ablation. The material's lattice is heated on an ultrashort time scale, causing rapid hydrodynamic expansion of the resulting plasma, which leads to ablation [8]. Because the ablation process occurs faster than thermal diffusion to surrounding tissue, these lasers make precise cuts with minimal residual thermal damage. Studies have used many types of fs and ps lasers, such as Ti:Sapphire and Yb:KYW lasers, to investigate the feasibility of lasers in hard tissue removal. Most efforts have focused on calculating ablation thresholds, measuring ablation rates, calculating rises in temperature during ablation, and observing the effects of external cooling systems [24, 121, 122].

Studies have shown that lasers with shorter pulse durations have lower ablation thresholds. Kim et al. found that when the pulse duration of a Spitfire laser (800 nm, 1 kHz) was reduced from 20 ps to 130 fs, the ablation threshold of human dentin changed from 3.8 to 0.75 J/cm^2 [121]. Stern et al. observed the same relationship between pulse duration and ablation threshold [123]; the threshold for bovine cornea ablation was 20 J/cm^2 with 30 ps dye laser pulses (625 nm, and 20 Hz) and only 4 J/cm^2 with a 1 ps laser. The ablation threshold was further reduced to 1.6 J/cm^2 with 100 fs pulses.

Ultrashort pulse lasers typically have low ablation rates. The ablation rate is the volume of tissue cut per pulse (μm/pulse), and lasers with low ablation rates remove tissue slowly. However, a low ablation rate ensures precise ablation with minimal collateral damage, as shown in Fig. 9a [124]. Neev and Squier measured the ablation rate of a

Ti:Sapphire laser (800 nm, 350 fs, 1 kHz) on enamel tissue as 0.2 µm/pulse at 1 J/cm^2 (the threshold level) [24]. Rode et al. found similar results when using ablation threshold fluence (2 J/cm^2) to remove teeth; the ablation rate was about 0.2 µm/pulse [125].

A laser's ablation rate must be high enough to meet clinical requirements. Some studies have attempted to make ultrashort lasers viable using high radiation fluences, with modest success. When Silva et al. used a 4 J/cm^2 laser (1045 nm, 500 fs) on a dentin sample, the results showed an increase in ablation rate from 0.2 µm/pulse (at 1 J/cm^2) to 1.4 µm/pulse [122]. Neev's group found that the ablation rate of dentin enamel increased from 0.1 µm/pulse at 2 J/cm^2 to 1.2 µm/pulse at 34 J/cm^2 [24]. Still, ultrashort lasers have lower ablation rates than Er:YAG (250 µm/pulse), Ho:YSGG (80 µm/pulse), and Nd:YAG lasers (14 µm/pulse) [117].

High pulse frequency is necessary to achieve practical ablation rates, but few studies have investigated the relationship between repetition rate and ablation rate. When Fahey et al. used a 1.3 ps fiber laser (λ = 1552 nm) with a wide range of pulse frequencies (50 to 500 kHz) to remove hard tissue, they found that as repetition rate increased, so did ablation depth [126]. At constant laser fluence of 7.7 J/cm^2, the ablation depth increased from 16 µm at 50 kHz to 108 µm at 500 kHz, at which point collateral thermal damage to the surrounding tissue was observed. Cangueiro and Vilar also found that the ablation rate of a Yb:KYW laser (1030 nm, 500 fs) increased sixfold when pulse frequency was increased from 50 Hz to 1000 Hz. At 2,000 Hz or greater, the ablation area became irregular, dark, and carbonized, with cracks forming below and around the ablation zone,

as pictured in Fig. 9b [127]. Plotz et al. used an Nd:YVO_4 laser (1064 nm, 8 ps) in a similar study [128]. They found that 500 kHz was the highest pulse frequency that did not cause thermal damage to surrounding tissue, and it produced considerably higher ablation rates than the lowest pulse frequency (50 kHz). Overall, a high repetition rate substantially improves the ablation rate, but it can also cause thermal damage.

Thermal side effects associated with high repetition ultrashort laser ablation are caused by the accumulation of heat, which leads to an increase in temperature. To protect adjacent tissue from irreversible damage during ablation, the increase in temperature must not exceed 10 °C [129]. Many studies have attempted to measure and mitigate the temperature increase caused by ablation. Neev et al.'s study showed that the temperature increases by roughly 2.5 ^{o}C of surrounding tissue when using low a fluence (3 J/cm^2) and low pulse frequency (10 Hz) Ti:Sapphire laser (1050 nm, 350 fs) [130]. When they increased the fluence to 34 J/cm^2, the temperature rose to 8 ^{o}C above room temperature after only 2 seconds. After 50 seconds of continuous ablation, the temperature reached 70 ^{o}C. Le et al., using a Yb:KYW laser (1030 nm, 560 fs, 1 kHz) with a fluence of 14 J/cm^2, measured a temperature rise of approximately 17 ^{o}C during dentin ablation [131]. By contrast, Silva's group only measured a 5.8°C increase in temperature despite using a fiber laser (1045 nm, 500 fs, 4.9 J/cm^2 fluence) with a 100 kHz repetition rate [122]. The same study noted a rapid increase in temperature to 39°C when using a 10 ps fiber laser (1064 nm, 100 kHz) on dentin.

Thermal damage can be reduced with an external cooling system, such as a water spray. Some studies reported that using water can limit the temperature rise [122, 131]. For example, without cooling, the temperature rose by 17.5 ^{o}C during hard tissue ablation with a 14 J/cm^2 laser fluence. Le et al. used forced water cooling to lower the increase in temperature to 6.6 ^{o}C [131]. The same behavior was observed using an air-water spray, which reduced the temperature increase to about 7.1 °C, compared to 26 ^{o}C without water cooling [122]. On the other hand, water spray cooling may reduce the ablation rate of ultrashort pulse lasers. One study [127] reported a minor effect, while another study reported a 70% effect [122].

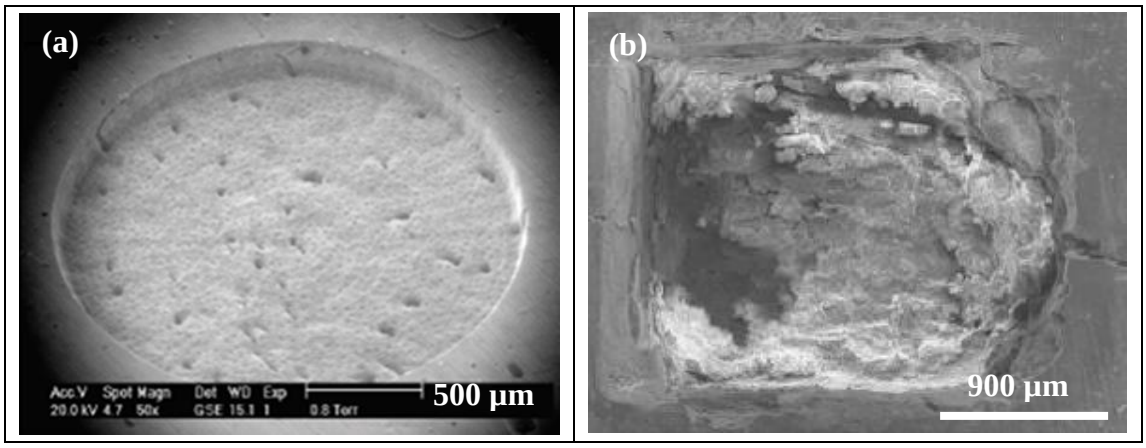

Figure 9: (a) Bovine compacta ablated by Ti:Sapphire laser pulses (800 nm, 700 fs, and 1 kHz) using 0.65 J/cm^2 [124], and (b) Cortical bone ablation produced using Yb:KYW laser (1030 nm, 500 fs, 2 kHz) with 2 J/cm^2[127]. Reprinted with permission from [124, 127]

Chapter 3: Methods

3.1 Summary of ultrashort laser systems

Two laser systems were used in this project. The first was the Ti:Sapphire chirped-pulse amplification system (Spitfire-LCX, Spectra Physics), a laser system with femtosecond pulse duration, 800 nm wavelength, 270 µJ pulse energy, and 1 kHz repetition rate. The second was a commercial high energy mode-locked picosecond fiber laser system (Uranus-µJ Series, PolarOnyx Laser, Inc.) operating in the near-IR region, with a wavelength of 1035 nm, pulse duration of approximately 1 ps, and repetition rate of 100 kHz - 1 MHz. Two different setups were used to perform ablation experiments with the laser systems.

3.1.1 Ti:Sapphire laser

The first ultrashort laser system in this study consists of a Ti:sapphire oscillator (Tsunami), a diode-pumped solid state (DPSS) laser (Millennia V), and a Ti:sapphire chirped-pulse amplifier (CPA) (Spitfire) along with its pump a diode-pumped neodymium yttrium lithium fluoride (Nd:YLF) laser (Evolution), shown in Fig. 10. The Ti:sapphire mode-locked oscillator laser (Tsunami) is pumped by a Millennia V continuous-wave, frequency-doubled neodymium doped yttrium orthovanadate ($Nd:YVO_4$) laser, which has a wavelength of 532 nm. The Tsunami oscillator generates ultrashort laser pulses with a 90 fs pulse duration (fullwidth half-maximum [FWHM]) and ~9 nJ maximum pulse energy at a repetition rate of 83 MHz. The laser's peak wavelength was measured to be roughly 800 nm with a FWHM bandwidth of about 13 nm. The oscillator's output needed to be

amplified, as its pulse energy was too low for ablation experiments. The laser pulses were used as seed pulses in the Ti:Sapphire chirped-pulse amplifier (CPA) (Spitfire).

Ultrashort pulses are high-intensity, even with low energy at small spot size. Any direct amplification of these pulses can damage the optical components of the amplifier (Spitfire) and induce unwanted nonlinear effects in the amplification cavity. Prior to amplification, the seed pulses were "stretched" by dispersive optics in the Spitfire. The stretched pulses were then amplified in a regenerative amplifier, which was pumped by an Nd:YLF laser (Evolution) operating at a wavelength of 531 nm and a repetition rate of 1 kHz. The stretched amplified pulses were then recompressed to ~210 fs in duration. The Spitfire's output pulses were measured at 270 µJ energy, 800 nm wavelength, and 1 kHz repetition rate.

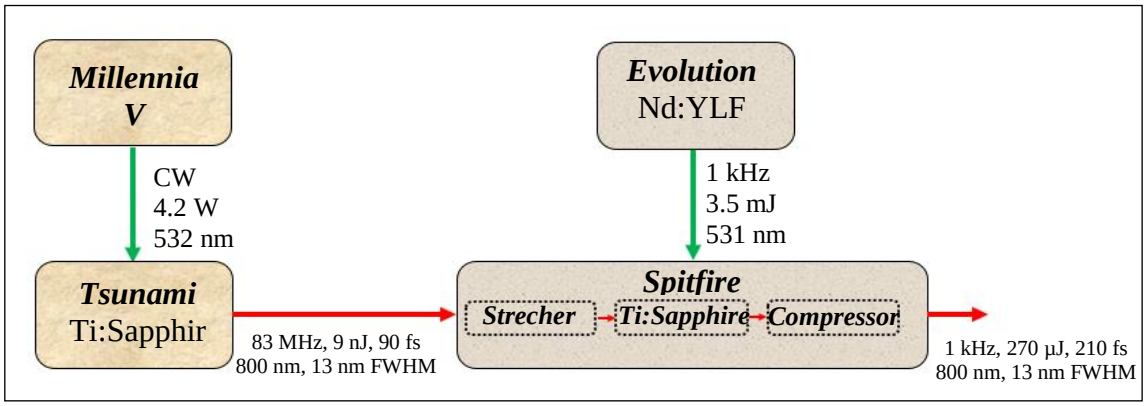

Figure 10: Schematic of the chirped-pulse amplifier system, consisting of an oscillator (Tsunami) and a regenerative amplifier (Spitfire) pumped by Millenia V and Evolution, respectively.

3.1.2 Fiber laser

The second ultrashort laser system in this thesis is a picosecond fiber laser system consisting of a fiber mode-locking oscillator, a fiber stretcher, a preamplifier, a high-power

amplifier, and a compressor, illustrated in Fig. 11. Processing begins with a 980 nm laser pump diode coupled into a 980/1030 wavelength de-multiplexing (WDM) device. The WDM was then coupled into a Ytterbium doped fiber, which was used as a gain medium, with a high doping concentration of 10,000 ppm. The gain medium amplifies the pulses circulating in the cavity. The other side of the Ytterbium doped fiber was coupled to a single mode fiber (SM 25). To select the wavelength and achieve a stable mode-locked train of pulses into the ring cavity, the first single mode fiber (SM 25) was coupled to a bandpass filter with a bandwidth between 1 and 20 nm. A second single mode fiber (SM 25) followed the bandpass filter. To control the polarization of the pulse, a fiber-based in-line polarization controller was installed beside the second single mode fiber. After polarization controlling, the light is directly coupled to enter an in-line polarization beam splitter that only transmits high-intensity pulses. The shaped pulse acts as a saturable absorber to induce mode locking train. The single mode fiber coupled to the polarization beam splitter keeps the pulse in the ring cavity. The other part of the beam is delivered to a polarization maintaining fiber output to be used as the seed laser in the high energy fiber laser system. The part of the beam inside the ring is coupled into a polarization insensitive isolator to ensure unidirectional propagation. The beam polarization was controlled again by a second in-line polarization controller following the isolator. To complete the ring cavity, a third single mode fiber introduced a second in-line polarization controller and was coupled to the WDM [132].

To generate ultrashort high-power laser pulses, the polarized output pulses from the seed laser which have a 10 ps pulse duration, a repetition rate of 38 MHz, and a few mW

of pulse power are lengthened to 100 ps by a fiber stretcher stage. Next, the beam is coupled into a preamplifier consisting of a 980/1030 wavelength de-multiplexing (WDM) device, a 980 nm laser pump diode, and a Ytterbium doped fiber to amplify the pulses to tens of mW. An acoustic optical modulator (AOM) keeps the repletion rate between 100 kHz and 1 MHz. Once the pulses are preamplified, the beam is amplified using a WDM coupled to a Ytterbium doped fiber used as a gain medium. Laser pump diodes are used to amplify the chiped pulses. Finally, the pulses are compressed using gratings, resulting in pulses are ~1 ps in duration with a maximum energy of 40 µJ. The central wavelength is 1035 nm, and the repetition rate falls between 100 kHz and 1 MHz. The beam from the fiber laser is initially ~4 mm in diameter, with vertical polarization.

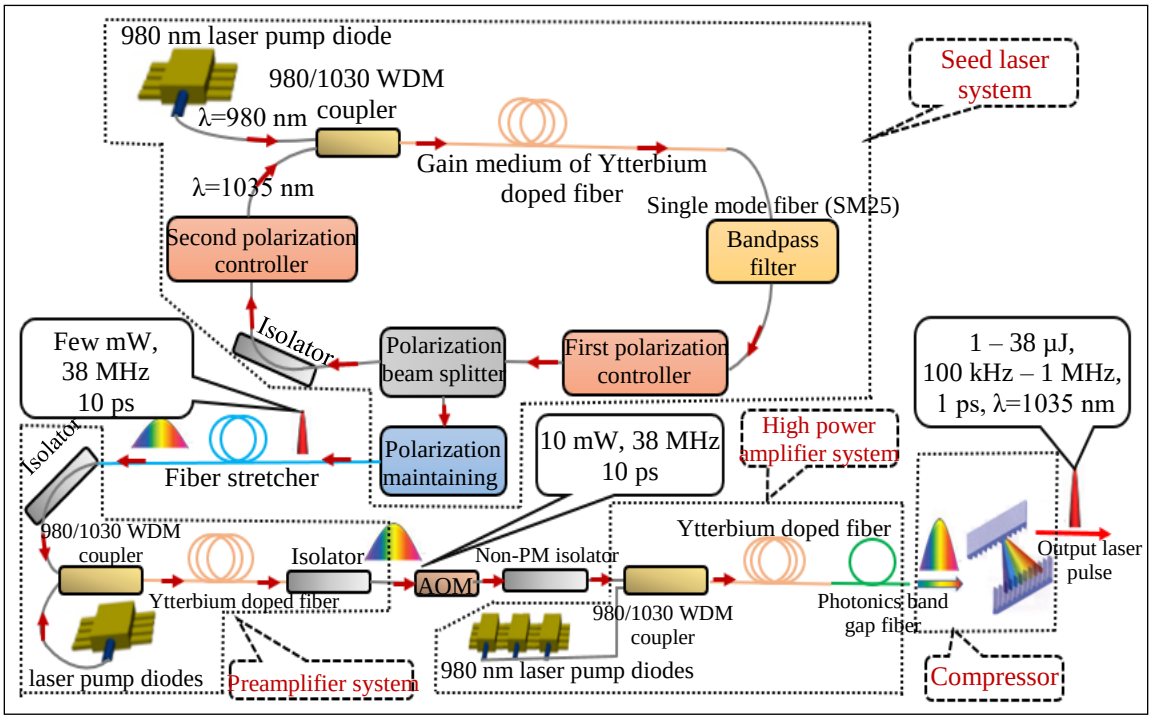

Figure 11: The fiber laser system consists of a mode-locked oscillator (top), a preamplifier (bottom left), and a high-power amplifier (bottom right).

3.2 Laser ablation setup

3.2.1 Ti:Sapphire laser setup

The output beam from the Spitfire is directed to a micromachining setup containing optical and mechanical elements shown in Fig. 12. The beam's initial diameter is ~10 mm, which is focused to ~4 mm by a telescope containing a positive lens (f = 50 cm achromatic doublet lens) and a negative lens (f = -20 cm plano-concave singlet lens). When focused, the beam will not be clipped on the edges of the small-aperture optical components. The pulse energy is manually adjusted by a rotating half-wave plate (0RP44-3, HWP, Newport) and thin film polarizers (11B00UP.26, TFP, Newport). The half-wave plate rotates the polarization of the linearly polarized beam about the optical axis of the birefringent crystal. The output polarization is rotated along the plane perpendicular to the beam's propagation. The amplitude of the electric field component of the beam propagating through the polarizer can be changed by varying the rotational orientation of the half-wave plate's optical axis relative to the incidence electric field. A thin film polarizer further polarizes the beam, eliminating residual s-polarized components perpendicular to the p-polarized ones. The thin film polarizers also minimize dispersive material in the beam's path and prevent nonlinear effects caused by the high intensity of the beam. Precise, automated attenuation of pulse energy is achieved using another thin film polarizer in combination with a half-wave plate mounted in a motorized rotation stage (SR50CC, Newport). A photodiode (DET210, Thorlabs) allows for calibration of beam power at different half-wave plate orientations. A computer-controlled mechanical shutter (VS25S2S1, Uniblitz)

determines the laser's exposure time. In experiments requiring a specific number of pulses, a mechanical chopper was used.

After the attenuation setup, the laser beam is brought to a stainless steel micromachining chamber using three mirrors, as shown in Fig. 12. Stainless steel with ¼ inch thickness eliminates any X-rays that may result from high-intensity ablation [133-135]. A stainless-steel lid with a window made from a transparent quartz coverslip (Electron Microscopy Sciences), 0.15 mm-thick and 1-inch in diameter, covers the chamber. The thin coverslip reduces nonlinear effects coming through the window. The bone sample is fixed on a microscope slide using paraffin wax before being placed in the chamber. To keep the people operating the laser safe, a C-shaped copper shield (3 mm-thick) surrounds the window, and a transparent acrylic-based shield separates the chamber from those standing in front of it. A hand-held radiation detector (Eberline RO-20 ion chamber) was used to confirm the absence of X-ray emissions around the chamber during the ablation process.

The chamber is positioned on two motorized translation stages (UTM100PP.1, Newport) controlled by a motion driver (MM4006, Newport) that precisely moves sample in the X-Y plane. The laser beam is focused into the chamber by a plano-convex lens (LA1986-B, BK7, Thorlabs) mounted on a motorized translation stage (Newport MFN25PP). The spot size (ω_o) of the focused beam was measured at 15.1 μm at ($1/e^2$). The depth of focus (b) of the Gaussian beam (the distance between two points within which $1/e^2$ of the total power exists) was calculated from Eq. (2) to be 1.8 mm [136]. A confocal

monochrome charged-couple device (CCD) camera was used with an LED light source to monitor the ablation process.

$$b = \frac{2\,\pi\,\omega_o^2}{\lambda} \tag{2}$$

Where ω_o is beam radius and λ is laser wavelength.

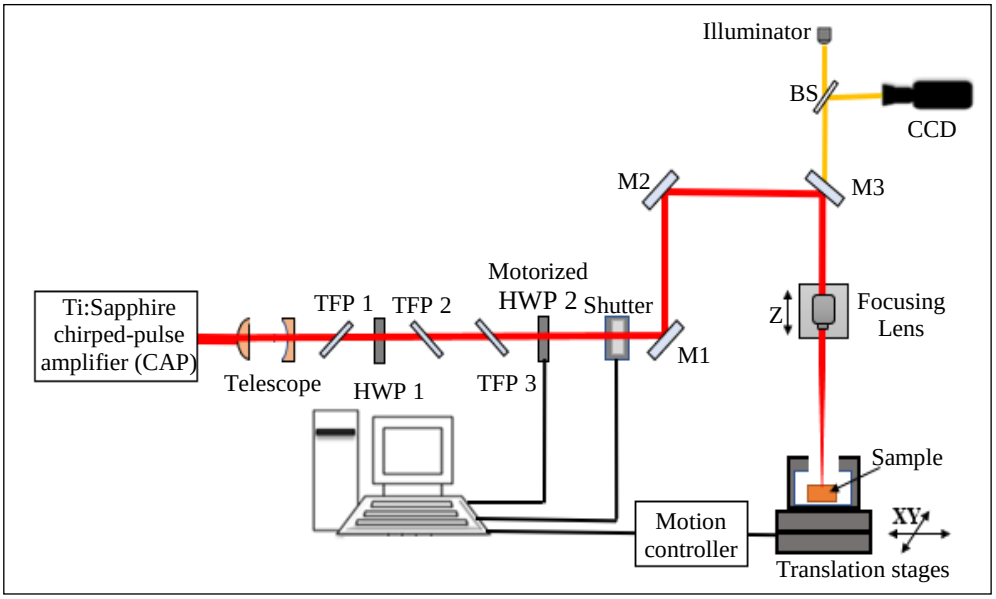

Figure 12: Schematics of the Ti:Sapphire laser system. The pulse energy is adjusted using an attenuation setup containing half wave plates (HWP 1, and HWP 2) and thin-film polarizers (TFP 1, TFP 2, TFP 3). The reflected mirrors (M1, and M2), a dichroic mirror (M3), and a beam splitter (BS) deliver the laser beam to the chamber.

3.2.2 Fiber laser setup

The fiber laser beam is guided to the micromachining setup, where all the fiber laser system experiments are carried out. The schematics of the setup, including optical and mechanical components, are illustrated in Fig. 13. To protect the fiber laser system from beams reflected by optical components within the micromachining setup, an optical isolator (800 nm Broadband Optical Isolator, Electro-Optics Technology) allowing the transmission of the vertical polarization beam in only one direction was used. The optical

isolator contains a Faraday rotator, an input polarizer, and an output polarizer. The input polarizer acts as a filter that only allows linearly polarized laser beams into the rotator. The rotator turns the polarization of input beam 45°, then lets it through the output polarizer. If the beam travels backwards, it is polarized 45° by the output polarizer, then rotated 45° by the rotator, polarizing the beam horizontally. Because the input polarizer is vertically aligned, the beam will be extinguished.

Pulse energy is manually attenuated using a half-wave plate (λ/2, 1053 nm, Thorlabs) mounted on a rotation stage and a Glan-laser polarizer (CPAS-15-670-1064, CVI). A computer-controlled mechanical shutter (SH-10L interlock, EOPC) adjusts the laser exposure time. The beam is then delivered to a stainless-steel chamber using four high-reflection mirrors (M1, M2, M3, and M4), a dichroic mirror (M5), and a beam splitter (BS). A bone sample is fixed on a microscope slide and placed in the chamber.

The stainless-steel chamber is mounted onto two computerized translation stages (UTM100PP.1, Newport) to precisely maneuver the sample in X and Y directions. A motion driver (MM4006, Newport) connected to the computer program controls the stages. The focusing element (a microscope objective or a lens) is mounted on a manual linear translation stage to adjust the focal point of laser beam along the Z direction. Most experiments used a microscope objective (50X, N.A = 0.42, Plan Apo NIR Infinity, Mitutoyo) with a focal length of 200 mm and a working distance of 17 mm. The focal spot diameter (*D*) of the objective for the beam can be calculated using the diffraction limit, as demonstrated in Eq. (3). The diameter of the beam's focal spot was calculated to be 3.0

μm. Using Eq. (2), the depth of focus was calculated to be 13.65 μm. Experiments requiring different focal spot sizes used two plano-convex lenses, one with a spot size diameter ($1/e^2$) of 41.0 μm and a depth of focus of 2.55 mm (f = 125 mm, LA1986-B, Thorlabs), and one with a spot size diameter ($1/e^2$) of 16.4 μm and a depth of focus of 408 μm (f = 50.2 mm, KPX082, Newport). A confocal monochrome charged-couple device (CCD) camera monitored the machining process with an LED light source, shown in Fig. 13.

$$\boldsymbol{D = 1.22\ \frac{\lambda}{N.A}} \tag{3}$$

where λ is the laser wavelength and N.A. is the numerical aperture of the objective.

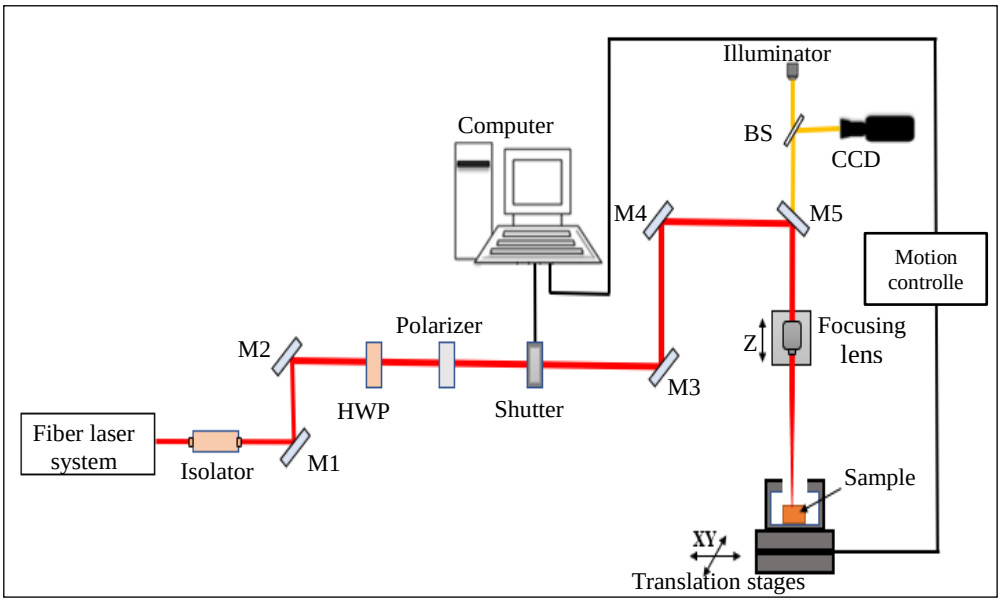

Figure 13: Schematic of the fiber laser system. An isolator prevents reflected beams from entering the laser system. The beam intensity is controlled using a wave plate and polarizer. The laser exposure time is adjusted by a computerized mechanical shutter. The micromachining process is monitored by a CCD camera and LED light source. The beam is guided using high-reflection mirrors (M1, M2, M3, and M4), a dichroic mirror (M5), and a beam splitter (BS).

3.3 Characterization of the laser beam

Several techniques were used to characterize the main properties of the laser beam prior to conducting ablation experiments. The pulse duration, spatial and temporal intensity distribution, spectrum, and average power of the laser pulses were measured using various optical instruments at low laser power to avoid damaging the devices.

3.3.1 Pulse duration

The pulse duration of the Ti:Sapphire laser amplifier system was measured using a second-order non-collinear autocorrelator. Fig. 14 shows the schematic diagram of the Michelson interferometer-based autocorrelator. A beam splitter divides the beam in two (50/50), sending each beam down two separate optical paths. On one path, a mirror mounted on a motorized translational stage (UTM100CC1HL, Newport) delays the beam relative to the other path. Two gold mirrors reflect and propagate the beams through the beam splitter in parallel, focusing them into a nonlinear frequency-doubling BBO crystal (0.5 mm thick potassium dihydrogen phosphate, KDP, crystal), resulting in induced blue light (λ = 400 nm). An InGaAs photodetector records the intensity of the blue light photons, a function of the overlapping of the two pulses. The pulse duration can be measured when one pulse is shifted via the optical delay line.

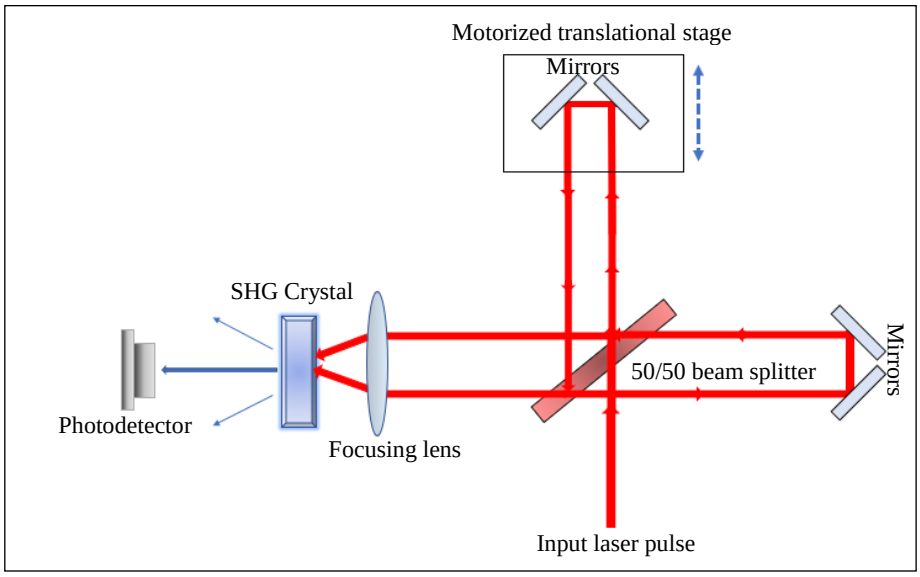

Figure 14: Schematic of a Michelson interferometry autocorrelator setup. The beam is divided down two optical paths. One path uses a mirror on a motorized translational stage to create optical delay. The photodiode records the intensity of the frequency-doubled photons to measure the pulse duration.

3.3.2 Beam profile

A silicon CCD beam profiler (Ophir Optronics, BeamStar) was used to investigate the spatial intensity distribution of the Ti:Sapphire laser (beam profile). The spatial intensity distribution is approximately Gaussian. To ensure alignment, the beam profiler was positioned after the focusing lens in the micromachining station. The optics elements along beam path can be adjusted to prevent clipping while observing the beam's spatial intensity distribution. The CCD profiler was also used to confirm that there is no change in the laser beam distribution.

3.3.3 Peak wavelength

The Spitfire and Tsunami output beam spectrums were measured with a fiber-coupled spectrometer (PC2000 PC, Ocean Optics). Both laser beams had a peak wavelength of around 800 nm and a full width half maximum (FWHM) bandwidth of

approximately 13 nm. A spectrometer (AQ-6315E, Ando) measured the spectrum of the output beam from the fiber laser. The peak wavelength was 1035 nm, with an FWHM bandwidth of 12 nm.

3.3.4 Average power

A silicon-based photodiode sensor (PD300-3W, Ophir Optronics) and a NOVA universal power meter display (1Z01500, Ophir) were used to measure the average power of the laser systems. To calibrate the laser's power, a small portion of the beam was directed into a photodiode (DET210, Thorlabs) positioned before the of the Ti:Sapphire system's micromachining station, and an optical power meter was placed in front of the focusing lens. The power meter was close enough to the lens to avoid the high-intensity focal point of the beam. The chamber's quartz coverslip window was positioned on the beam path to account for Fresnel losses. The power meter was removed after calibrations. During experiments, the above-mentioned photodiode was used to determine the laser's power.

3.4 Bone sample preparation

The McMaster Animal Research Ethics Board (AREB) approved the experimental protocol and use of bone tissue. All bone samples were acquired from the same butcher in Hamilton, Ontario, who provided bovine scapula bones with relatively flat surfaces. The soft tissue and periosteum on the bone surface were removed using tweezers and a knife. A diamond wafering saw (Buehler IsoMet) was used to cut the bones to approximately 1 cm in length, 1 cm in width, and 0.5 - 0.7 cm in height. The top and bottom surfaces of the bone were polished using a series of SiC papers (80 and 320 grit) to ensure they were as

flat as possible. The samples contained two layers of cortical bone (thickness 1-3 mm) sandwiching the trabecular layer (thickness ~5 mm), as illustrated in Fig. 15. All bone samples were stored in the freezer at -10 ^{o}C immediately after preparation. Samples were removed from the freezer and left to thaw at room temperature for 24 hours prior to experimentation. When the experiments were complete, the ablated bone samples were stored at -10 ^{o}C for a few days prior to additional sample characterization.

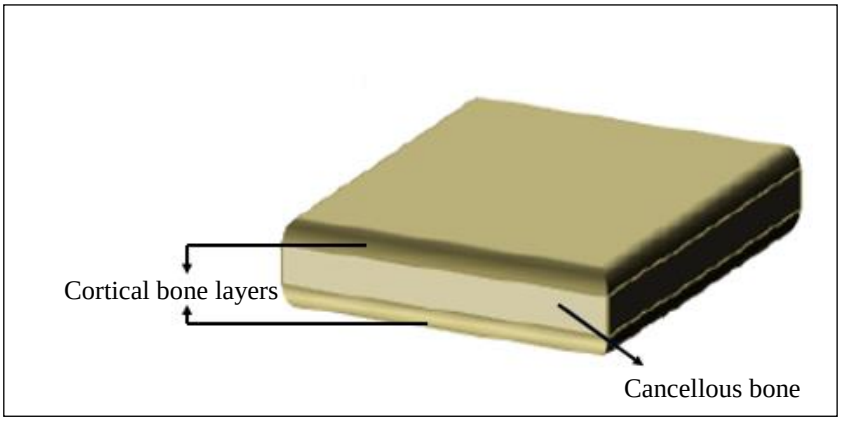

Figure 15: Bone sample including cortical layers sandwiching the trabecular layer. All experiments were performed on the top cortical layer [137]. Reprinted with permission from [137]

3.5 Characterization methods

Several techniques were used to characterize the results of the laser ablation experiments**.** An optical microscope, infinite focus microscope, and scanning electron microscope (SEM) were used to characterize the samples' morphology. Chemical characterizations were carried out using energy dispersive X-ray spectroscopy (EDS) and micro-Raman spectroscopy.

3.5.1 Reflected-light microscopy

To learn how different laser parameters affect the ablation process, channels were ablated onto bone samples using linear scanned ablation. Wide cavities were also created under various experimental conditions to examine their effects on the ablation process. The ablated bone samples were examined in the Canadian Centre for Electron Microscopy (CCEM) at McMaster University using a reflected-light microscope (Axioplan2, Zeiss). This study used bright field reflected-light illumination to operate the optical microscope. Six types of objective lenses were used, including 2.5x, 5x, 10x, 20x, 50x, and 100x. The images were taken by a Clemex CCD camera accompanied by a microscope. Ablation depths and removal rates were measured and analyzed using two types of image analysis software (Northern Eclipse™ and ImageJ).

3.5.2 Infinite focus microscopy

An infinite focus microscope (Alicona) was used to create an optical 3D surface characterization of the sample surface. The microscope produces 3D datasets from which 3D images are generated to characterize surface topography. The microscope uses the focus variation principle; it vertically scans the sample surface, continuously acquiring data. This study used focus variation to measure the height of each focal point. Several profile parameters were measured, such as average roughness (Ra), and mean peak to valley height of roughness profile (Rz). These parameters were studied using a 50x objective with 100 nm vertical resolution.

3.5.3 Scanning electron microscopy

This study used an SEM (515 SEM, Philips) and image acquisition software (Atec) to measure the qualities of surfaces and edges in bone samples. Measurements were taken in the CCEM. A 2D SEM image is taken by scanning the sample's surface with a focused high-energy electron beam perpendicular to the sample surface in a raster scan pattern. Electron-sample interactions create secondary and backscattered electrons, which are measured to create information about surface morphology. The sample was coated with a thin layer (15 nm) of gold to make it more conductive. Low accelerating voltage (~5 keV) was used for imaging to prevent significant charging effects.

3.5.4 Energy dispersive X-ray spectroscopy

EDS is a semi-quantitative technique used to detect and quantify chemical elements in a sample. The bone samples were characterized using an EDS (515 EDS, Philips) and image acquisition software (Atec). Measurements were taken in the CCEM. EDS requires the use of an electron beam to excite the sample, producing X-ray emissions for analysis. Each chemical element has a specific atomic structure that sets it apart from other elements and the sample itself. This analysis used a 10 keV electron beam to acquire an area for study. The system was calibrated ahead of time with a silicon sample.

3.5.5 Raman microscopy

Raman spectroscopy uses inelastic scattering of monochromatic light to identify molecules and study chemical bonding within a sample. Before and after laser treatment, the sample was examined using a Raman spectrometer (inVia Qontor confocal Raman

microscope, Renishaw). Measurements were conducted in McMaster University's Department of Chemistry. A helium-neon gas laser (model 127, Spectra Physics) with an excitation wavelength of 632.8 nm was used to take Raman spectra. Neutral density filters varied the power of laser beam across the sample surface. The beam's spot diameter was focused to less than 1 μm using a 50x objective lens (numerical aperture 0.75). Spectra were recorded within the wavenumber range of 400 to 3200 cm^{-1}, with 5 accumulations and an acquisition time of 30 seconds. The Raman system was calibrated using the silicon reference peak at 521 cm^{-1}. Due to high background levels recorded in all spectra resulting from the samples' rough surfaces, the band wave numbers were determined by fitting the experimental data with polynomial curves using the Fityk software.

Chapter 4: Experimental characterization of Ti:Sapphire laser drilling process parameters

4.1 Determination of ablation thresholds

4.1.1 Introduction

Ablation threshold is the fluence needed to produce a density of free conduction-band electrons that has enough electrostatic force to achieve optical breakdown and eject target material [138]. In other words, ablation threshold is the fluence needed to achieve the smallest possible amount of irreversible collateral tissue damage [139]. Orthopedic medical procedures require an understanding of bone's ablation threshold. The ablation threshold helps characterize laser-tissue interactions, and exploring how different laser parameters affect the ablation threshold can provide insight into laser ablation mechanisms [140]. Therefore, it is important for the ablation threshold to be precisely measured.

To prevent unnecessary tissue damage, the ablation threshold must be as small as possible. Several studies have been carried out to decrease the ablation threshold [123, 141, 142]. These studies found that the ablation threshold differs based on tissue composition and laser parameters, such as wavelength. Murray and Dickinson examined the ablation threshold for several biological tissues, including dentine, enamel, and bone, using an XeCl excimer laser (308 nm) with a pulse length of 200 ns and a repetition rate of 5 Hz [142]. The lowest ablation threshold was 0.1 ± 0.01 J/cm^2 for chicken bone, followed by 0.5 ± 0.01 J/cm^2 for dentin. The highest ablation threshold belonged to enamel, with 2.86 ± 0.01 J/cm^2. Olivié et al. studied the effect of wavelength on the ablation threshold of porcine corneal stroma, using 100 fs laser pulses with wavelengths between 800 nm and 1450 nm

[143]. At 1000 nm, the ablation threshold was 2.2 J/cm^2, which dropped to 1.5 J/cm^2 at 800 nm.

Large amounts of bone need to be removed during orthopedic medical procedures. Consequently, orthopedic laser ablation requires a large number of pulses. The incubation effect, which describes the effect of pulse number on ablation threshold, can help researchers find the lowest possible laser fluence capable of ablating tissue at a sufficient rate.

The experiments in this section aimed to measure the ablation threshold of polished bovine bone at different incident pulse numbers (25, 100, 500, and 1000 pulses) using a Ti:Sapphire ultrashort laser and the D^2-method. The maximum crater diameter (D) of the removed tissue region is measured as a function of laser pulse fluence [144]. The single-pulse ablation threshold and incubation coefficient of bovine bone were also determined.

4.1.2 Method

The experiment was carried out using the Ti:Sapphire ultrafast laser machining setup in Fig. 12 (Section 3.2.1). Ultrashort pulses with a duration of 210 fs, a center wavelength of 800 nm, and a repetition rate of 1 kHz were used to measure the ablation threshold of polished cortical bovine bone. The laser beam was focused onto the sample surface by a plano-convex lens (f = 12.5 cm, BK7, Thorlabs) to a spot size of $\omega_o \approx 15.1$ μm, a beam radius measured at 1/e^2. Craters were ablated on the sample surface using 25, 100, 500, and 1000 incident pulses, with radiation fluences ranging from 2.4 to 18.2 J/cm^2. Three experiments were carried out for each combination of pulse number and fluence. Ablation

threshold was calculated using the D^2-method. The diameter of the crater was measured using a reflected-light microscope (Axioplan 2, Zeiss) and ImageJ software. Threshold fluences (F_{th}) were determined at 25, 100, 500, and 1000 incident pulses using the relationship between the square diameter of the crater (D^2) and the peak fluence (F_o), given by the following equation:

$$\boldsymbol{D^2 = 2\,\omega_o^2\,ln\left(\frac{F_o}{F_{th}}\right)} \tag{4}$$

where ω_o is the laser beam radius at $1/e^2$ of the maximum intensity.

The squared crater diameter can be plotted as a function of peak laser fluence on a semi-logarithmic scale, and the ablation threshold can be determined by extrapolating (D^2) to zero. The beam spot size at $1/e^2$ can also be measured from the plot and verified for consistency with earlier investigation.

Jee et al. showed that the ablation threshold for *N* laser pulses ($F_{th}\,(N)$) is related to the single-pulse ablation threshold ($F_{th}\,(1)$), given by this equation [145]:

$$\boldsymbol{F_{th}\,(N) = F_{th}\,(1)\,N^{S-1}} \tag{5}$$

where S is the incubation coefficient.

The single-pulse ablation threshold and incubation coefficient can be obtained from a log-log plot of the accumulated fluence [$N \cdot F_{th}\,(N)$] as a function of the number of laser pulses (N), where $F_{th}\,(1)$ is equal to the y-intercept, and S is equal to the slope.

4.1.3 Results and discussion

4.1.3.1 Ablation threshold for different pulse numbers

Examples of the ablated craters are shown in Fig. 16. The diameter of each crater was defined as the greatest diameter of the removed tissue area. The asymmetries or irregular shapes of some craters may have resulted from resolidification of melted tissue after ablation [23]. Squared diameters (D^2) of ablated craters were plotted as a function of logarithmic laser fluences for 25, 100, 500 and 1000 incident pulses, as shown in Fig. 17. The results for each of the three experiments were plotted as trails 1, 2, and 3 in the aforementioned graphs. Due to laser pulse energy fluctuations, uncertain beam focus alignment, and the sample surface's topography, there was scatter between trails.

The experimental data of each trail was fitted using a linear least-squares algorithm. The average slope and y-intercept of the three trails were then calculated to determine the equations of the fitted data, as well as the trend line for each incident pulse number, both shown in Fig. 17. The ablation threshold of each pulse number was determined by extrapolating (D^2) to zero, the results of which are in Table 4. The effective spot size diameters for each experiment were calculated from the slopes of the least-square lines to be 30.6 ± 2.6 µm (at 25 pulses per spot), 28.2 ± 2.6 µm (100), 30.4 ± 3.2 µm (500), and 30.4 ± 2.2 µm (1000).

As illustrated in Table 4, ablation threshold decreased as pulse number increased. The lowest ablation threshold was 0.73 ± 0.12 J/cm^2 at 1000 pulses per spot, while the highest threshold was 1.08 ± 0.15 J/cm^2 at only 25 incident pulses. Using the same laser

parameters, Emigh et al. measured the ablation thresholds at 1000 and 25 pulses to be 1.75 ± 0.55 and 2.37 ± 0.78 J/cm^2 respectively [146]. The present study observed smaller ablation thresholds than Emigh et al., likely because the samples in this study were polished to an average surface roughness of 0.25 µm, while Emigh et al.'s samples were unpolished. A sample's roughness can affect the local field intensity and thus threshold fluence [147]. This discrepancy may have also been caused by differences between the composition of porcine bone, used in Emigh et al.'s work, and bovine bone, used in this study. Nicolodelli et al. measured the ablation threshold at 1000 pulses to be 0.23 J/cm^2, even lower than the value measured in the present study (1.75 ± 0.55 J/cm^2) [148]. This is probably because Nicolodelli et al.'s study used a pulse width of 70 fs, whereas this study used a pulse width of 210 fs. Shorter pulse durations result in lower ablation thresholds, because as pulses become more shorter, the laser beam becomes more intense, generating more electrons through multiphoton processes [149].

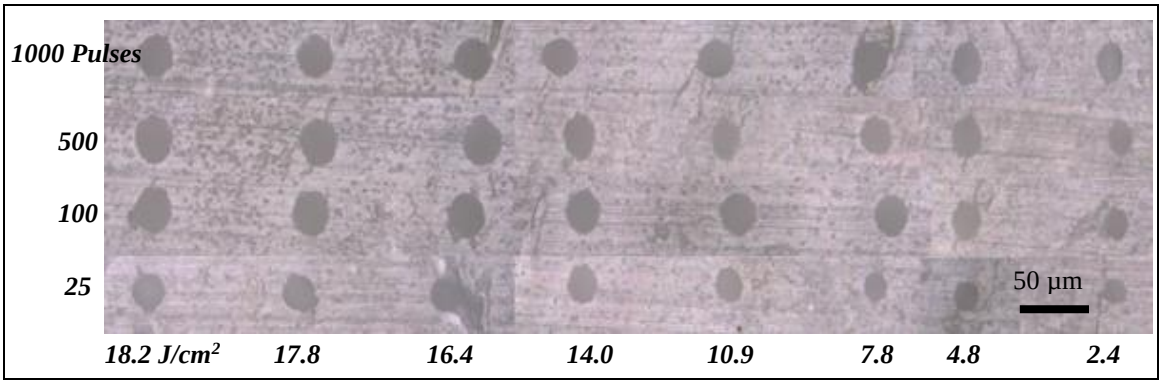

Figure 16: Craters ablated on bone surface by 25, 100, 500 and 1000 incident pulses at different fluences using a Ti:Sapphire ultrafast laser (λ = 800 nm, τ = 210 fs, repetition rate 1 kHz). Images were obtained using a reflected light microscope (50x objective).

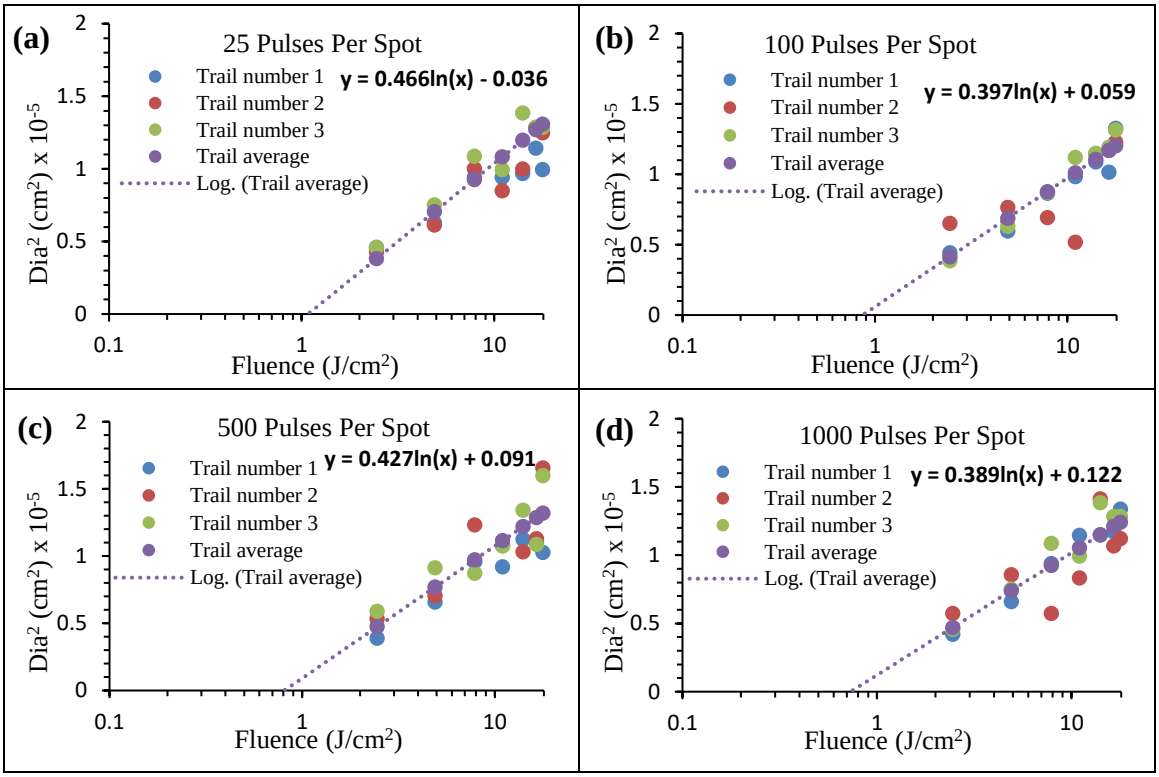

Figure 17: The squared diameters (D^2) of the ablated areas versus the laser fluence (λ = 800 nm, τ = 210 fs, repetition rate 1 kHz) in bovine bone samples. (a) 25 incident pulses per spot, (b) 100 pulses, (c) 500 pulses, and (d) 1000 pulses. Experiment was repeated three times; trail 1, 2, and 3, for each pulse number. The slope and intercept of the plotted trend line were obtained from the average slope and intercept of the least-squared lines of the three individual trails.

Table 4: Ablation threshold for different incident pulse numbers calculated using the D^2-method.[a]

Number of Pulses *(N)*	Ablation threshold (J/cm²)
25	1.08 ± 0.15
100	0.86 ± 0.14
500	0.80 ± 0.17
1000	0.73 ± 0.12

[a] The standard errors of the fits from each individual trial were used to calculate uncertainties.

4.1.3.2 Incubation effect

The accumulated fluence, $N * F_{th}(N)$, was plotted as a function of pulse number (N) on a double-logarithmic scale, illustrated in Fig. 18. The incubation coefficient, *S*, was calculated from the slope of the fitted data with a power function of 0.90 ± 0.02. The single-

shot ablation threshold value was 1.43 ± 0.09 J/cm^2. When S = 1, a change in pulse number does not affect ablation threshold.

Incubation effects come from absorption of fluence. A large-enough number of pulses causes the accumulation of heat in tissue, resulting in thermal modification. This could lead to changes in the tissue's dielectric constants and local electric field, altering the ablation threshold [147]. The present study measured similar incubation coefficients to those in Emigh et al.'s work, indicating similar thermal modifications [146]. However, the ablation threshold of single pulse is smaller than in Emigh et al. (3.29 ± 0.14 J/cm^2), even when using a similar wavelength and pulse duration [146]. As stated earlier, Emigh et al. used unpolished porcine bone, while the present study used polished bovine bone, which could explain the difference in ablation threshold. These findings suggest bovine bone can be removed with less fluence than porcine bone.

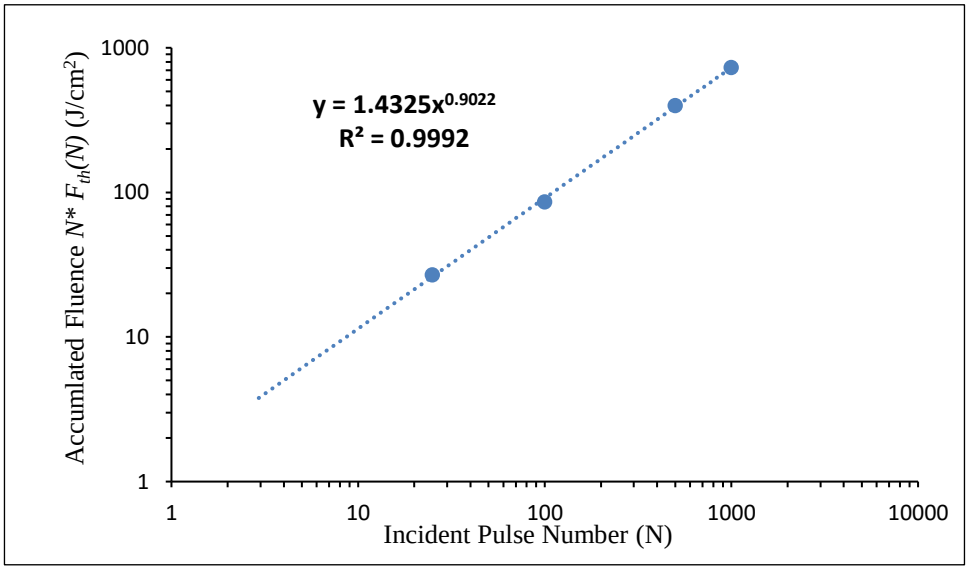

Figure 18: Accumulated fluence versus incident pulse number with λ = 800 nm, τ = 210 fs, and a repetition rate of 1 kHz for a bovine bone sample. The slope yields the incubation factor S = 0.90 ± 0.02, and the single-pulse ablation threshold was 1.43 ± 0.09 J/cm^2.

4.2 Characterization of cutting parameters

4.2.1 Introduction

Hard tissue ablation requires precise cutting, high ablation efficiency (short procedure time), and minimal damage to surrounding tissues. Ultrashort pulse met some but not all of these requirements. They have low ablation efficiency, as they can only remove 1 μm in depth of tissue per pulse [24]. However, they can make precise cuts, as demonstrated by a study using a Ti:Sapphire ultrafast laser [150]. Other studies have shown that femtosecond lasers cause less mechanical damage than other lasers [144, 151], although a few studies observed thermal damage that delayed the healing process [127, 131].

More information is needed before ultrashort laser ablation can become a clinical reality. Specifically, little knowledge exists regarding how bone-laser interactions affect the ablation process. A variety of laser and drilling process parameters influence the ablation process, and different parameters have different effects on the efficiency, precision, and types of damage caused by ablation [35, 152]. Understanding these effects will help improve the removal process by reducing procedure times and mitigating collateral damage which is the main goal of next chapter. The following experiments were conducted to learn more about several parameters, including laser fluence, scanning speed (also called translational speed), number of scanning passes, and pulse duration.

4.2.2 Ablation depth vs. fluence

4.2.2.1 Method

In this experiment, a plano-convex lens (f = 125 mm) with a spot size diameter of 30.2 μm at $1/e^2$ focused the beam onto the surfaces of polished cortical bovine bone samples. To measure ablation depth and rate as a function of laser fluence, multiple channels were created on the sample surface at different fluences, ranging from 3 to 22 J/cm^2, and at two scanning speeds (200 and 500 μm/s). To determine amount of tissue removed per pulse, the effective number of incident pulses on each spot (N_{eff}) was calculated from Eq. 6 to be 94 pulses at 200 μm/s and 38 pulses at 500 μm/s:

$$N_{eff} = \sqrt{\frac{\pi}{2}}\frac{\omega_o f}{v} \tag{6}$$

where ω_o is the spot of laser beam, f is the repetition rate, and v is the scanning speed.

Unless stated otherwise, every experiment in Section 4.2 has several things in common. In each experiment, a Ti:Sapphire ultrafast laser (pulse duration 210 fs, center wavelength 800 nm, repetition rate 1 kHz) ablated several channels onto the sample surface. The ablated channels were 3000 μm long, with 200 μm between each channel. Three trials were carried out for each set of values under investigation. For example, in this experiment, three trials were conducted for every combination of fluence and scanning speed. After the channels were ablated, the sample was cross-sectioned using a diamond-blade sectioning saw, and the channel depths were measured via light microscopy.

4.2.2.2 Results and discussion

Fig. 19 shows a cross-section of the grooves created using a scanning speed of 200 μm/s at multiple laser fluences. Ablation depths were measured from the sample surface to the deepest point of visible distortion. Some bone material can be seen in the grooves, likely caused by debris from ablation or cross-sectioning.

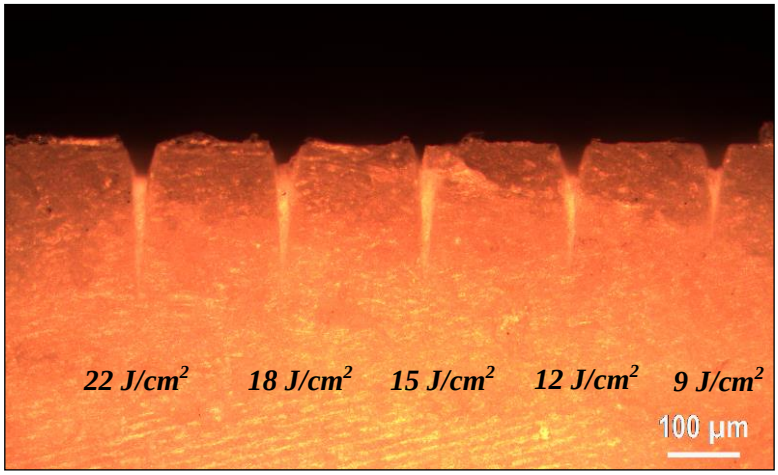

Figure 19: Cross-section of grooves ablated at 22 to 9 J/cm^2, with a constant scanning speed of 200 μm/s.

The ablation depth was plotted as a function of laser fluence in Fig. 20a, at two scanning speeds. As fluence increased, so did channel depth, as lasers with higher fluence deposit more energy into the sample, ablating more material. The results also showed that when the scanning speed was set to 500 μm/s, the laser produced shallower grooves than at 200μm/s. This is because a lower scanning speed gives the laser time to hit the sample with more pulses, as calculated using Eq. 6.

The amount of tissue removed per pulse (removal rate) was calculated by dividing the groove depth by the effective number of incident pulses. It was then plotted as a function of laser fluence, as shown Fig. 20b, which illustrates that as fluence increases, so does

removal rate. At 500 µm/s and 22 J/cm^2, the removal rate (3.8 µm/pulse) was 2.4 times higher than at 3 J/cm^2 (1.6 µm/pulse). The removal rate also increased with scanning speed, likely because higher scanning speeds produce less total depth and debris and allow for more removal rate per pulse.

As stated earlier, high fluence results in shorter procedure times. However, if the laser's fluence is greater than 20 times the ablation threshold, collateral damage to surrounding tissue can be severe. The next chapter investigates the effects of high fluence on surrounding tissue in greater detail.

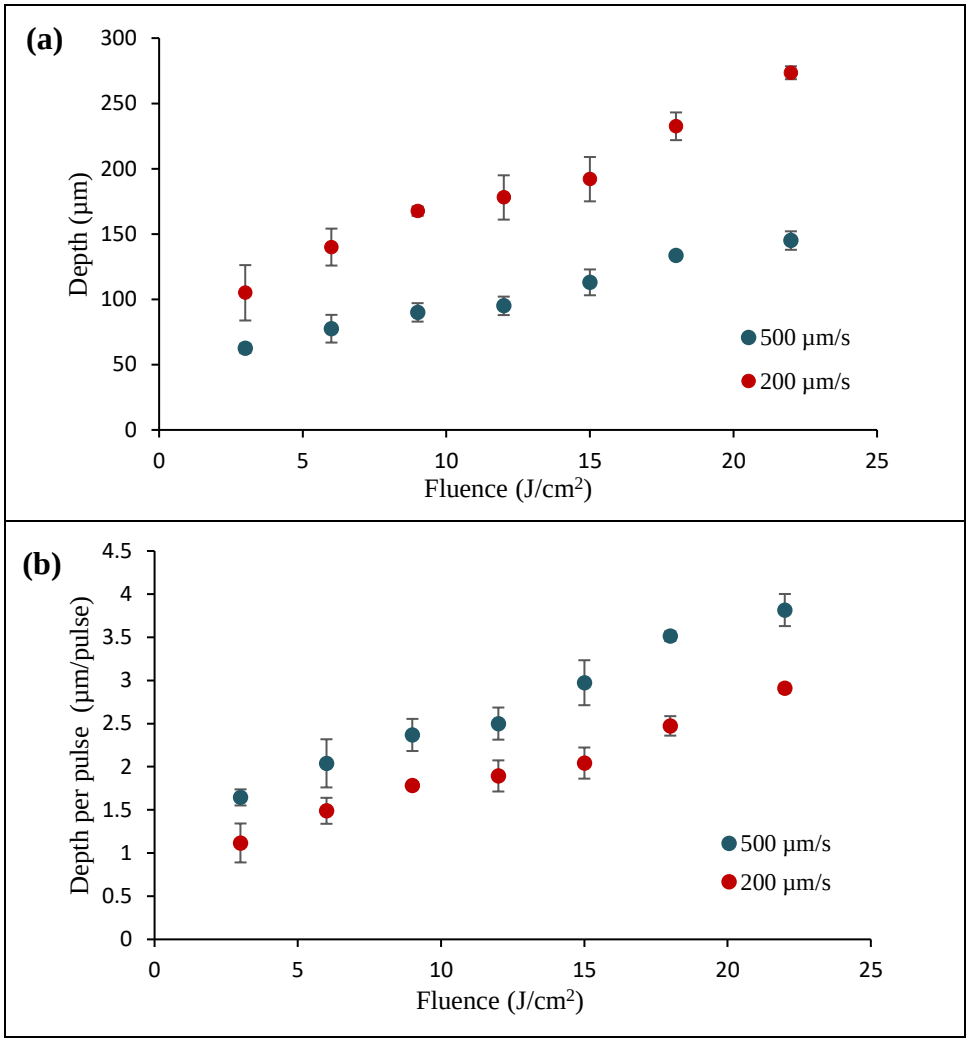

Figure 20: (a) Ablated groove depth and (b) removal rate (µm/s) at various laser fluences between 3 and 22 J/cm^2 and at two scanning speeds: 200 and 500 µm/s. A Ti:Sapphire ultrafast laser (λ = 800 nm, τ = 210 fs, repetition rate 1 kHz) was used. Error bars indicate standard deviation.

4.2.3 Ablation depth vs. scanning speed

4.2.3.1 Method

The following experiments measured ablation depth and rate (µm/pulse) as a function of scanning speed. Multiple lines were ablated on polished bone samples at various scanning speeds (100-1000 µm/s) and fluences (5 and 15 J/cm^2). Scanning speed

determines the number of incident pulses per spot; these numbers were calculated from Eq. 6 and are displayed in Table 5.

Table 5: The number of incident pulses per spot at different scanning speeds, with a spot size diameter of 30.2 µm and a repetition rate of 1 kHz.

Scanning speed *(µm/s)*	Effective pulse number
100	189
200	94
300	63
400	47
500	38
600	31
700	27
800	23
900	21
1000	19

4.2.3.2 Results and discussion

Fig. 21 shows a cross-section of five grooves ablated at 15 J/cm^2, with scanning speeds ranging from 100 to 500 µm/s.

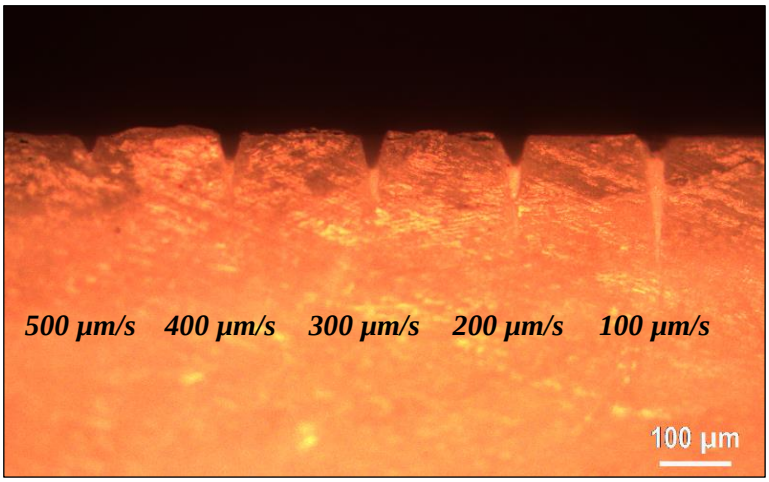

Figure 21: Cross-section of five ablated grooves made using a fluence of 15 J/cm^2 and various translational speeds.

In Fig. 22a, groove depth was plotted as a function of scanning speed at two fluences. At both fluences, channel depth increased as scanning speed decreased. As stated

earlier, lower scanning speeds give the laser more time to hit the same spot with a greater number of incident pulses. Higher fluences also resulted in deeper ablation, the reasons for which are explained in Section 4.2.2.2. However, as scanning speed increases, the difference between the two fluences becomes smaller. These results indicate that low scanning speeds and high fluence both increase ablation efficiency.

Fig. 22b is a graph showing the removal rate as a function of scanning speed at two different laser fluences. The removal rate increased with scanning speed until it reached 500-700 μm/s, whereupon it decreased. This suggests that while lower scanning speeds correlate with increased depth, higher speeds lead to higher ablation rate per pulse [141]. When bone debris accumulates in the bottom of a deep crater, it shields the material underneath from additional laser pulses, a process known as debris shielding. As groove depth increases, the laser beam diverges, reducing its effective intensity [153]. Deeper grooves also have steeper inclines, which effectively reduce laser fluence [154].

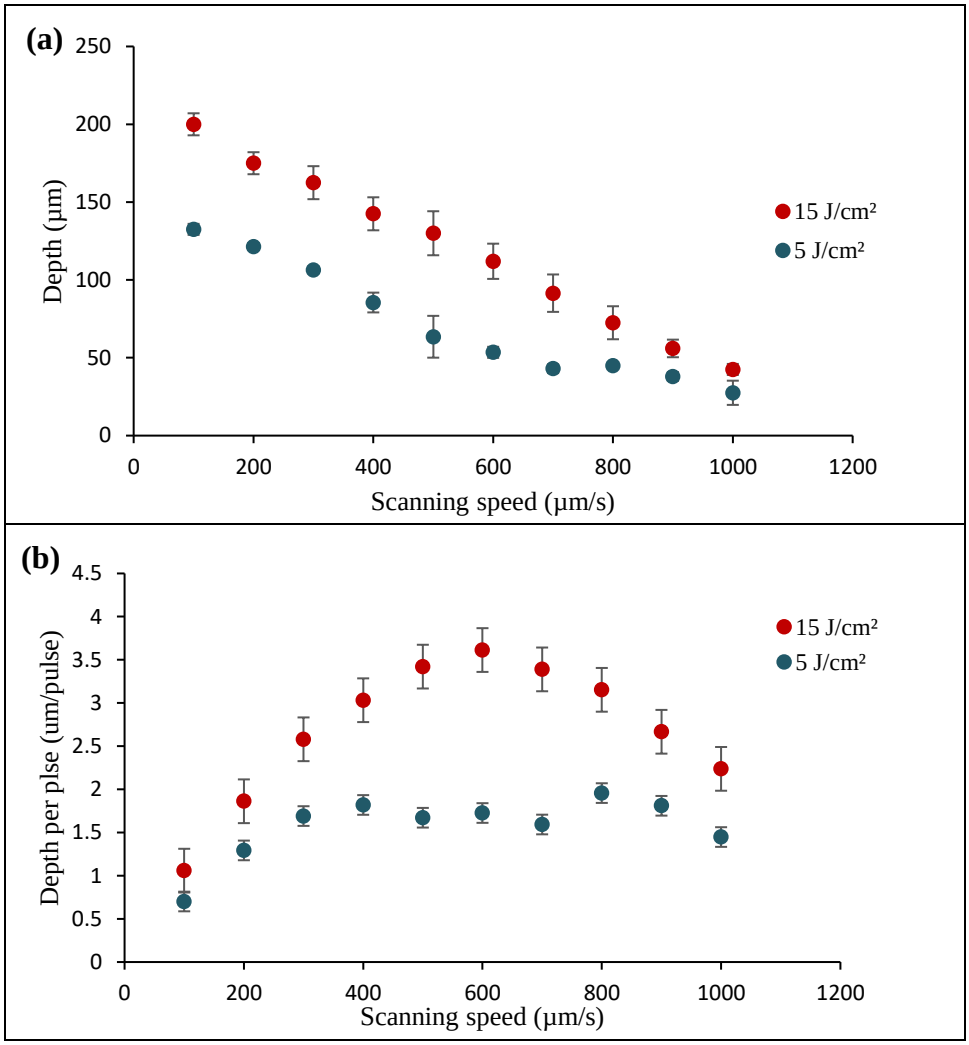

Figure 22: (a) Total groove depth and (b) removal rate as a function of scanning speed between 100 and 1000 µm/s at two different fluences using a Ti:Sapphire ultrafast laser (λ = 800 nm, τ = 210 fs, repetition rate 1 kHz).

4.2.4 Ablation depth vs. number of successive passes

4.2.4.1 Method

During hard tissue ablation, the laser needs to make several passes over the bone to remove enough material. This section focuses on the relationship between ablation depth and the number of passes. Several channels were ablated onto the sample surface at two

fluences (15 and 5 J/cm^2), four different pass numbers (2, 4, 6, and 8), and a scanning speed of 200 μm/s.

4.2.4.2 Results and discussion

The figure below shows a cross-section of a sample that was ablated at 15 J/cm^2. As the number of passes increased, the grooves became deeper, and more debris accumulated at the bottom of the grooves. Fig. 23b graphs the relationship between groove depth and the number of passes. The difference in ablation depth between 2 passes and 8 passes is relatively small, which is explained by the debris shielding effect described in Section 4.2.3.2. As the laser pulse travels down into the groove, the beam is scattered or absorbed. The groove acts as a waveguide for the next pass, further reducing ablation depth. To ensure deep cavities, debris should be kept to a minimum through water or air flow, which are explored in Chapter 5.

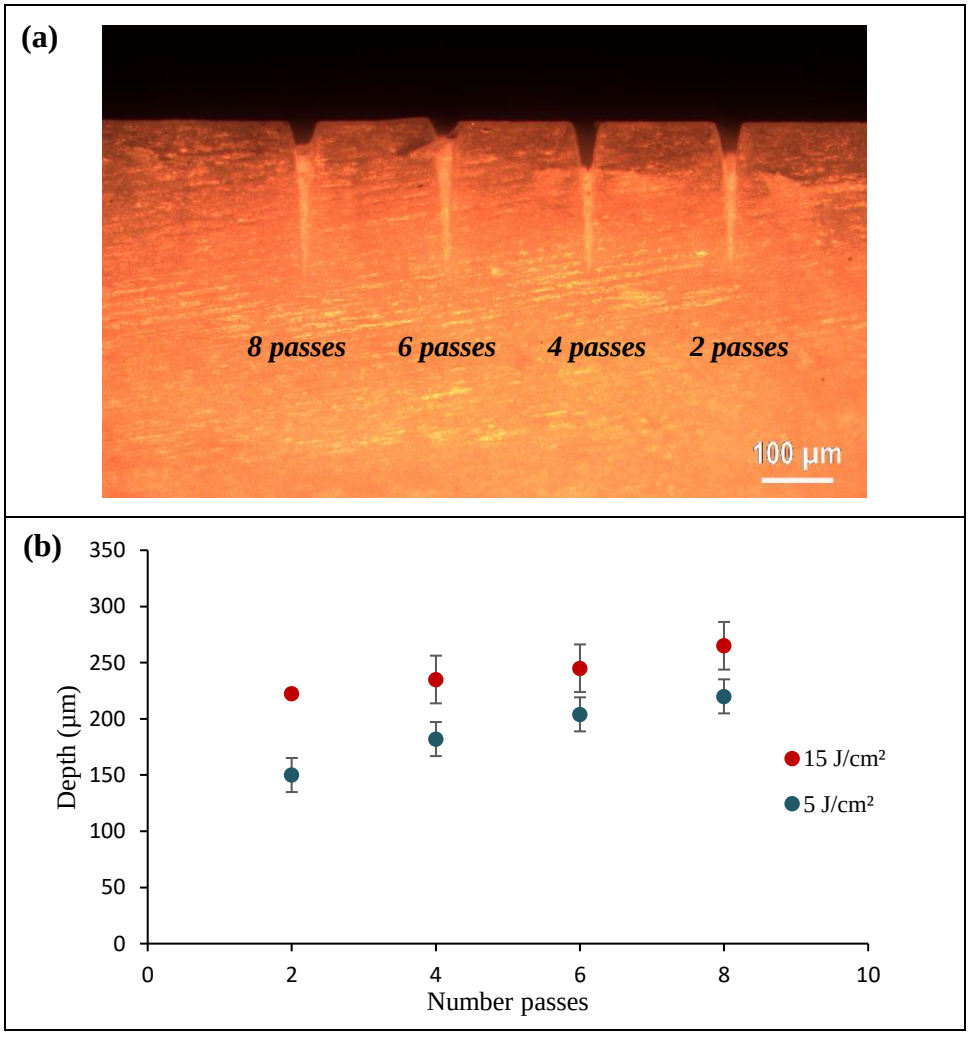

Figure 23: (a) Cross-section of ablated grooves made with different numbers of consecutive passes (15 J/cm^2 fluence, 200 µm/s scanning speed), and (b) Groove depth as a function of the number of consecutive passes (5 and 15 J/cm^2 fluence, 200 µm/s scanning speed) using a Ti:Sapphire ultrafast laser (λ = 800 nm, τ = 210 fs, repetition rate 1 kHz).

4.2.5 Ablation depth vs. pulse duration

4.2.5.1 Method

Pulse duration is one of the most important laser parameters, as it determines the mechanism of ablation. In the next experiment, several craters were created on the sample surface at three different pulse durations (200 fs, 500 fs, and 2 ps), four different laser fluences (12, 14, 16, and 18 J/cm^2), and a scanning speed of 200 µm/s.

4.2.5.2 Results and discussion

The ablation depths at different pulse durations were graphed in Fig. 24a. At all fluences, ablation depth decreased as pulse duration increased, likely because smaller pulse durations have higher peak laser intensities. These high peak intensities result in stronger multiphoton absorption, which induces optical breakdown at lower pulse energies. Also, pulse duration (τ) affects the threshold fluence for plasma-mediated ablation (F_{th}). Their relationship is described by the equation $F_{th} \sim \tau^{x}$. When τ < 100 fs, *x* is less than 0.1, and when 4 ps < τ < 8 μs, *x* falls between 0.4 and 0.6 for various tissue types [35]. Siegel et al. found that as pulse duration increased from 100 fs to 1.5 ps, plasma reflectivity occurred, shielding the sample surface [80]. This finding could also explain the inverse relationship between pulse duration and ablation depth.

Fig. 24b shows the removal rate as a function of laser fluence at different pulse durations. At all fluences, shorter pulse durations resulted in higher ablation rates. For example, as the pulse duration increased from 200 fs to 2 ps (fluence of 18 J/cm^2), the ablation rate decreased from 2.8 to 1.6 μm/pulse. This suggests that shorter pulse durations and higher fluence result in greater ablation efficiency.

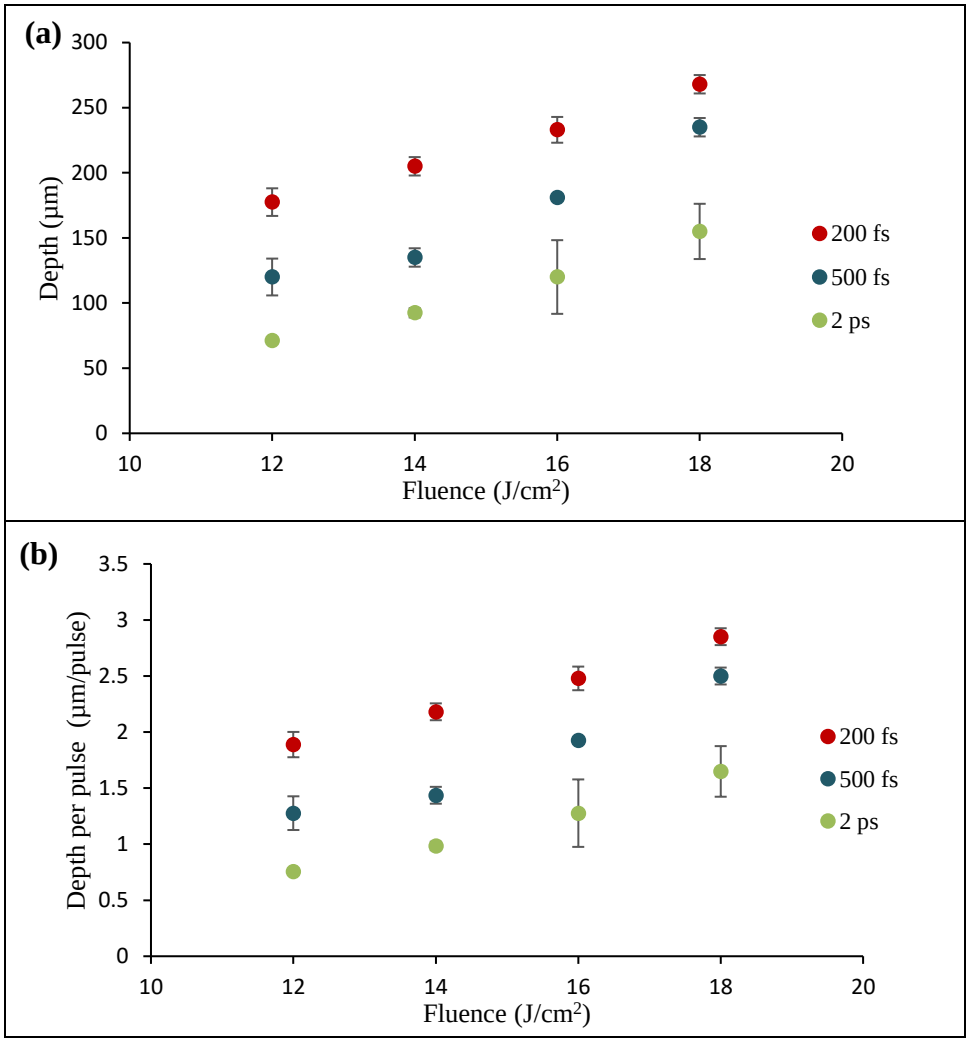

Figure 24: (a) Ablation depth and (b) depth per pulse at different pulse durations, with fluence ranging from 12 to 18 J/cm^2 and 200 µm/s scanning speed, using a Ti:Sapphire ultrafast laser (λ = 800 nm and repetition rate 1 kHz).

Chapter 5: Cavity preparation in bone by ultrashort Ti:Sapphire laser under dry and water experimental conditions

5.1 Introduction

Orthopedic applications require the removal of large volumes of tissue. However, ultrafast lasers can remove only small amounts of hard tissue, on the order of one micrometer of tissue thickness per pulse [8]. The limitation of material removal per pulse using ultrafast lasers has inhibited the practical surgical applications of these lasers [125, 130, 155]. Moreover, in many hard tissue applications, the formation of deep incisions (few millimeters) into the tissue is required. To meet clinical requirements, the amount of material removal per pulse must be maximized with the ability of achieving deep cavities. In chapter 4, it have reported that the quantity of tissue removal generally increases with increasing laser fluence (J/cm^2). Thus, the increase of ablation rate (the volume of hard tissue removed by the laser per unit time, mm^3/s) can be achieved by applying high laser fluence. An et al. have managed to produce larger-diameter holes on the cortical bone with the high fluence of laser set to 19.3 J/cm^2 (~ 6 times higher than the threshold (F_{th})) [150]. The hole depths were shallower than expected due to debris deposited on the bottom of the holes. So far, most ultrafast laser ablation studies have been performed under the condition of still air only [150, 156]. To minimize thermal effect and assist the ablation process, some assistive methods such as water or compressed air flow may be used. More investigations of ultrafast laser ablation of bone using high fluence under different experimental environments are still needed.

In this study, rectangular cavities with the lateral dimension of 1000×220 (μm^2) were produced using a femtosecond laser (210 fs, 800 nm, and 1 kHz). The influence of experimental conditions including air, compressed air flow, still water and water flow on bovine bone tissue ablation at different number of scanning passes and high fluence (~10 F_{th}) was examined. Ablation depth and rate induced at various environments and different scanning passes were measured. Ablation performance including ablation surface morphologies, cut geometry, microstructure, and mechanical and thermal damage induced under different ablation conditions was examined using optical, electron, and Raman microscopies.

5.2 Method

The ablation experiments used the setup illustrated in Fig. 12 (Section 3.2.1). Different ablation environmental conditions were evaluated including: compressed air flow, underwater (non-flowing), and water jet flushing. The results were compared to ablation in ambient atmospheric air, i.e. non-flowing. In the case of the air blowing condition, compressed air was applied on the ablation region during the ablation process. The air flow was delivered using an air pump (Stansport, Electric Air Pump) at 10 psi using a silicon tube and a needle with an inner diameter of 1 mm. The tip of the needle was directed under a 45° angle from vertical and 3 mm from the tissue surface, as shown in Fig. 25a. For ablation with water, two different conditions were tested: 1) the sample is immersed in non-moving water with a 500 µm water layer on top of the sample surface; 2) a thin layer (500 µm thick) of water flowing on top of the sample surface during ablation process. The water flow of 1200 ml/min within the vial was produced by a micro water

pump (DC micro pump, Mini26, BringSmart). The direction of the water flow was perpendicular to the longitudinal axis of the rectangular cavity.

In all experiments, the focused beam was scanned in a raster pattern, as shown in Fig. 25b, on the tissue surface (1000×220 μm^2) to produce rectangular shaped cavities. Each full rectangular raster pass consists by 20 scanning lines (length:1000 µm, line spacing:10 µm). The raster scanning speed was set at 200 µm/s with pulse energy at 55 µJ, and corresponding laser fluence at 15.3 J/cm^2 (~10 F_{th}). The number of scanning passes of 1 to 8 was applied to examine the effect of number of passes on ablation depth (µm) and rate (mm^3/s) under various environmental conditions. We also examined the effect of lowering focus shift during each pass. After ablation, the bone samples were cut by a diamond dicing saw parallel to the shorter axis of the rectangle cavity to expose the cross-sectional profile of the ablated region. The geometries of the cavity cross-section, including depth and area, were measured two times for each crater using a reflected light microscope and analyzed using ImageJ. From the cross-section area, the volume of the ablated cavity was calculated to determine the ablation rate (mm^3/s). In addition, to examine potential thermal damages, Raman analysis was carried out for the sample surface before and after the laser treatment to check for chemical composition changes. Raman spectra were obtained using a Raman spectrometer (inVia Qontor confocal Raman microscope, Renishaw) equipped with a He-Ne laser (model 127, Spectra Physics) operating at 633 nm. The laser beam was focused with a 50× objective lens onto the samples' surface. For each sample, four spectra were recorded with an acquisition time of 30 seconds/record. Due to high background levels recorded in all spectra resulting from the samples' rough surfaces,

the band wave numbers were determined by fitting the experimental data with polynomial curves using the Fityk software.

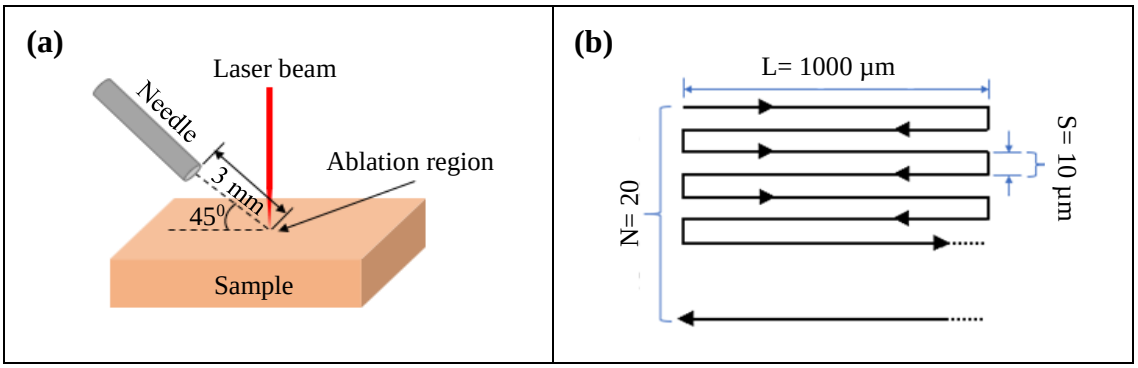

Figure 25: (a) Schematic setup of air flow condition, and (b) Schematic of laser ablation path, L: scanning line length; N: number of scanning lines in one scanning pass; and S: scanning line spacing.

5.3 Results and Discussion

In the above experiments, we systematically examined the effect of ablation environmental conditions on the depth of the ablated crater, ablation rate, crater surface morphology, and potential thermal side effects on the crater surface.

5.3.1 Ablation depth

The crater depth (the distance from the surface to the deepest point in the bottom of the crater) as a function of the number of scanning passes at various environmental conditions is shown in Fig. 26. For all four conditions, increasing of the number of scanning passes produced deeper cavities. In the entire range of scanning passes under examination, the maximum ablation depth was achieved with compressed air flow; while the shallow cavity was observed under the condition with non-flowing air. In the cases where still or flowing water were used, the cavity depths were shallowest. With refocusing objective lens (100 µm) after each scan, the increase in ablation depth was observed only under the

flowing air conditions as shown in Fig. 26. There was negligible effect of refocusing on the depth when non-flowing air or water conditions used (not shown in Fig. 26).

Under the condition of non-flowing air, the ablation depth increased rapidly over the first three scanning passes up to about 580 μm (Fig. 26). After the first three passes, the amount of ablation with each pass decreased. This result is likely due to the influence of ablation debris: i.e. the amount of ablation debris accumulates in the crater [61, 157]. Under the compressed air flow condition, the ablation depth of the cavities was much greater with each scanning pass compared to the non-flowing air condition. The compressed air flow condition also had a decreased rate of ablation after 3 passes, at about 820 μm, when the focus depth was not changed between successive scans. In this case, the change in the amount of ablation can be explained in relation to the Rayleigh length (where the maximum energy density is achieved) which was calculated to be 818 μm for the focusing lens used. With a deeper cut depth, some debris at the bottom of the ablated crater cannot be moved by air flow and could affect the ablation process and depth for both cases (non-refocusing and refocusing).

In the cases of ablation under non-flowing air, it was found that bone ablation was always accompanied by the debris deposited inside the irradiated region. During ablation, debris in the path of laser light can absorb and scatter the incident beam [157, 158]. Consequently, the debris shielding attenuates the pulse energy, leading to decrease in ablation depths of the craters compared to those of air flow. In contrast, the presence of

flowing air during the ablation process removes the debris, leading to clean processes and deeper ablation depth than ablation under only air [131].

During femtosecond laser ablation, multiphoton ionization initiates optical breakdown and plasma formation [159]. The plasma mediated ablation process is accompanied by bubble formation and subsequent material removal at the focal spot [160]. In the presence of water, the incoming laser beam interaction with water may cause non-linear phenomena like filamentation, supercontinuum generation, and optical breakdown of water, which forms a plasma shielding effect reducing the amount of energy reaching the tissue [81, 161]. In addition, another source of energy shielding is generated in the water during the formation of cavitation bubbles, scattering the incident laser beam [162]. It has been reported that energy shielding can play an important role at relatively high laser fluence [61, 162]. It has been reported that that the energy loss is estimated to be 30 to 70% of the total incident beam energy [81, 162-164]. This explains why the smallest cut depths were obtained with still and flowing water conditions compared to air and flowing air (Fig. 26). In the still water case, significant ablation debris suspended in the water layer was observed above the treatment region after the ablation process, and this debris can interfere with the incident laser beam, which further reduces the pulse energy reaching the targeted area. Consequently, shallower craters were produced using still water compared to flowing water (Fig. 26) [165].

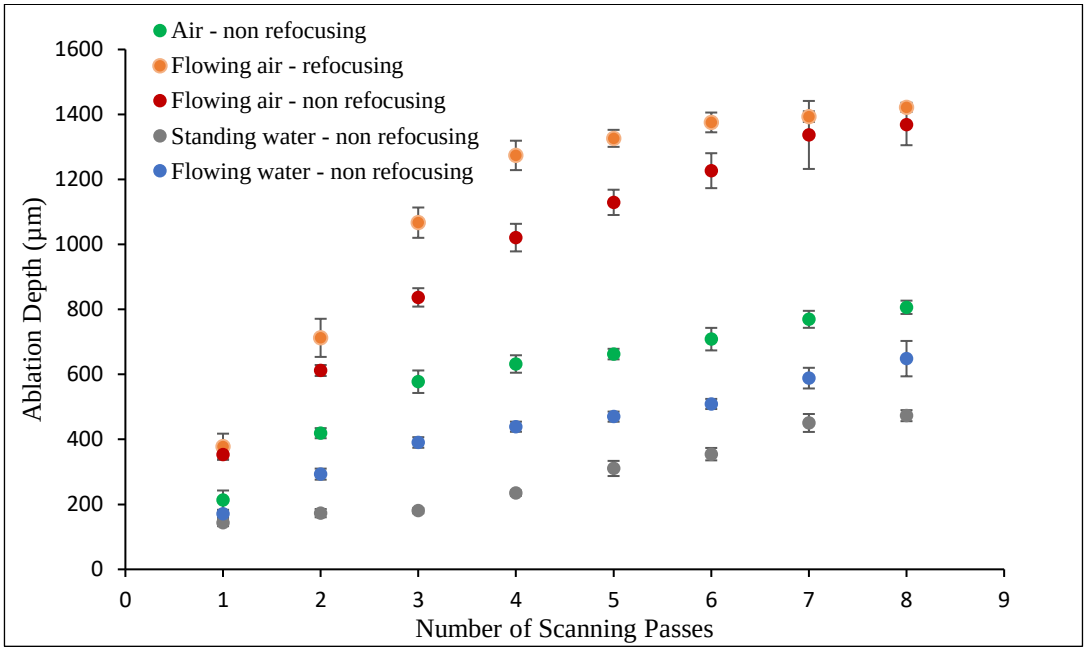

Figure 26: Ablation depth of the cavity as a function of the number of scanning passes for bovine bone under different experimental conditions using 15.3 J/cm^2 fluence, 200 µm/s scanning velocity, and 1 kHz repetition rate.

When ablating near the optical breakdown fluence, plasma shielding may play a role in the focal volume. At fluence much higher than the threshold (e.g. 10 x F_{th} in the present study), a larger plasma area is generated above the focus, thus a significant amount of the beam energy can be absorbed by the plasma formed before the beam waist [61, 163, 166]. To reduce the plasma shielding effect and thus increase the cut depth of the crater in water ablation, the target position with respect to the objective focal plane must be considered. Additional flowing water irradiation experiments were carried out to study the effect of the position of the target surface with respect to the focal plane of the objective. The position of the focusing lens was shifted over the Z-axis, and the laser fluence at the focal point was kept constant at 15.3 J/cm^2. The positive values of Z (the focus was below the sample surface) and negative values (the focus was the above the bone surface) were

investigated with different number of passes as shown in Fig. 27. The results show that the deeper cavities were achieved when the target is before the focal plane by 200 µm. The same behavior was observed by Sylvester et al., who reported that the highest amount of ablated material (weak plasma shielding) was found when the target was positioned slightly above the focal plane [164]. Tulea et al. also reported that the plasma shielding effect due to an optical breakdown in water was avoided when the target was before the focal plane [166]. Nonetheless, even though the deeper cut depth was obtained when target is posited above focal plane in water experiments, the air and flowing air conditions provide deepest cut depth at the same number of passes. Another way to reduce the plasma shielding effect is to remove the water layer away for ablation point during the process by air jet as Le et al done [131].

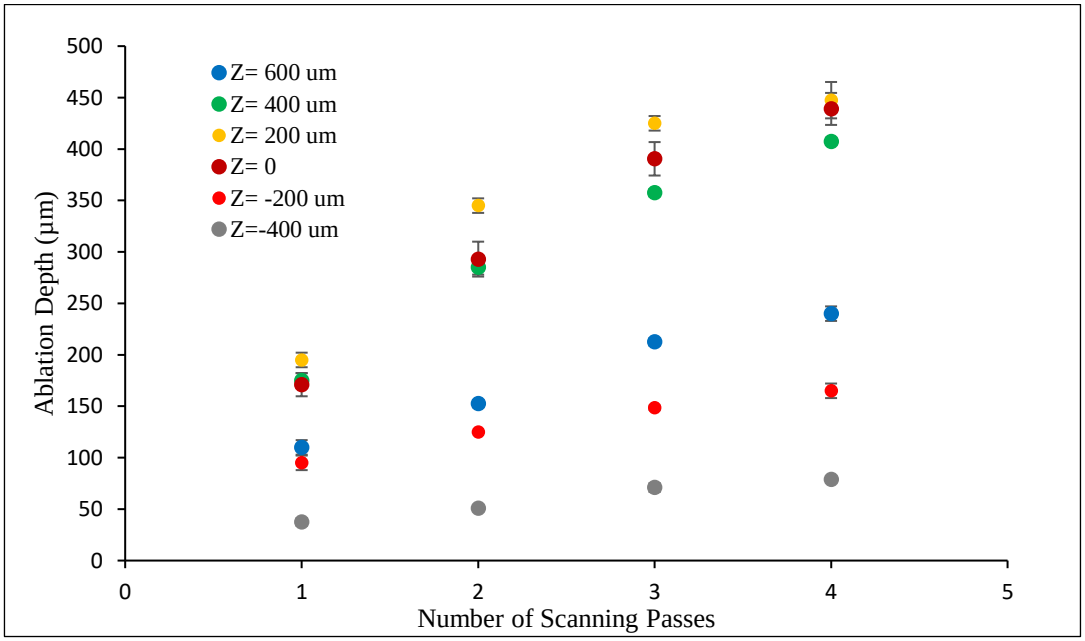

Figure 27: Ablation depth as a function of the number of scanning passes at different axial position of the focus position with respect to the bone surface under flowing water condition.

5.3.2 Ablation Rate

A key limitation of ultrafast lasers in orthopedic applications is the slow material removal rates (mm^3/s) [5]. In the present work, the enhancement of ablation rate under various experimental conditions was investigated. To measure the ablation rate, cavities with cross-section area of 1000×220 (μm^2) were produced in bone sample. The depth of the cavity under different conditions are a measure of the ablation rate. First, the ablation depth increases as after each additional scan passes (shown in Fig. 26). For all ablation conditions, the ablation rate decreased as the number of scanning passes increases (shown in Fig. 28): i.e. as the laser ablates deeper, it becomes less efficient in removing materials. This is attributed to that the increase in scanning passes produced a debris layer that resulted in the reduction of laser intensity [167, 168].

As shown in Fig. 28, the highest ablation rate was achieved using flowing air-assisted ablation compared to the other three conditions. With air flow, the ablation rate is about 1.6 times higher than without blowing air. This is attributed to ablation debris being removed away from the treatment area during the ablation process by the flowing air. In the air only case, a thick debris layer was observed in the processing area after ablation regardless the number of scanning passes. The debris blocks the laser energy from reaching the targeted ablation volume by absorbing and scattering the incoming pulses.

In the flowing water case, even though debris effect was visibly absent, a lower ablation rate was found compared to those of air or flowing air. Ablation accompanies with flowing water removed ~ 20% and 50 % less material (by volume) per second than those

of the air and air flow processes, respectively. The slowest ablation rate was observed when a still water layer was used. The decrease in the ablation rate under water (flowing or not) can be explained by the influence of plasma shielding during ablation process [161, 162, 166].

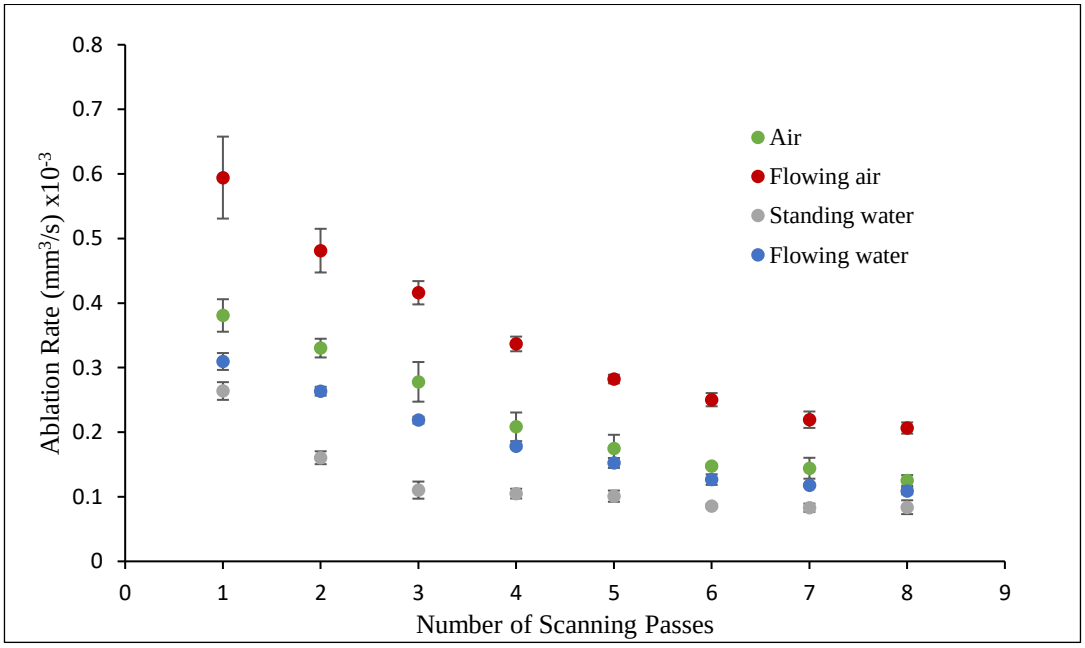

Figure 28: Ablation rate as a function of the number of scanning passes for bovine bone under air, flowing air, still water and flowing water and without refocusing objective lens using 15.3 J/cm^2 fluence, 210 fs pulse duration, 200 µm/s scanning velocity, and 1 kHz repetition rate.

5.3.3 Surface Morphology

The surface morphology characterization was performed using scanning electron microscope (SEM). The ablation pattern produced cavities with depths of 632 µm (air), 1021 µm (air flow), 234 µm (still water), and 439 µm (water flow). Top-view SEM images of the ablation craters for the four conditions are depicted in Fig. 29. Even though high fluence (~10F_{th}) was applied, the overall view shows well-defined geometry and smooth cavity rims for all four environments. This can be explained by the fact that the amount of

ablated tissue per pulse (μm/pulse) is small, it increases two or three times (from ~1 to 2 or 3 μm/pulse) when the fluence increases from ablation threshold (F_{th}) to high fluence for femtosecond lasers [8, 122, 156]. However, it is reported that at high ablation rates (e.g. 300, 80, and 14 um/pulse for Er lasers, Ho:YSGG, and Nd:YAG, respectively), the crater edges become irregular and rough [17, 124, 127]. Compared to the cavity edges produced by only air or both water conditions (Fig. 29a, c, and d), cavities created by the air flow process showed smoother surfaces (Fig. 29b). The smoothness of air flow ablation could result from the relatively clean process (i.e., free of debris). In water experiments (Fig. 29c and d), the rougher crater edges come from the optical breakdown of water, which results in the cavitation bubbles leading to stronger pressure impact at the beginning and collapsing of bubble, which can mechanically affect the removal of molten tissue and ablation debris away from the cavity edges during ablation [169, 170].

In Fig. 29, the SEM images of the craters ablated using high fluence (~$10F_{th}$) showed the absence of mechanical surfaces damage such as cracks at the crater edges for all four experimental conditions. This indicates that using a femtosecond laser at high fluence and low scanning speed (200 μm/s) and repetition rate (1 kHz) is safe for the surrounding bone tissue under the four studied environments. The preservation of the surrounding tissue is highly desirable for various surgical applications such as preparing the bone for implants [170]. A few studies reported the formation of small microcracks around treated areas using femtosecond lasers when high pulse repetition rates and low scanning velocity were applied [168]. Large cracks in the range of hundreds of microns

were observed with short and long pulsed laser ablation (nanosecond to millisecond pulse widths) [17, 156].

In the non-flowing air case, a large amount of ablation debris was observed around the treatment area and at the bottom of the cavity. It was found that the debris amount increased with the number of scanning passes (more material removal). The debris accumulation layer did not adhere to the top surface of tissue and can be removed by air flow before the SEM imaging for characterization purpose [171]. As shown in Fig. 29a, the debris layer attaching to the side wall cavity cannot be removed after ablation [168]. With air flow, the cavity with a small aspect ratio (depth/width ≈ 3) did not show signs of debris material on its surface or its inner walls. However, at high aspect ratio (more than 3), some ablation debris accumulated at the bottom of the cavity (Fig. 29b). This is due to (shown in Fig. 25a) the air flow at a 45^{o} angle is not able to completely remove the ablation debris from the cavity with a high aspect ratio. A higher efficiency of removing debris during the ablation process can be achieved by setting the air flow angle to be more perpendicular to the tissue surface and using a higher air inflation. Experimentally, we found that using air flow to clean the treatment area during the ablation process produced cleaner cavities compared to those cleaned after ablation. In both water conditions, the craters were relatively clean without any debris in the treatment area as shown in Fig. 29c and d.

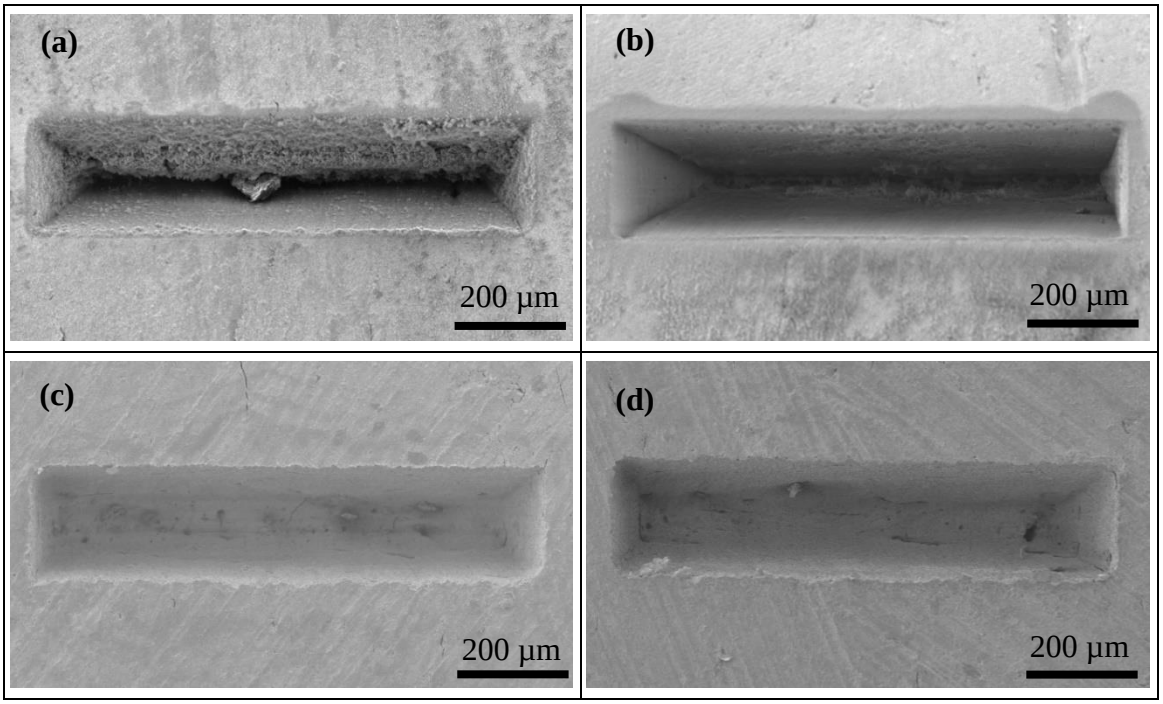

Figure 29: SEM images of craters in bovine bone performed by repeating a 1000x220 (μm^2) rectangular scanning pattern four times under; (a) air (cavity cleaned by air flow before image taken for characterization purpose), (b) compressed air flow, (c) still water, and (d) flowing water conditions, with laser fluence 15.3 J/cm^2, and scanning speed 200 µm/s.

To investigate the shape of the side walls and the bottom of the cavities, a high magnification SEM view of the cavities side wall (left side of the cavity shown in Fig. 29) is shown in Fig. 30. For all four environments, the morphology of the cavity walls appears to be uniform without surface ripples. A few studies reported that femtosecond laser ablation could induce ripples on inner wall surfaces [161, 172]. As shown in Fig. 30, the smoothest inner wall surface was produced with air flow (Fig. 30b), which can be a result of the clean ablation process induced by air flow-assisted ablation. In both underwater cases, the inner wall surface of the cavity was rougher (Fig. 30c and 30d). A possible explanation might be that the cavity acts as a trap to plasma expansion and confines

the hydrodynamic motion of cavitation bubbles in water, which generates high pressure impacts on the cavity walls [61, 161, 173].

For all investigated conditions, the floor of the craters has a well-defined geometry with sharp edges and corners. In air and air flow cases, a peak and valley pattern has emerged on the cavity bottom (not shown). In contrast, the floor of the crater of the water-assisted ablation was relatively flat with the presence of microcracks (Fig. 30c and b), which were resulted from the high pressure induced in the confined volume of water in the cavity [174].

After ablation, the bone samples were cut perpendicular to the ablation crater using a precision diamond wafering saw and examined under an optical microscope to investigate the cavity profile. In an ideal case, the cavity cross-sectional profile should look rectangular, with the same width from the top of the cavity to the bottom. In all experimental conditions, the cavities were showing a crater profile, which is wider near the top and narrower near the crater bottom. Wider cavity near the top was produced in both underwater experiments compared to those of in air and air flow. The same result was reported by Ren and Charee [173, 174]. For all environments, it has been seen that the crater profile has a ’V’ shape, when aspect ratio (depth/width) is greater than two as shown in Fig. 31a and b. In contrast, the cavity profile becomes a ’U’ shape when aspect ratio is two or less as depicted in Fig. 31c and d. Several factors may contribute to such crater profiles. First, when the crater goes deeper, the laser beam energy is attenuated due to the large focus angle [130]. Second, the ablated materials cannot escape from the deep crater

fast enough and thus they absorb and scatter laser beam [158]. Third, during large-scale tissue removal, the beam could scatter from the sidewall to the structure center [175].

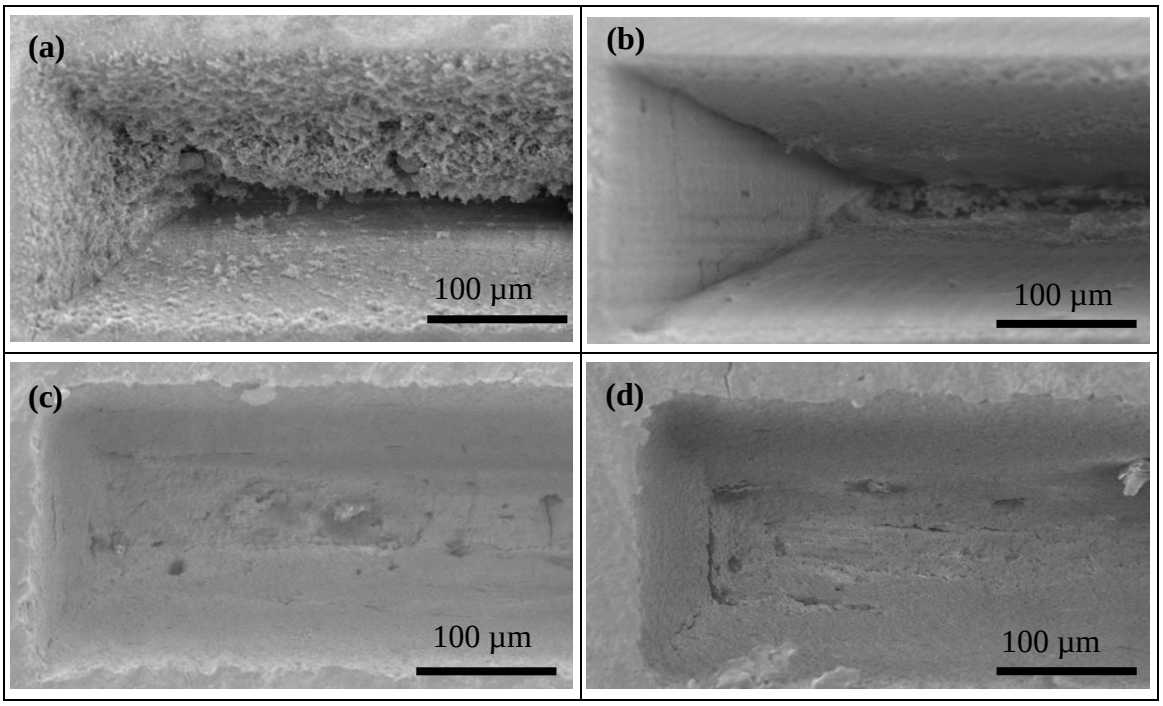

Figure 30: A higher magnification SEM view of the left side craters in bovine bone ablated by repeating the scanning pattern four times at 15.3 J/cm^2 fluence and 200 µm/s traverse speed under; (a) air, (b) compressed air flow, (c) still water, and (d) water flow conditions.

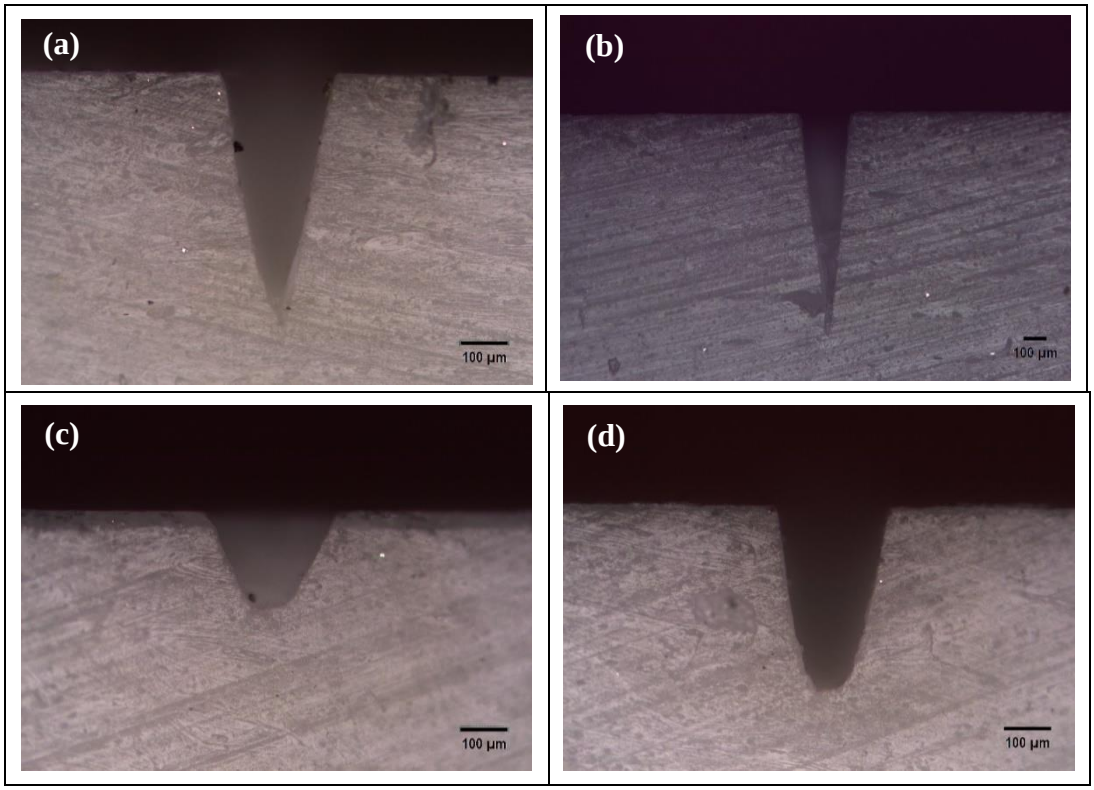

Figure 31: Cross-section optical microscope images of craters on the bone ablated by repeating rectangular scanning pattern four times over the sample surface with 15.3 J/cm^2 fluence, and 200 µm/s scanning speed under; (a) air, (b) compressed air flow, (c) still water, and (d) water flow conditions.

5.3.4 Thermal Side Effects

One of the main advantages of femtosecond laser ablation is the absence of undesired thermal side effects. The beam energy deposited by the femtosecond laser pulses does not have enough time to move into the bulk of the sample because the thermal relaxation time for biological tissue is in the order of nano- to microseconds. Thus, for ultrafast ablation using focused light, the absorbed thermal energy and associated damage are confined within the focal volume. The thermal energy diffusing beyond the ablation focus volume are generally negligible [131, 151, 155, 176]. Nonetheless, the presence of thermal effects from femtosecond laser ablation have been reported, including the presence

of melting and carbonization [127, 148, 161, 177]. In the present work, the thermal side effects of femtosecond laser ablation under different conditions was examined using a confocal Raman microscope. Raman spectra were obtained over the wavenumber range of 400 to 3200 cm^{-1} from the untreated sample (blue curve), and ablated sample as shown in Fig. 32. For comparative purposes, the spectrum of an untreated sample was measured. All the Raman bands recorded in the spectra of examined samples were assigned to bone compositions. No new phases such as amorphous carbon peak at 1580 and 1350 cm^{-1} were observed due to the laser ablation under different conditions which indicate that no carbonization occurred [177]. For all Raman spectra of samples, the clear peaks around 430 cm^{-1}, 591 cm^{-1}, and 960 cm^{-1} were observed correspond to the phosphate inorganic component. The spectra present the v_1 vibration band of CO_3^{2-} at 1070 cm^{-1} and the bending vibration band of the HPO_4^{2-} ion at 1453 cm^{-1} correspond to carbonate and phosphate mineral components, respectively. The two peaks at 1250 cm^{-1} and 1678 cm^{-1} provide evidence of existing the organic collagen protein, the amide I and III. The carbon-hydrogen (C-H) bond was observed at 2940 cm^{-1} corresponded to organic component of bone. This indicates that using low scanning velocity (200µm/s) and repetition rate (1 kHz) at high fluence (~$10F_{th}$) is safe for femtosecond laser ablation, and adjacent bone tissue is not thermally affected.

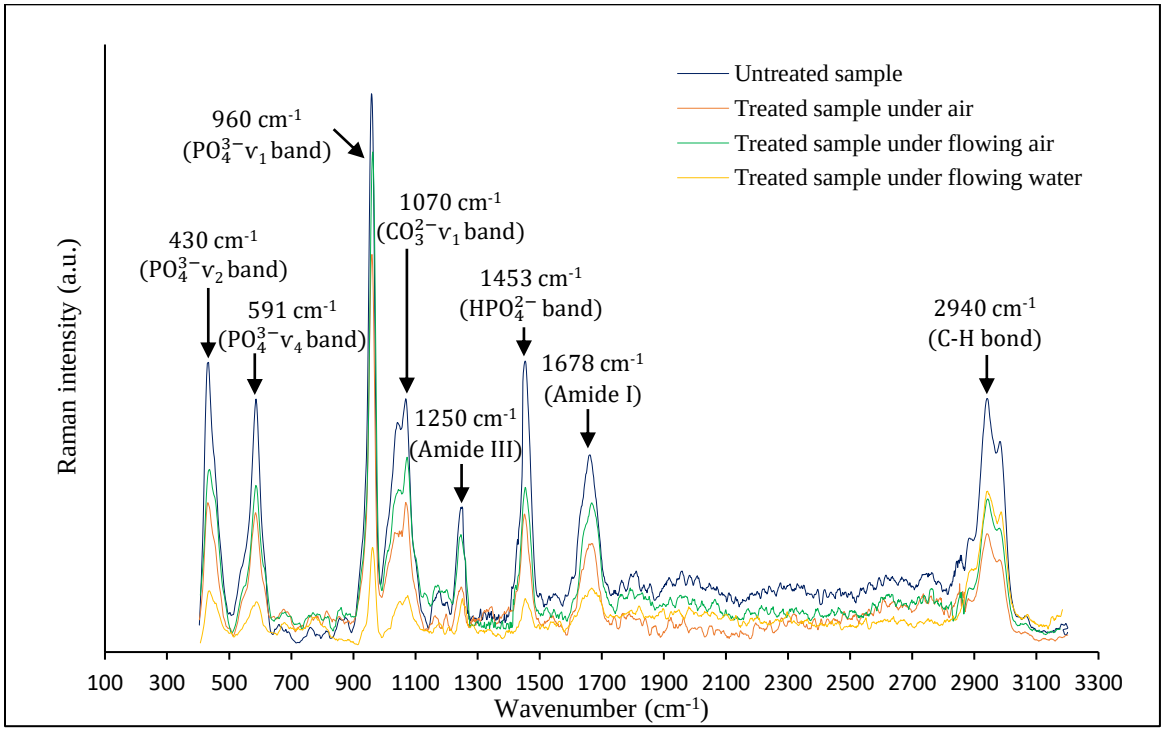

Figure 32: Raman spectra of bovine bone sample before and after treatment under different conditions showing the major bands corresponding the organic and inorganic bone components.

Chapter 6: Characterization of fiber laser and processing ablation parameters

6.1 Introduction

As stated earlier, a lot of material needs to be removed during orthopedic procedures, but femtosecond pulse lasers can only remove small amounts of hard tissue per pulse. Neev and Squier could only remove ~1 μm of tissue per pulse using a Ti:Sapphire laser with a fluence of 3 J/cm^2 [24]. A higher fluence could result in faster ablation. The present study revealed that as fluence increases to 22 J/cm^2, the ablation rate also increases to 3.8 μm/pulse, as shown in Fig. 20b from Section 4.2.2.2. Still, even the highest ablation rates achieved with femtosecond pulse lasers pale in comparison to those of other lasers, such as the Er:YAG laser (300 μm/pulse) [115]. Even with high fluence, femtosecond pulse laser ablation is slow.

Ultrashort laser ablation speeds must reach a level comparable to that of the mechanical tools currently used in orthopedic procedures. High repetition rates could bring them closer to achieving this feature. Most experiments on ultrashort lasers used an oscillator and regenerative amplifier configuration operating at low repetition rate (in the kHz range). With this limitation, solid state ultrashort lasers could not be used in practice. However, recent advances in laser technology have made ultrashort fiber lasers smaller, lighter, and more powerful, with higher repetition rates. This new generation of lasers can ablate tissue with precision, efficiency, and minimal collateral damage, making them well-suited for orthopedic surgery.

Despite the advantages of high repetition rates, there are two concerns worth discussing. First, high ablation rates can cause thermal damage. If the repetition rate is high enough, heat accumulates faster than it dissipates, resulting in carbonized tissue [178] and irreversible nerve damage, which occurs at lower temperatures than those required for carbonization [156, 179]. When nerves are close to the ablated area, the temperature must not exceed that threshold. Second, lasers with high repetition rates can create plumes of ejected material and plasma that block subsequent pulses and reduce ablation efficiency. When using a high repetition rate, the plasma should be given enough time to dissipate [8].

With the right laser and processing parameters, collateral damage and plumes of ejected material can be minimized. This chapter explores the effects of beam diameter, repetition rate, scanning speed, and number of successive passes on the ablation process. An ultrashort fiber laser (λ = 1035 nm, τ = 1.0 ps, repetition rate 100 kHz to 1 MHz) was used for all of the experiments in Chapter 6.

6.2 The effect of beam diameter on the ablation process

6.2.1 Method

To study the effect of beam diameter on ablation, three different focal lenses (125, 50.2, and 200 mm) were used to focus the laser beam's diameter from 4 mm (FWHM) to 41.0, 16.4, and 3.0 µm, respectively, on the sample surface. Multiple grooves were ablated on the sample surface using the ultrashort fiber laser setup in Fig. 13 (Section 3.2.2) at fluences of 1.5, 3.0, and 4.5 J/cm^2. All three fluences were used with each focusing lens. The scanning speed and repetition rate were set to 100 µm/s and 100 kHz, respectively. A

reflected-light microscope captured images, shown in Fig. 33, of the ablated grooves from a top-down and cross-sectional view.

6.2.2 Results and discussion

When the beam was focused to diameter of 41.0 μm, it created the widest grooves at all fluences. The channels were 75, 95, and 120 μm wide at fluences of 1.5, 3.0, and 4.5 J/cm^2 respectively, as shown in Fig. 33a. As fluence increased, so did groove depth. The grooves in Fig. 33b were 150, 330, and 410 μm deep at 1.5, 3.0, and 4.5 J/cm^2. The 41.0 μm beam diameter also produced more carbonized and melted bone, as did the 16.4 μm diameter, whose results can be found in Fig. 33c. The channels were approximately 4, 5, and 5.6 times wider than the beam diameter (16.4 μm) at fluences of 1.5, 3.0, and 4.5 J/cm^2 respectively. These fluences produced grooves with depths of 70, 110, 150 μm, as shown in Fig. 33d. When the focal point was 3.0 μm in diameter, the laser produced a clean, shallow channel whose width roughly equaled the diameter of the spot. These grooves can be seen in Fig. 33e and f.

The wide, deep channels produced by diameters of 41.0 and 16.4 μm on the target surface were caused by overlapping laser pulses. Beam diameter, repetition rate, and scanning speed determine the effective number of incident pulses per spot, as illustrated in Eq. 6 (Section 4.2.2.1). Diameters of 41.0, 16.4, and 3.0 μm resulted in 25630, 10250, and 1875 respective pulses per spot. Large diameters (41.0 and 16.4 μm) cause the pulses to overlap, sending more energy to each spot. Energy and heat accumulate inside the tissue, reducing the ablation threshold for subsequent pulses and removing additional material

[180, 147]. Heat accumulation also causes severe thermal damage on the cavities' edges, as shown in Fig. 33a-d. The damage only gets worse as beam diameter increases. Smaller beam diameters (3.0 μm) cause less thermal damage, but they also remove less tissue. When massive amounts of tissue need to be removed, larger beam diameters are more appropriate. The resulting carbonized tissue can be removed using mechanical tools. Smaller beam sizes or high scanning speeds (less pulse overlap) can precisely remove smaller amounts of tissue with minimal collateral damage.

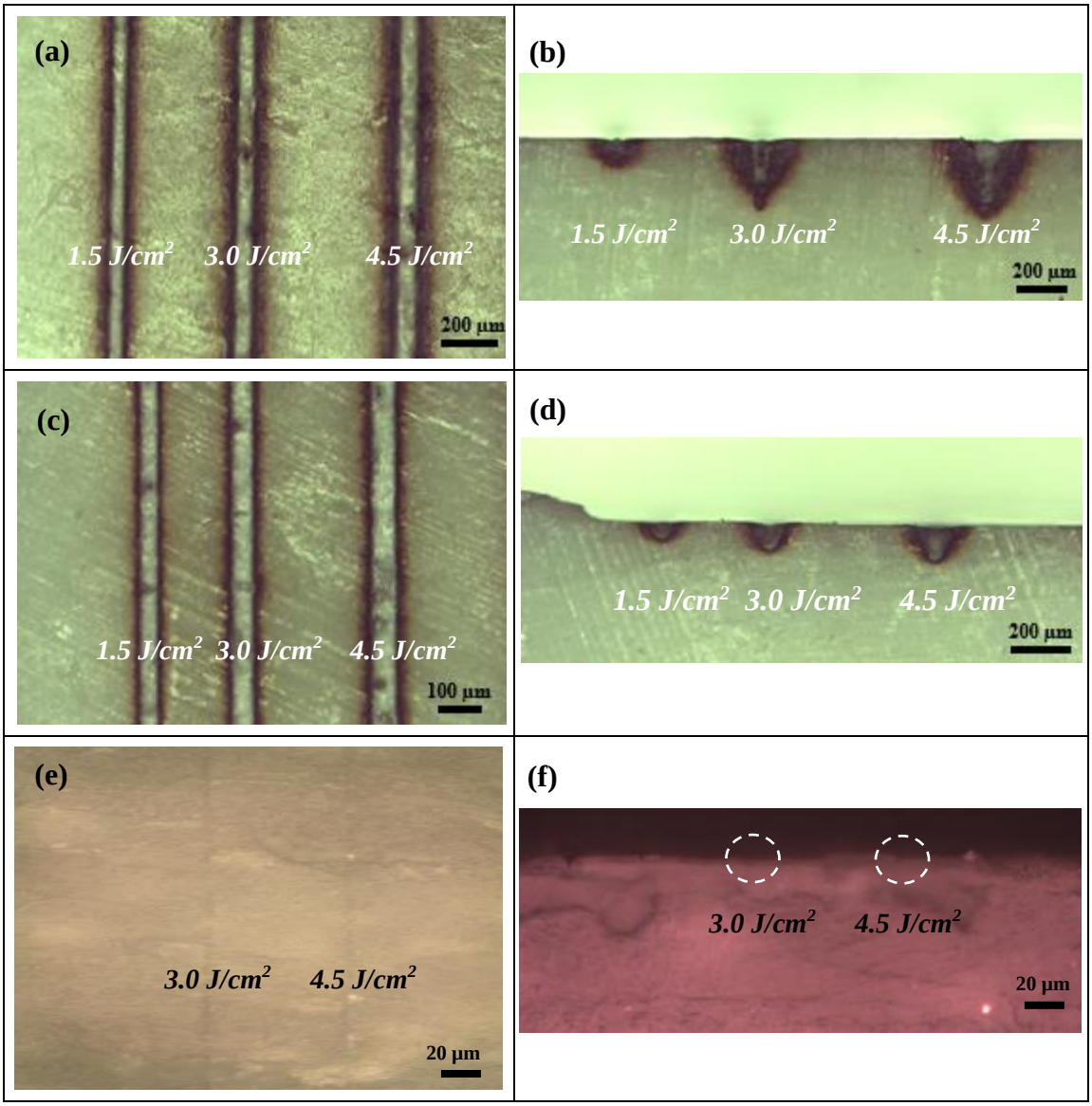

Figure 33: Grooves created using an ultrashort fiber laser (λ = 1035 nm, τ = 1.0 ps, repetition rate 100 kHz) at fluences of 1.5, 3.0, and 4.5 J/cm^2 and various beam diameters. (a) and (b) provide top and cross-sectional views of channels ablated using a 41.0 µm diameter beam. The grooves in (c) and (d) were created by a 16.4 µm diameter beam. As for (e) and (f), the grooves were ablated using a 3.0 µm diameter beam.

6.3 The effect of repetition rate on ablation depth

6.3.1 Method

The relationship between repetition rate and ablation depth was studied using different laser fluences. Multiple grooves were ablated using repetition rates of 100, 250,

and 500 kHz. Fluences ranged from 5 to 20 J/cm^2. An objective lens (50x, N.A = 0.42, Plan Apo NIR Infinity, Mitutoyo) focused the laser beam into a spot with a diameter of 3.0 μm, and the translation stage speed was set to 1 mm/s.

Every experiment in Section 6.3, 6.4, and 6.5 has several things in common. These experiments used the ultrashort fiber laser setup (pulse duration 1.0 ps, wavelength 1035 nm) shown in Fig. 13 (Section 3.2.2). Three trials were carried out for each set of values under investigation. For example, in this experiment, three trials were conducted for every combination of repetition rate and laser fluence. The channels were 3000 μm long, with 200 μm between each channel. A cross-section of the ablated sample was made using a diamond-blade saw, and the channels were measured using light microscopy.

6.3.2 Results and discussion

In Fig. 34a, ablation depth is plotted as a function of laser fluence for each repetition rate. It is clear that for all examined repetition rates, groove depth positively correlates with fluence. For example, at 500 kHz and 20 J/cm^2, the removal depth was 2.2 times higher (12 versus 27 μm) than at 5 J/cm^2. The same relationship was observed between fluence and ablation rate in Fig. 34b, where the removal rate at 500 kHz increased from 0.013 to 0.029 μm/pulse in going from fluences 5 to 20 J/cm^2. Higher fluences deposit more energy into the tissue, explaining the relationship between ablation and fluence.

Ablation depth increased with repetition rate, as seen in Fig. 34a. The ablation depth at 5 J/cm^2 and 500 kHz is approximately 3.4 times higher than the depth achieved at 100 kHz. This occurs because higher repetition rates apply more pulses per spot, irradiating the

tissue with more total energy. Further, hard tissue's ablation threshold decreases with pulse rate as found in section 4.1 [147]. Fig. 34b shows that a repetition rate of 100 kHz results in a significantly higher ablation rate per pulse than 500 or 250 kHz. High repetition rates generally cause the debris shielding effect outlined in Section 4.2.3.2, reducing the ablation rate per pulse.

Orthopedic surgeons need to remove tissue quickly, so the repetition rate of a laser ablation system needs to be as high as possible without causing debris shielding. The repetition rate should also be low enough to prevent heat accumulation, which can melt or carbonize tissue [130, 178]. Plasma shielding is also a concern [181]. The next chapter investigates the relationship between fluence and repetition rate in greater detail.

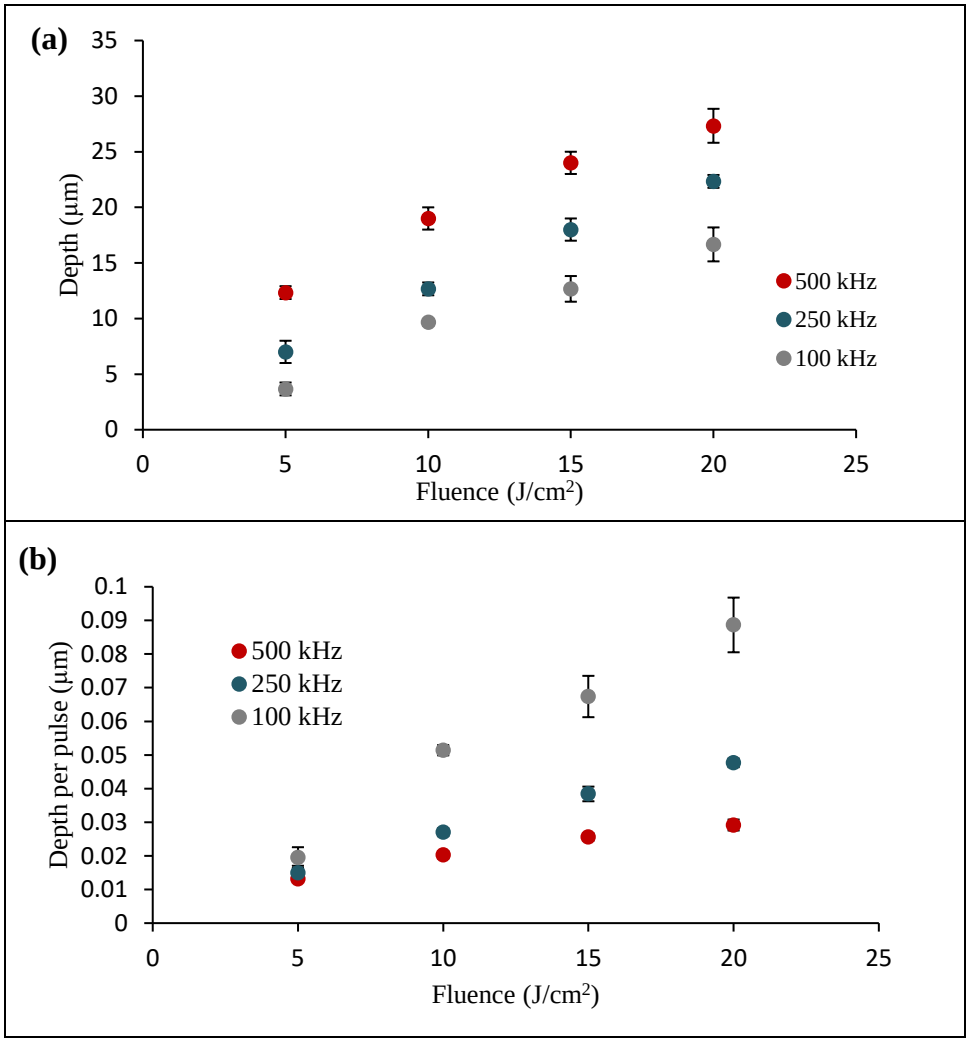

Figure 34: (a) Ablation depth and (b) removal rate (µm/s) at laser fluences ranging from 5 to 20 J/cm^2 , as well as three different repetition rates (100, 250, and 500 kHz). This experiment used an ultrashort fiber laser (λ = 1035 nm, τ = 1.0 ps) with a scanning speed of 1 mm/s.

6.4 The effect of scanning speed on ablation depth

6.4.1 Method

This experiment used an ultrashort fiber laser (repetition rate 100 kHz) at various scanning speeds (100 – 2000 µm/s) and two different fluences (10 and 20 J/cm^2) to ablate multiple grooves on polished bone samples. The goal was to record removal depth and rate (µm/pulse) as a function of scanning speed. Scanning speed refers to the number of incident

pulses per spot, which were calculated using Eq. 6 (Section 4.2.2.1) and are shown in Table 6. The beam was focused to a point with a diameter of 3.0 µm ($1/e^2$) using an objective lens (50x, N.A = 0.42, Plan Apo NIR Infinity, Mitutoyo).

Table 6: The number of incident pulses per spot at different scanning speeds, with a spot size diameter of 3.0 µm and a repletion rate of 100 kHz.

Scanning speed *(µm/s)*	Effective pulse number
100	1875
500	375
1000	187
1500	125
2000	94

6.4.2 Results and discussion

In Fig. 35a, groove depths are charted as a function of scanning speed at two different laser fluences. The lower of the two fluences (10 J/cm^2) resulted in shallow channels, which became deeper as scanning speed decreased. This happens because lower speeds allow more incident pulses to hit each spot, reducing the tissue's ablation threshold [182]. The effect is similar to the overlapping mechanism described in Section 6.2.2. At 20 J/cm^2, scanning speed had little effect on ablation depth, as shown in Fig. 35a. This can be explained by the shielding of the incoming laser pulse by the plume, which reduces the ablation efficiency [127, 182].

Fig. 35b shows removal rate per pulse as a function of scanning speed at two different fluences. For both fluences, ablation rate increased with scanning speed. For example, at 20 J/cm^2, the ablation rate per pulse increased from 0.01 µm/pulse at 100 µm/s to 0.15 µm/pulse at 2000 µm/s. These results suggest that higher scanning speeds lead to higher ablation efficiency per pulse.

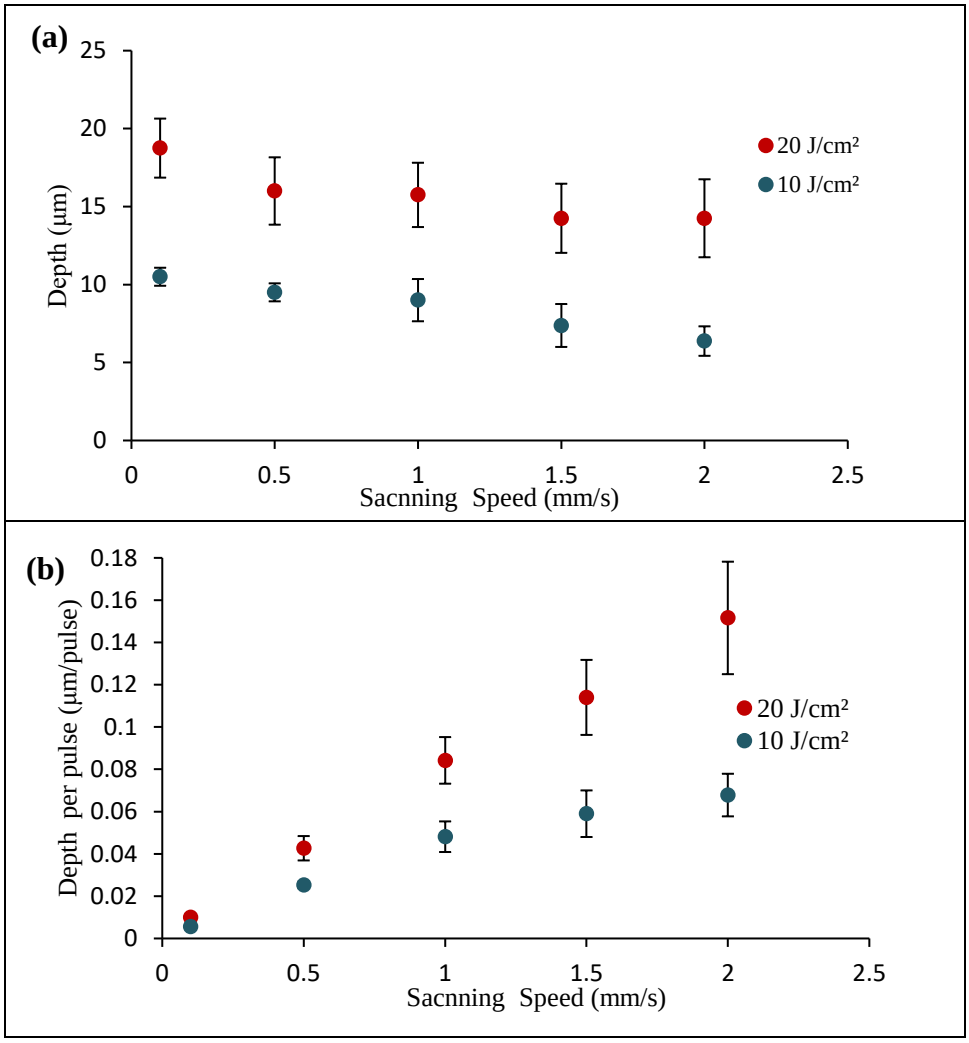

Figure 35: (a) Total groove depth and (b) removal rate as function of scanning speeds ranging from 100 to 2000 µm/s at two different fluences using an ultrashort fiber laser (λ = 1035 nm, τ = 1.0 ps, repetition rate 100 kHz).

6.5 The effect of multiple passes at various focal positions on ablation depth

6.5.1 Method

To remove the amount of material required for orthopedic and dental work, the laser beam must pass over the same target many times, with the objective lens refocusing each time. This section examines the effect of successive pass number on groove depth. Multiple

channels were ablated on the sample surface using different numbers of passes (5, 10, 15, and 20), with a laser fluence of 10 J/cm^2 and a scanning speed of 2000 µm/s. An objective lens (50x, N.A = 0.42, Plan Apo NIR Infinity, Mitutoyo) focused the laser beam to a diameter of 3.0 µm. The Rayleigh length (7.0 µm) was calculated using Eq. 2. To find a relationship between removal depth and focal position, the laser's focal point was lowered in the Z-direction (towards the sample) once every five passes. In each trial, the focal point was lowered at different intervals (5, 10, or 15 µm), as shown in Fig. 36. For example, in the first trial, the focal position was lowered by 5 µm once every five passes. This study used the ultrashort fiber laser setup in Fig. 13 (Section 3.2.2) with a repetition rate of 100 kHz.

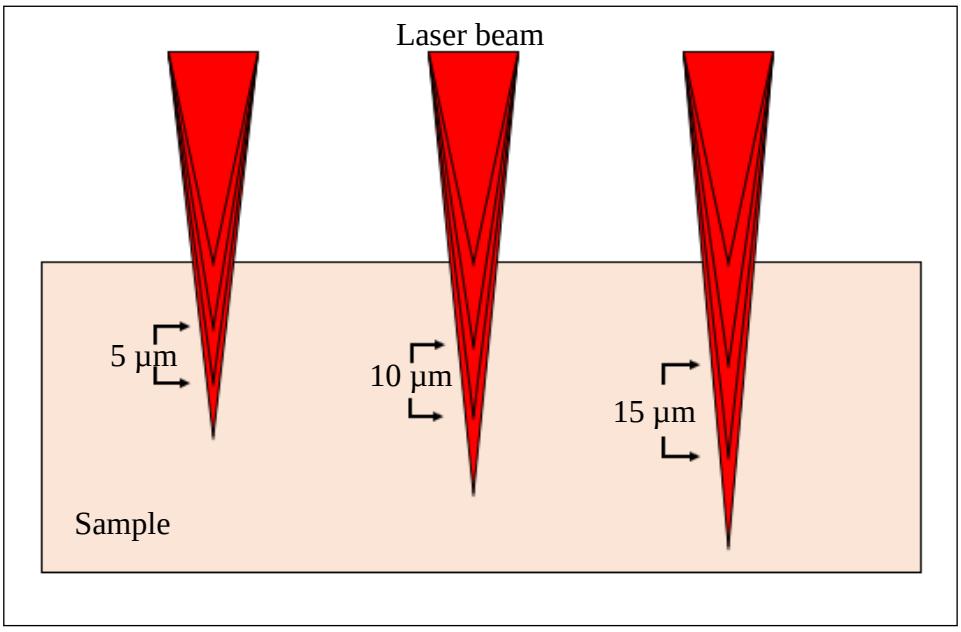

Figure 36: Image of the focal position at three distances. The focal point was lowered three times, once every five passes, at three different intervals (5, 10, and 15 µm). There were 20 passes in total.

6.5.2 Results and discussion

Channel depth was graphed a function of pass number in Fig. 37. At all three refocusing intervals, depth increased with additional passes. Depth increased faster when the focal position was lowered at 10 µm intervals. After five passes, the channels were 15 µm in depth in all trials, as the focal position had not yet been changed. When the focal point was lowered by 5, 10, and 15 µm, the depth increased to 17, 31, and 24 µm, respectively. This suggests that the focal position plays a significant role in ablation efficiency. Still, the laser created 15 µm deep grooves after five passes without refocusing, even though the total Rayleigh length for the objective lens was small (Z_R = 3.5 µm). This is likely due to the high laser fluence used (10 J/cm^2).

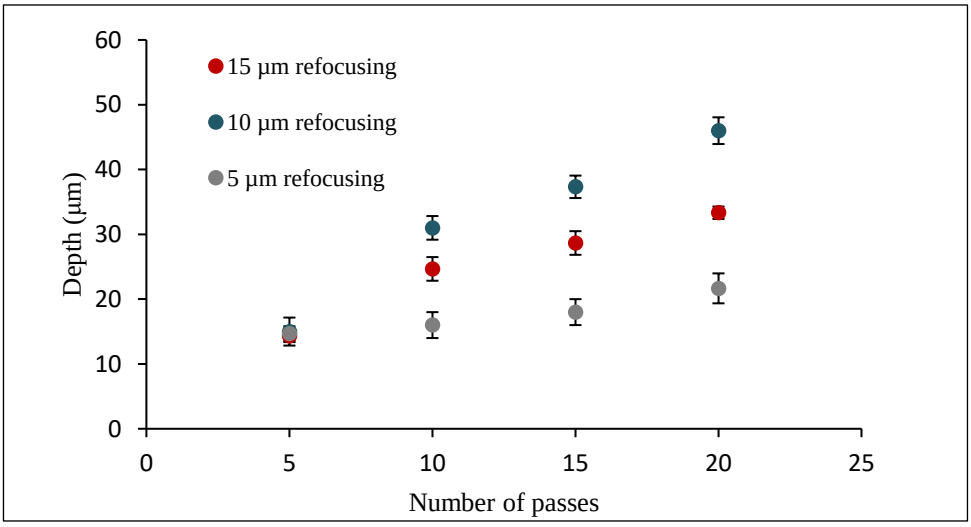

Figure 37: Groove depth as a function of pass number at different refocusing intervals (5, 10, and 15 µm) using an ultrashort fiber laser (λ = 1035 nm, τ = 1.0 ps, repetition rate 100 kHz). Fluence and scanning speed were set to 10 J/cm^2 and 2000 µm/s respectively.

Chapter 7:Cavity preparation in bone by ultrashort fiber laser under dry and water experimental conditions

7.1 Cavity preparation under dry condition

7.1.1 Introduction

Lasers are more precise and cause less collateral damage than mechanical tools, leading to better outcomes for patients [183-185]. This makes ultrashort laser ablation an attractive area of study. Ultrashort lasers cannot yet be used in practice, as they are far slower than mechanical cutting tools. However, Chapter 6 demonstrated that specific fluences, repetition rates, focal positions, and scanning speeds can increase the ablation rate without compromising precision.

High fluences and repetition rates increase ablation efficiency, but they also can cause laser pulses to overlap. Heat accumulates faster than it can dissipate, leading to carbonization and irreversible cellular damage [180, 186]. Repetition rates above 100 kHz can also create a lot of debris, reducing ablation efficiency [187-189]. If the time between pulses is reduced to only a few microseconds, the resulting debris shields the tissue from successive pulses [190]. These results highlight the importance of carefully selecting fluence and repetition rate.

This chapter aims to find the best possible repetition rate and fluence for ultrashort laser ablation of hard tissue. First, the effects of fluence and repetition rate on ablation rate (the volume of hard tissue removed by the laser per unit of time, mm^3/s) was studied.

Second, SEM images were used to determine the effects of repetition rate on ablation quality, indicated by the appearance of the remaining tissue. Third, the relationship between pulse rate and surface roughness of ablated cavities was examined. Finally, the fourth investigation studied the effect of laser ablation on the chemical components of bone.

7.1.2 Method

The ablation experiments used the setup illustrated in Fig. 13 (Section 3.2.2). A fiber laser (wavelength 1035 nm, pulse duration 1 ps,) ablated rectangular cavities (1000 µm long and 200 µm wide) at repetition rates of 100-800 kHz, with fluences ranging from 5 to 30 J/cm^2. Three trials were carried out for each combination of fluence and repetition rate. The tissue was scanned in a raster pattern, illustrated in Fig. 38. Scanning lines were 1000 µm long, with 4 µm between each line. The beam made 30 scanning passes. Once every five passes, the beam's focus was lowered by 10 µm in the Z-direction. Scanning speed was set to 2000 µm/s, with a spot size diameter of 4 µm.

A diamond wafering saw was then used to cross-section the tissue samples parallel to the width of the scanning pattern and perpendicular to the bone sample. The cavities were measured using a reflected light microscope and J-image software. Ablation rates (mm^3/s) were then calculated from the area of each cavity. Infinite focus microscopy and scanning electron microscopy (SEM) were used to characterize surface morphologies. Before and after ablation, Raman analyses and energy dispersive X-rays were performed on samples to look for changes in their chemical composition or structure.

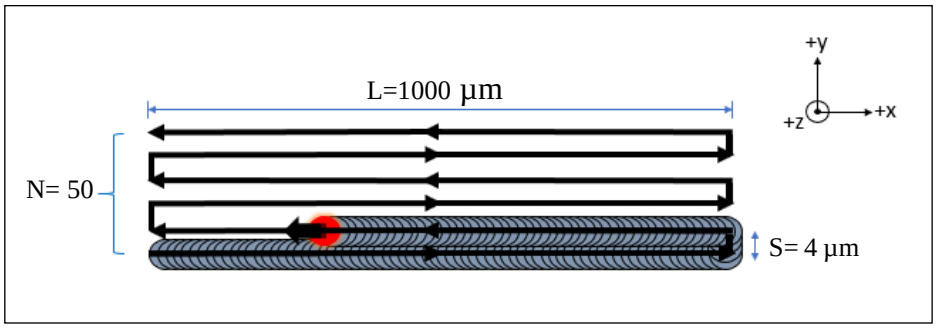

Figure 38: Schematic of the laser's path. L = scanning line length; N = number of scanning lines in one scanning pass; and S = scanning line spacing.

7.1.3 Results and discussion

7.1.3.1 Ablation rate

Fig. 39 illustrates the effect of fluence and repetition rate on ablation rate. At repetition rates of 100-600 kHz, the ablation rate increased significant with fluence. For example, at 600 kHz, the ablation rate increased from $0.42x10^{-4}$ to $0.64x10^{-4}$ mm^3/s as fluence increased from 5 to 30 J/cm^2. Schelle et al. observed the same relationship using an Nd:YVO_4 laser with a pulse duration of 8 ps, a wavelength of 1064 nm, and a repetition rate 500 kHz. They found that the ablation rate increased five fold as fluence increased from 2 to 7 J/cm^2 [191]. However, Chen et al. noted a reduction in ablation efficiency when laser fluence exceeded 4.7 J/cm^2 using a thin-disk femtosecond laser (wavelength 1025 nm, pulse width 400 fs, repetition rate 30 kHz) on dentin [167]. This reduction was likely caused by plasma shielding, which occurs when the laser's fluence greatly exceeds the tissue's ablation threshold [192]. When plasma accumulates, it can absorb or reflect incoming laser photons, shielding the sample from additional pulses [172, 193]. The present study did not observe any significant plasma shielding, even at the highest fluence, 30 J/cm^2.

At 800 kHz, the laser instantly carbonized the sample, and all fluences produced irregularly shaped cavities that could not be measured. This finding will be explored further in the next section. A high scanning speed, more than 2000 µm/s, can increase the ablation rate (mm^3/s) even when using a low repetition rate as shown in Section 6.4.2. The translation stage in the present study, pictured in Fig. 13 (Section 3.2.2), could not exceed 2000 µm/s.

The graph in Fig. 39 shows that even when laser fluence doesn't change, ablation rate increases with repetition rate. At 5 J/cm^2, the ablation rate was 5 times greater at 600 kHz than 100 kHz. However, at 30 J/cm^2, the removal rate was only 2.6 times greater at 600 kHz than 100 kHz. The relationship between repetition rate and ablation rate can be viewed as a consequence of the heat accumulation effects described in Section 4.1.3.2. Femtosecond laser systems, such as Ti:sapphire laser, typically operate at 1 kHz, which is too low to cause significant heat accumulation. These effects become more severe at values exceeding 100 kHz [189]. As the repetition rate increases, heat accumulates in the ablation zone, thermally modifying the tissue therein. This thermal activation lowers the ablation threshold and increases the tissue's absorptivity, accelerating the ablation process [147, 194]. Liu and Niemz used a thin disk Yb:KYW laser (wavelength of 1030 nm, pulse duration of 900 fs) to study the effect of repetition rate on ablation rate [14]. Using pulse repetitions between 1 and 20 kHz, lower than in the present study, they also found that ablation rate increased with repetition rate. However, Schille et al. reported that ablation rate decreased with repetition rate beyond 5 MHz, likely due to plasma or particle shielding

[189]. In summary, this study achieved the highest ablation rate when using a repetition rate of 600 kHz and a fluence of 30 J/cm^2.

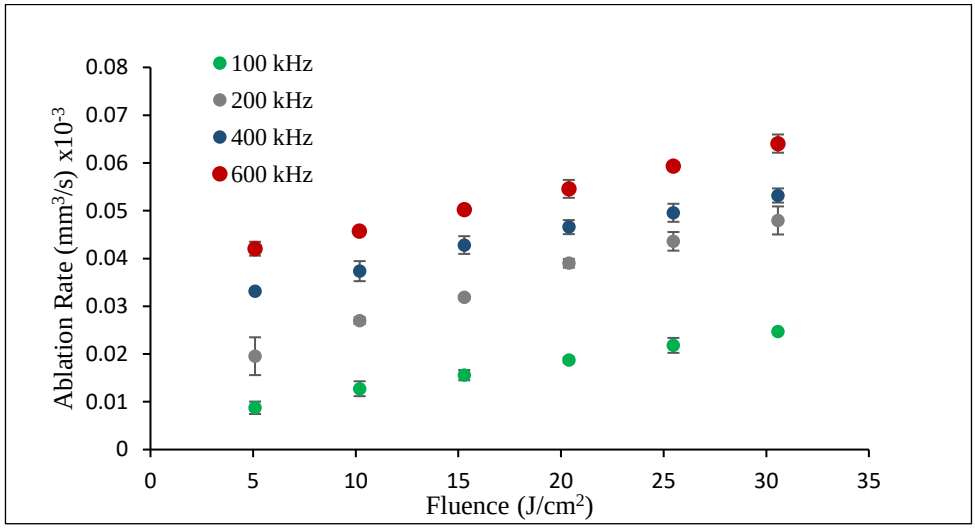

Figure 39: Ablation rate as a function of laser fluence at various repetition rates using a fiber laser (wavelength 1035 nm, pulse duration 1 ps).

7.1.3.2 Ablation quality

Quality and precision are important considerations in orthopedic surgery. This study used SEM to characterize the ablation quality of bovine bone samples, which were ablated with a fluence of 30 J/cm^2 and repetition rates of 100-800 kHz. Fig. 40 shows top-down views of each cavity. At 100-600 kHz (Fig. 40a-d), the cavities are precisely defined, with no visible microcracks, discoloration, melting, or carbonization around the edges. The ablation quality was poor at 800 kHz (Fig. 40e); cavity rims were irregularly shaped, and microcracks extended up to 300 µm around the ablated tissue, as did thermal damage.

This change in ablation quality was likely the result of heat accumulation. A portion of the laser's energy remains in the tissue after each pulse, and if the repetition rate falls between 100 and 600 kHz, the residual thermal energy will have time (1.6-10 µs) to

dissipate through the tissue, even though hard tissue has low thermal conductivity. This accelerates the ablation process. However, at 800 kHz, there is not enough time (1.2 µs) for heat to dissipate. As high heat accumulates, the surface temperature rises, causing serious thermal and mechanical damage [176, 190]. Also, the overlapping of pulses shows high impact factor on ablation quality. For example, at 600 kHz and 800 kHz, the effective pulse numbers are 750 and 1000 pulses, respectively. With spot overlap of 750 pulses on visible thermal effect was observed, low heat accumulation, compared to higher overlap of 1000 pulses. Thus, the repetition rate should be kept below 800 kHz to achieve good ablation quality at 30 J/cm^2 and 2000 µm/s. We have tried using fluences as low as 5 J/cm^2 to improve ablation quality at 800 kHz, but these attempts still ended with significant damage. The results of the present study suggest that increasing the scanning speed above 2000 µm/s can improve ablation quality.

Some studies have investigated the effect of repetition rate on ablation quality [128, 180, 186]. Using an ultrashort pulse laser with a wavelength of 1030 nm, a pulse duration of 320 fs, a focal spot diameter of 12.6 µm, and a scanning speed of 1000 µm/s, Gill et al. reported carbonization, and large fractures around the ablated area with a low repetition rate of 30 kHz [180], likely due to the high fluence they used (40 J/cm^2). Another study, carried out by Menezes et al., noted thermal damage when using a repetition rate of 50 kHz and a fluence of 40 J/cm^2 [186].

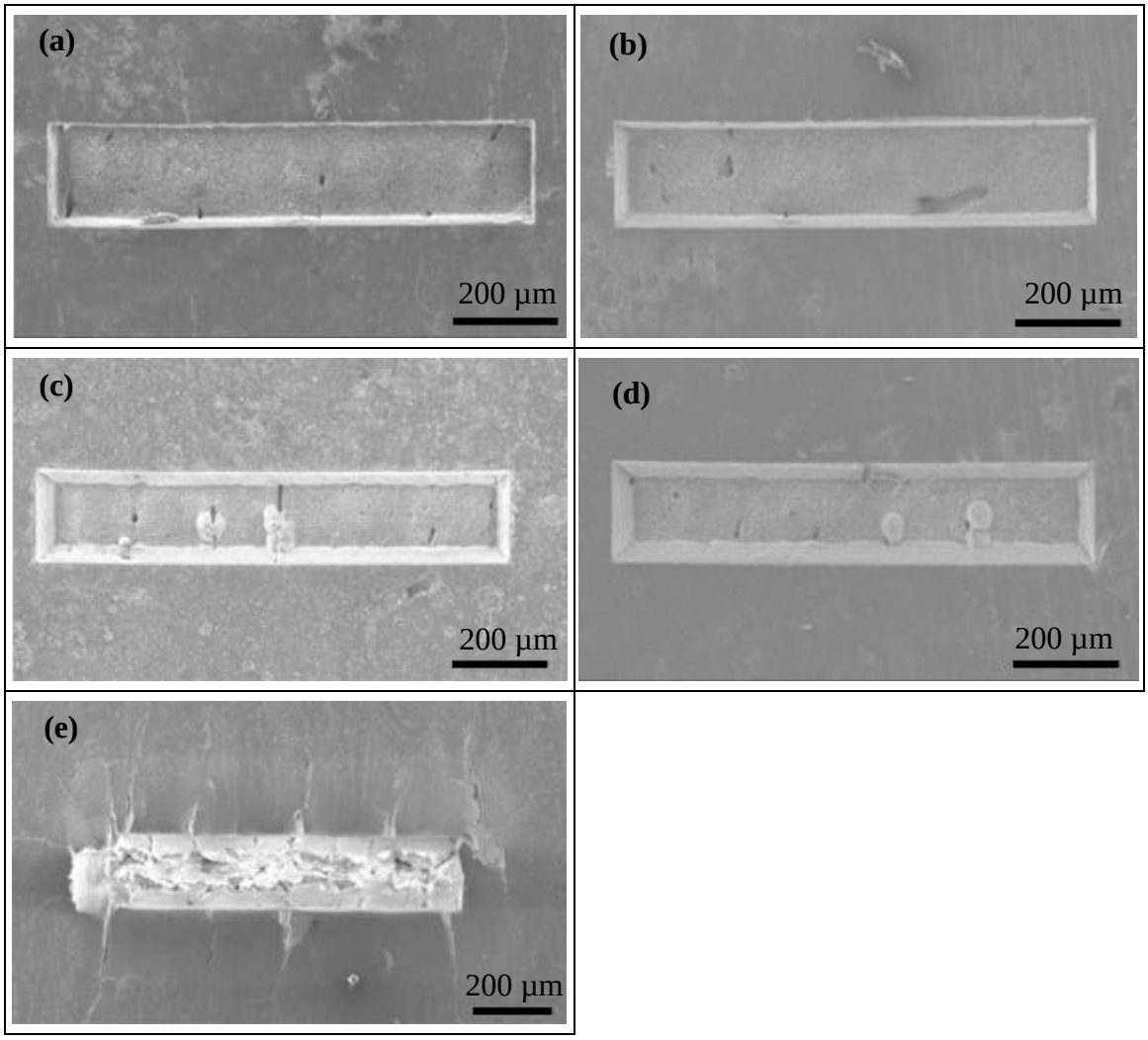

Figure 40: Top-down SEM images of cavities in bovine bone. The cavities were created by scanning a 1000x200 (μm^2) rectangular pattern 30 times at (a) 100 kHz, (b) 200 kHz, (c) 400 kHz, (d) 600 kHz, and (e) 800 kHz, with a fluence of 30 J/cm^2 and a scanning speed of 2000 µm/s.

7.1.3.3 Surface roughness

Orthopedic and dental surgeons often have to fill cavities in hard tissue with certain materials, such as dental composite resin [195, 196], which adhere more easily to rough surfaces [117, 197]. The next study analyzed the roughness of cavities ablated at 30 J/cm^2 and 100-600 kHz, with three cavities per repetition rate. Roughness was measured based on the surface's average roughness profile (Ra) and roughness depth (Rz). Ra refers to

peak-to-valley values of surface roughness within the measuring length, while Rz is the arithmetic mean value of the single roughness depths of consecutive sampling lengths. An untreated sample was used as a control after being polished with a series of SiC papers (80 and 320 grit). Since SEM examination is associated with a lack of quantitative investigation of the roughness values, infinite focus microscopy was used instead.

Fig. 41 shows three-dimensional trace maps of each sample's surface, and the mean roughness values are recorded in Table 7. The control sample's Ra and Rz were measured to be 0.28 ± 0.08 and 0.92 ± 0.15 µm respectively. The treated samples were far rougher. At 100 kHz, Ra and Rz equaled 0.44 ± 0.03 and 1.90 ± 0.11 µm. Similar values were obtained at 200 kHz, where Ra was 0.48 ± 0.01 µm and Rz was 1.98 ± 0.12 µm. The greatest roughness was achieved at 600 kHz; Ra equaled 0.67 ± 0.03 µm, and Rz equaled 2.51 ± 0.17 µm. Thus, high repetition rates produce rough surfaces, which greatly facilitate adhesion and mechanical interlocking between hard tissue and orthopedic or dental composites [117].

Table 7: Mean surface roughness for bone treated using 30 J/cm^2 at various repetition rates.

Samples	Surface roughness	
	Ra (µm)	Rz (µm)
	Mean ± SD	Mean ± SD
Control sample	0.28 ± 0.08	0.92 ± 0.15
Treated at 100 kHz	0.44 ± 0.03	1.90 ± 0.11
Treated at 200 kHz	0.48 ± 0.01	1.98 ± 0.12
Treated at 400 kHz	0.57 ± 0.05	2.37 ± 0.16
Treated at 600 kHz	0.67 ± 0.03	2.51 ± 0.17

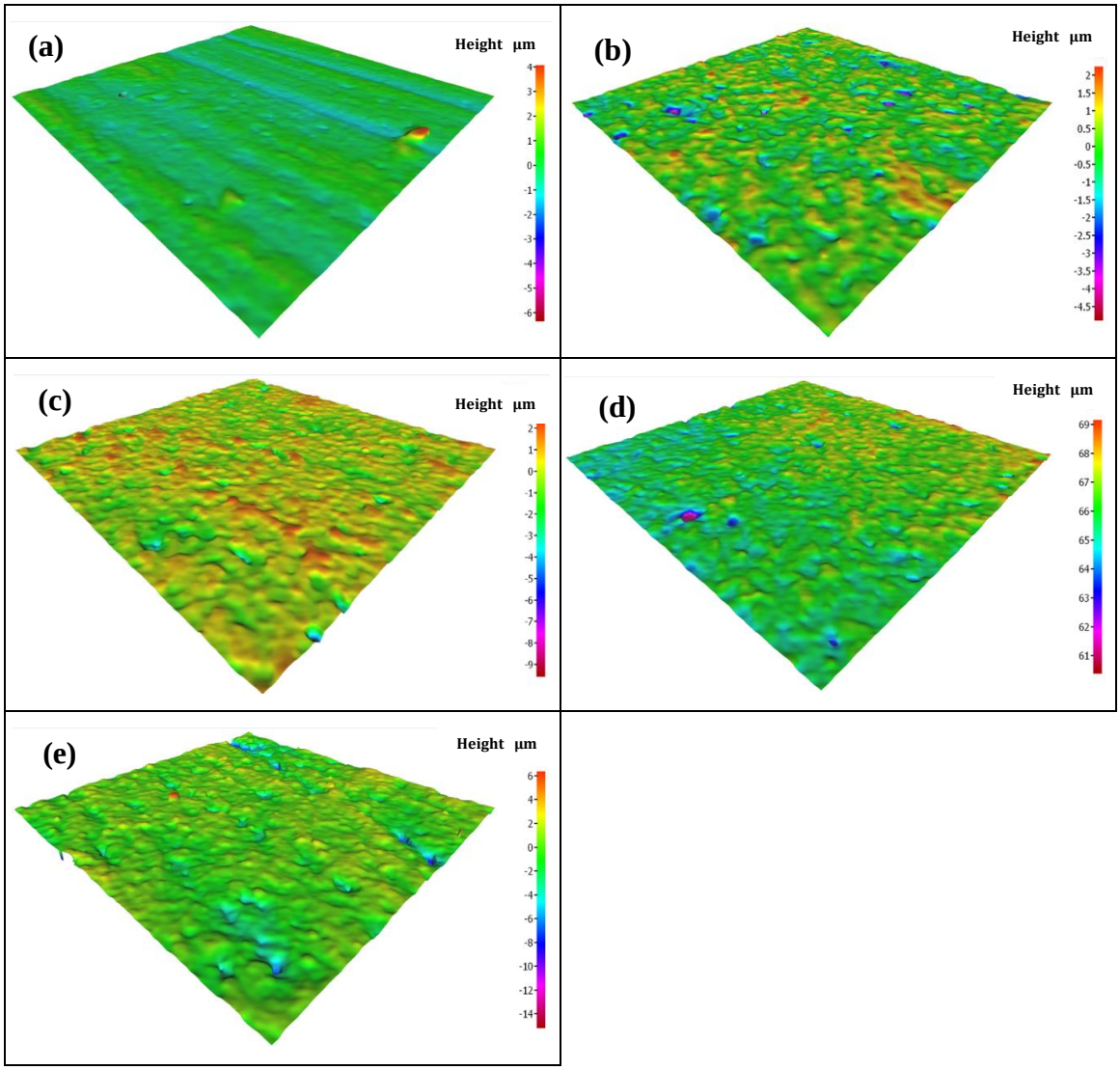

Figure 41: Three-dimensional trace maps of surface roughness (180x180 µm^2) for bone samples ablated at 30 J/cm^2 and various repetition rates. (a) Untreated surface, (b) 100 kHz, (c) 200 kHz, (d) 400 kHz, and (e) 600 kHz.

7.1.3.4 Energy dispersive X-ray spectroscopy analysis

In orthopedics and dentistry, it is important to preserve the chemical properties of treated tissue. Human bones and teeth have trouble self-organizing (regrowing) when the chemical properties of hydroxyapatite ($Ca_{10}(PO_4)_6(OH)_2$) are changed [198, 199]. Hydroxyapatite crystals are made of calcium (Ca) and phosphorus (P), both inorganic

substances. The crystals are oriented along collagen made of two organic elements: carbon (C) and oxygen (O). This study aimed to investigate how ablation affects the chemical properties of hard tissue. The concentrations of these elements were measured as a percentage of the sample's total weight using an energy dispersed X-ray microanalysis system (EDX). Ca and P ratios (weight %), which indicate bone quality [200], were then calculated for each sample. This study used the cavities shown in Fig. 40. The untreated parts of the same samples were used as a control. Three distinct sites were measured in each cavity, and the results were expressed as a mean ± standard deviation.

The results of the analyses are recorded in Table 8, and EDX spectra are shown in Fig. 42. At 100-600 kHz, there was 60% less C than in untreated areas, measured by weight. At 800 kHz, there was 80% less C, suggesting a decrease in organic composites [8]. No significant changes in O were observed. Based on the EDX spectra, treated tissue had slightly more Ca and P, indicating some component changes on an atomic scale [201]. These changes were likely caused by increases in temperature. Because Ca and P increased, one would expect substituent changes in the tissue, but there were no significant differences in the Ca/P ratio between treated and untreated areas. Fiber lasers with high fluence and repetition rates might not affect the remaining tissue on a molecular level.

Girard et al. observed a similar Ca/P ratio before and after treatment using a Ti:Sapphire laser, but they reported increased O, likely because the recoil material in the ablated area contains free radicals, which react with oxygen molecules in air [8]. In contrast to the present work, several studies reported changes to inorganic (Ca and P) ratios post-

ablation [109, 202]. Junbiao et al. observed changes in the Ca/P ratio in tissue ablated using an ultrashort pulse-free electron laser (wavelength 9.6 μm, pulse duration 2 ps) [202]. Sasaki et al. noted a decrease in the Ca/P ratio of ablated bone after Er:YAG irradiation [109]. This change in the Ca/P ratio could be explained by increased temperatures, which cause the formation of new products, such as alpha and beta-tricalcium phosphates $Ca_3(PO_4)_2$, as well as pyrophosphate ($Ca_2P_2O_7$) [203, 204].

Table 8: Atomic analyses of bone samples treated at 30 J/cm^2 and various repetition rates.

Samples	Content (weight %)				
	C	O	Ca	P	Ca/P
	Mean ± SD	Mean ± SD	Mean ± SD	Mean ± SD	Mean ± SD
Control sample	17.9 ± 0.5	31.0 ± 0.8	25.9 ± 1.0	11.8 ± 0.2	2.1 ± 0.1
Treated at 100 kHz	7.2 ± 1.8	30.7 ± 2.4	33.4 ± 0.9	15.6 ± 0.8	2.1 ± 0.1
Treated at 200 kHz	7.5 ± 1.7	31.7 ± 1.2	32.8 ± 2.6	15.0 ± 1.3	2.1 ± 0.1
Treated at 400 kHz	7.6 ± 0.7	32.6 ± 1.8	33.1 ± 1.8	14.6 ± 1.5	2.2 ± 0.2
Treated at 600 kHz	6.9 ± 1.6	29.8 ± 1.6	38.5 ± 4.1	16.3 ± 1.3	2.3 ± 0.3
Treated at 800 kHz	3.8 ± 0.5	34.1 ± 3.0	34.0 ± 2.6	16.1 ± 0.9	2.1 ± 0.1

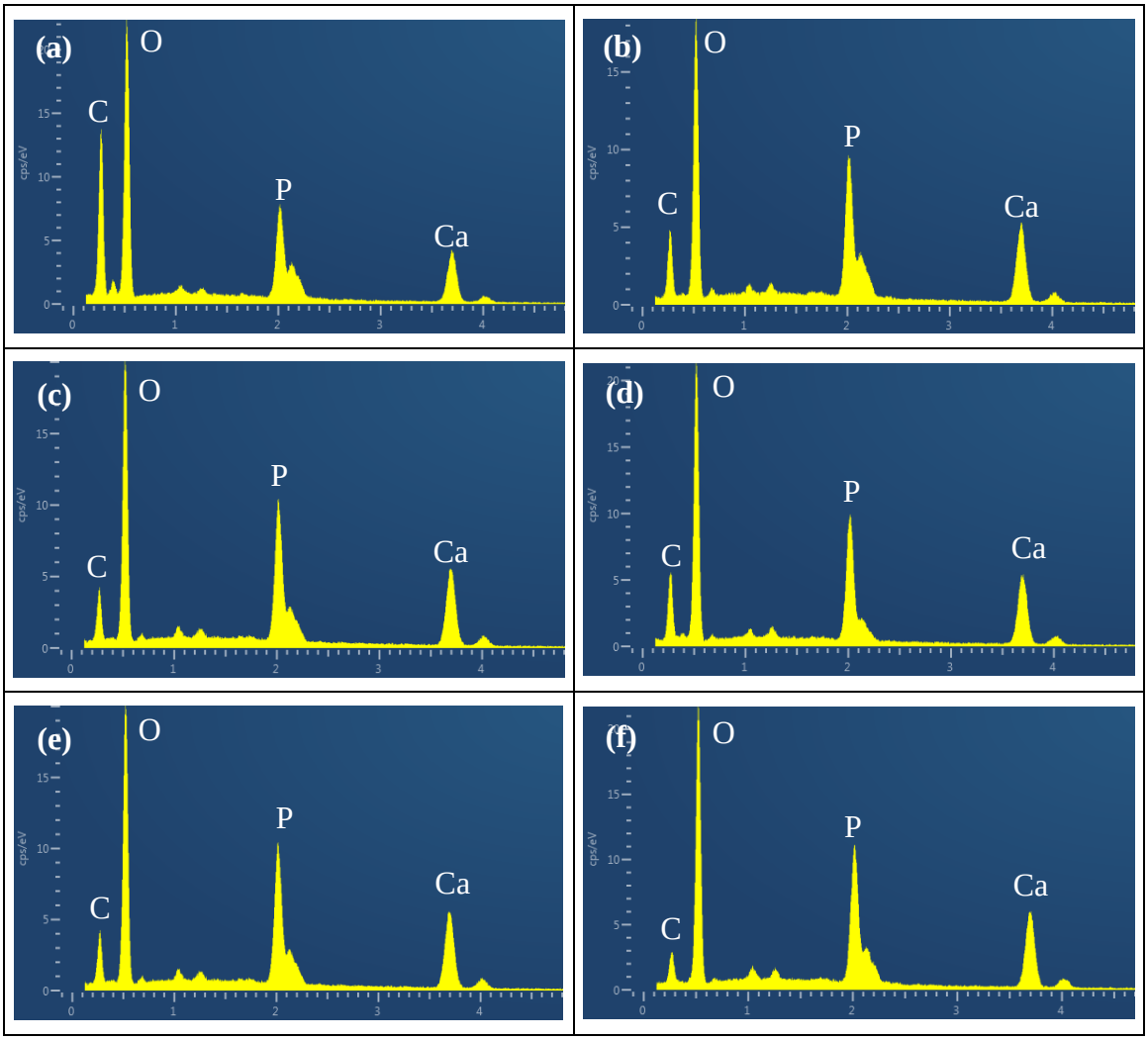

Figure 42: EDX spectra of bone samples ablated using 30 J/cm^2 and various repetition rates: (a) untreated, (b) 100 kHz, (c) 200 kHz, (d) 400 kHz, (e) 600 kHz, and (f) 800 kHz.

7.1.3.5 Micro-Raman analysis

High repetition rates can cause severe thermal effects, changing the mineral and organic components of hard tissue and forming amorphous carbon [126, 128]. This study investigated the effects of high repetition rates on ablated tissue to ensure the irradiation process did not cause thermal damage. Cavities ablated in hard tissue at 30 J/cm^2 and various repetition rates shown in Fig. 40 were analyzed using Raman spectroscopy, the

results of which are shown in Fig. 43. A Raman spectrometer (inVia Qontor confocal Raman microscope, Renishaw) equipped with a helium-neon gas laser (model 127, Spectra Physics) operating at 633 nm provided the Raman spectra.

Raman spectra were recorded for treated and untreated samples, with an acquisition time of 30 seconds and 5 accumulations over a wavenumber range of 400-3200 cm^{-1}. High background levels were recorded in all spectra due to the samples' rough surfaces, which can cause background light scattering.

In every sample ablated at 100-600 kHz and untreated, the Raman bands were clearly linked to specific components of hard tissue. Inorganic components are connected to the ν_1 vibration of the phosphate (PO_4^{3-}) internal mode at 960 cm^{-1} [205]. The other markers of the mineral elements are detected at 430 and 591 cm^{-1} correspond to the characteristic ν_2 and ν_4 vibrations of the phosphate (PO_4^{3-}) groups in hydroxyapatite [52]. Bands were observed at 1070 cm^{-1} for B-type carbonates (CO_3^{2-}), which substitute components of apatite [52]. The bending vibration bands of phosphate (HPO_4^{2-}) ions were observed at 1453 cm^{-1} [205]. Small peak intensities between 1035 and 1048 cm^{-1} correspond with ν_3 phosphate vibrations (PO_4^{3-}), which overlap with carbonate (CO_3^{2-}), making them hard to see.

In every sample treated at 100-600 kHz and untreated, the major bands were also assigned to organic components. The amide bands of proteins were detected at 1250 cm^{-1} (amide III) and 1678 cm^{-1} (amide I) [206]. The carbon-hydrogen (C-H) modes present in

collagenous and noncollagenous components were visible at 2877, 2930, and 3000 cm^{-1} [205]. According to the data in Fig. 43, no new phases were formed between 100 and 600 kHz, meaning the tissue did not overheat. The spectra of the untreated samples were more intense than those of the treated samples, likely caused by differences in surface roughness [207].

Raman spectra could not be obtained from samples treated at 800 kHz due to fluorescence emissions from the carbonized layer [127]. Spectra were instead recorded from tissue surrounding the cavity. The spectra peak at 430, 591, and 961 cm^{-1}, corresponding to the v_2, v_4, and v_1 vibrations characteristic of the phosphate (PO_4^{3-}) groups in hydroxyapatite. There were no peaks observed for organic components, suggesting the analyzed area lost almost all of its organic material. There were two peaks at 1350 (D-band) and 1580 (G-band) cm^{-1}, reflecting the high levels of amorphous carbon which confirm the transfer of the generated heat to the HAZ (heat affected zone) during the ablation process [208].

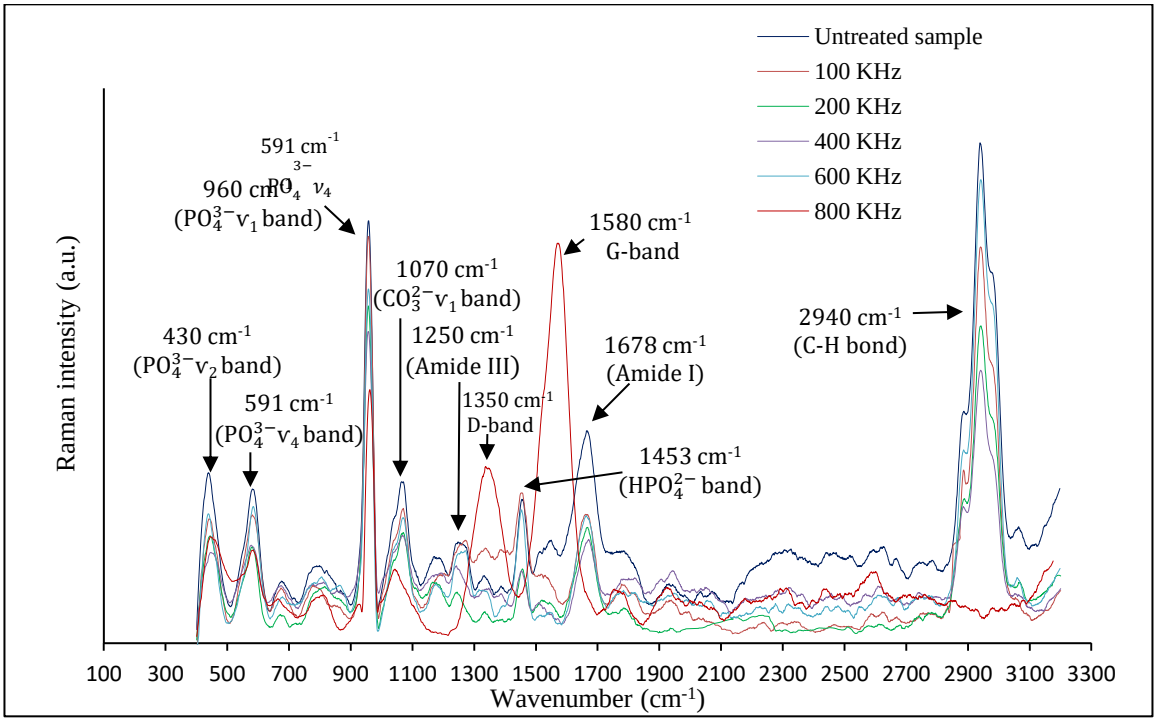

Figure 43: Raman spectra of samples treated at 100-800 kHz, as well as untreated samples. The ablation was carried out using a fiber laser (wavelength 1035 nm, pulse duration 1 ps, fluence 30 J/cm^2).

7.2 Cavity preparation under water condition

7.2.1 Introduction

Ultrashort pulse laser ablation causes minimal thermal damage, but a high enough repetition rate can negate this advantage, as shown in Section 7.1. A water cooling system could reduce the collateral damage caused by high repetition rates. Several studies show that a layer of water on the tissue surface can prevent thermal damage to adjacent tissue [100, 209], although some researchers observed tissue heating and thermal effects despite water cooling [98, 122]. The effect of water on ablation efficiency is also unclear. Water cooling has been reported to increase ablation efficiency, as it removes debris from the ablation area, preventing debris shielding [158, 210]. In others studies, the water absorbed a portion of the beam's energy, reducing the ablation rate [122, 211].

This section investigates the effect of water cooling on ablation in several ways. The first study focused on the relationship between ablation rate (mm^3/s), repetition rate, and fluence. In the second investigation, ablation quality was characterized using SEM images. Surface roughness was measured in the third study. The fourth and fifth investigations used EDX and Raman analyses to see if the ablation process changed the chemical composition of the removal area. The findings of each experiment were compared to the findings of dry condition (Section 7.1).

7.2.2 Method

The method is nearly identical to that of Section 7.1.2. The only difference is the use of a layer of water (500 µm thick) on the sample surface during the removal process with fluences ranging from 10 to 30 J/cm^2.

7.2.3 Results and discussion

7.2.3.1 Ablation rate

Fig. 44 illustrates the effect of fluence and repetition rate on ablation rate under wet conditions. At all repetition rates, the ablation rate increased with fluence. For example, at 600 kHz, the ablation rate increased from $0.25x10^{-4}$ to $0.29x10^{-4}$ mm^3/s as fluence increased from 10 to 30 J/cm^2. The effect of repetition rate on ablation rate is also clear. At 10 J/cm^2, the ablation rate was 6 times greater at 800 kHz than at 100 kHz. Similar effects were observed under dry conditions (Fig. 39). However, at 800 kHz, wet ablation produced regularly shaped cavities with measurable ablation rates, a departure from the irregular cavities of Section 7.1.3.1. Wet ablation resulted in lower ablation rates than dry ablation

at the same repetition rate and fluence. For example, at 400 kHz and 10 J/cm^2, the dry ablation rate was 0.37x10^{-4} mm^3/s (Fig. 39), while the wet ablation rate was 0.20x10^{-4} mm^3/s (Fig. 44), a 45% reduction.

These findings may have been caused by interactions between the ultrashort pulse laser and the water layer. Such interactions can involve optical breakdown, leading to non-linear phenomena, such as plasma generation, which attenuate the laser beam before it reaches its target. It has been reported that plasma shielding within the water layer can result in an energy loss of 30-70% [163, 81]. These interactions can also form cavitation bubbles that scatter the incoming laser beam [212].

Water cooling has been shown to reduce the ablation rate of ultrashort pulse lasers. Cangueiro and Vilar reported a 50% drop in the ablation rate when using a Yb:KYW laser setup (1030 nm, 500 fs, and 3 kHz) under wet conditions [127]. They used repetition rates of 40-1000 Hz and a fluence of 2 J/cm^2. Silva et al. observed an even higher decrease (70%) under wet conditions using a high-power Nd:YVO_4 laser (1064 nm, 10 ps, and 100 kHz) at fluences ranging from 4 to 8 J/cm^2 [122].

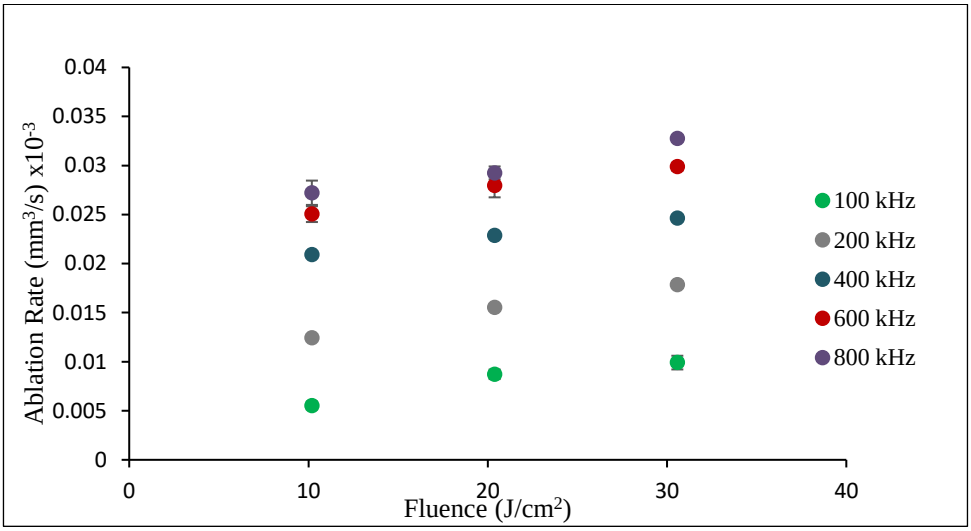

Figure 44: Ablation rate as a function of laser fluence at various repetition rates under water layer using a fiber laser (wavelength 1035 nm, pulse duration 1 ps).

7.2.3.2 Ablation quality

This study used SEM to characterize the ablation quality of bovine bone samples, which were ablated with a fluence of 30 J/cm^2 and repetition rates of 100-800 kHz under a water layer. Fig. 45 shows top-down views of each cavity. At all repetition rates examined, the cavities are well-defined, with no visible microcracks except for one large crack at 800 kHz (Fig. 45e). This crack probably formed during the dehydration process required for taking SEM images, which also created cracks in untreated areas. Unlike the rough crater edges observed when using Ti:Sapphire laser (Fig. 29c and d), fiber laser ablation produced cavities with smooth rims (Fig. 45), indicating minimal pressure at the beginning and collapsing of bubbles, which can mechanically affect the removal of tissue from cavity edges [169, 170].

No visible discoloration, carbonization, or other indicators of thermal damage were observed at any repetition rate under wet conditions. This is especially noteworthy at 800

kHz; under dry conditions, 800 kHz produced severe carbonization (Fig. 40e) due to excessive heat accumulation. Kang el at. found similar results using a long-pulsed Er,Cr:YSGG laser (wavelength of 2.79 μm, pulse duration of 150 μs, and pulse rate of 10 kHz) [211]. They observed irregular surface deformation and black carbonization surrounded by a white recrystallization rim under dry ablation, but when they used a layer of water, they did not find any carbonization.

Although water layer eliminates thermal damage, it drastically reduces the ablation rate (7.2.3.1), making it impractical for dental and orthopedic surgery. However, when used with microsecond pulse lasers, water cooling reportedly increases ablation rate [122, 213]. This is likely caused by a thermomechanical process associated with water ablation, where incoming laser energy is absorbed by water and transformed into heat, evaporating the water and causing micro-explosions in the irradiated tissue.

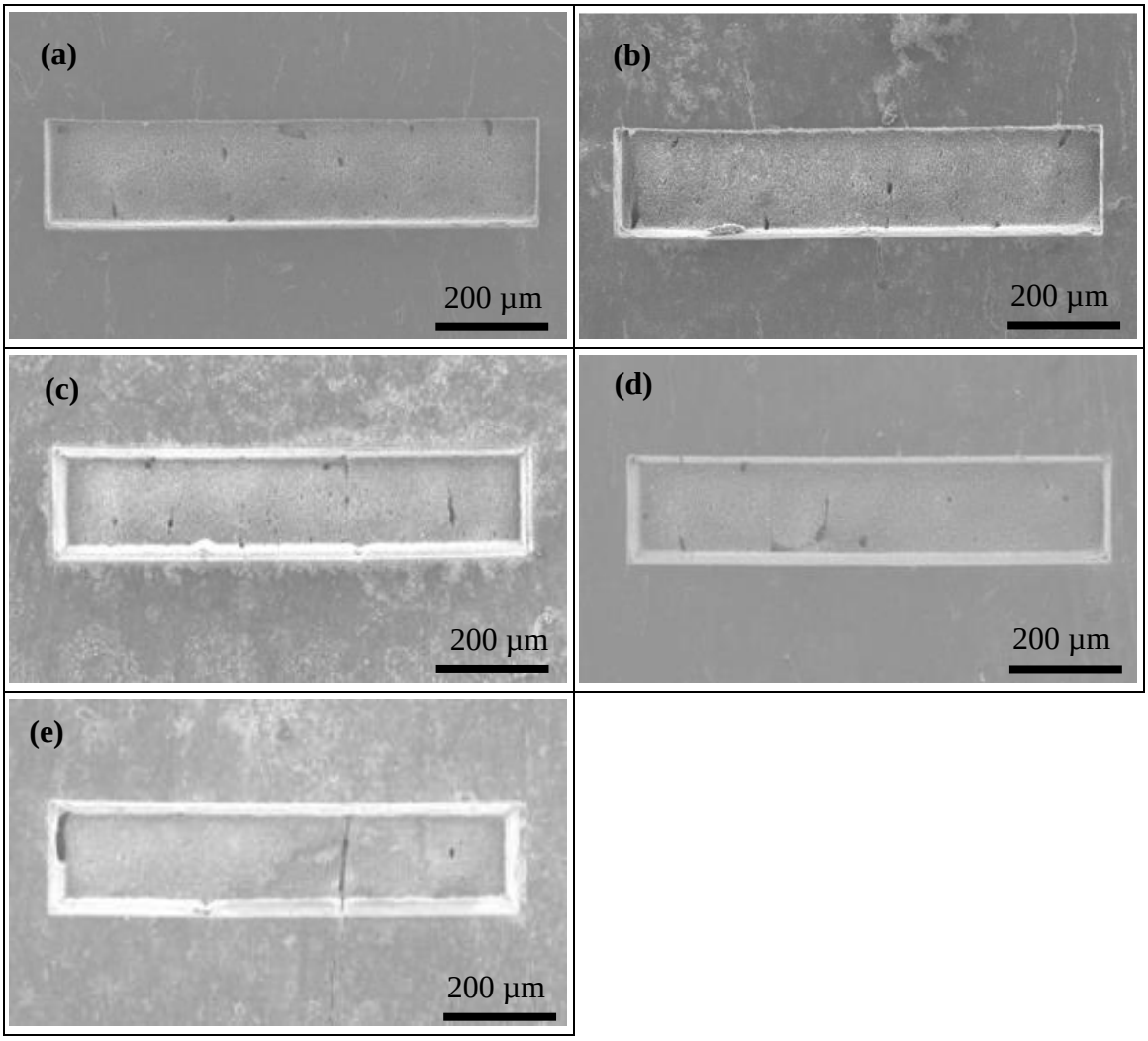

Figure 45: Top-down SEM images of cavities in bovine bone. The cavities were created by scanning a 1000x200 (μm^2) rectangular pattern 30 times at (a) 100 kHz, (b) 200 kHz, (c) 400 kHz, (d) 600 kHz, and (e) 800 kHz, with a fluence of 30 J/cm^2 and a scanning speed of 2000 µm/s.

7.2.3.3 Surface roughness

Table 9 shows the roughness of cavities ablated at 30 J/cm^2 and 100-800 kHz under wet conditions, with three measurements per repetition rate. Fig. 46 shows three-dimensional trace maps of each sample's surface. Mean roughness values are recorded in Table 9. The control sample's Ra and Rz were measured to be 0.29 ± 0.04 and 0.93 ± 0.13 µm respectively. The treated samples were far rougher, similar to the results of dry

condition (Section 7.1.3.3). At 100 kHz, Ra and Rz equaled 0.42 ± 0.02 and 1.93 ± 0.15 µm respectively. Similar values were obtained at 200 kHz, where Ra was 0.45 ± 0.03 µm and Rz was 2.02 ± 0.05 µm. The greatest Ra was achieved at 800 kHz, 0.67 ± 0.01 µm, while the greatest Rz equaled 2.50 ± 0.08 µm and was obtained at 600 kHz. The findings recorded in Table 7 (dry conditions) and Table 9 (wet conditions) indicate that ablation condition does not significantly affect surface roughness. For example, at 100 kHz, wet ablation produced an Ra of 0.42 ± 0.2 µm and an Rz of 1.93 ± 0.15 µm, while dry ablation produced an Ra of 0.44 ± 0.03 µm and an Rz values of 1.90 ± 0.11 µm.

The results of this study suggest that water cooling has little effect on the relationship between repetition rate and surface roughness. However, Cangueiro and Vilar obtained very different results using a Yb:KYW laser system (wavelength of 1030 nm and pulse duration of 500 fs) at repetition rates between 50 Hz and 3 kHz [127]. In their study, dry ablation resulted in a smooth cavity bottom at frequencies up to 1 kHz; higher frequencies produced irregular surfaces with large cracks. Under wet conditions, the ablated surface was completely flat at frequencies below 1 kHz. At higher frequencies, the surface became rougher, but it never became as rough as the cavities produced by dry ablation.

Table 9: Mean surface roughness of bone treated using 30 J/cm^2 at various repetition rates under water condition.

Samples	Surface roughness	
	Ra (µm) Mean ± SD	Rz (µm) Mean ± SD
Control sample	0.29 ± 0.04	0.93 ± 0.13
Treated at 100 kHz	0.42 ± 0.02	1.93 ± 0.15
Treated at 200 kHz	0.45 ± 0.03	2.02 ± 0.05
Treated at 400 kHz	0.55 ± 0.03	1.89 ± 0.11
Treated at 600 kHz	0.62 ± 0.06	2.50 ± 0.08
Treated at 800 kHz	0.67 ± 0.01	2.31 ± 0.03

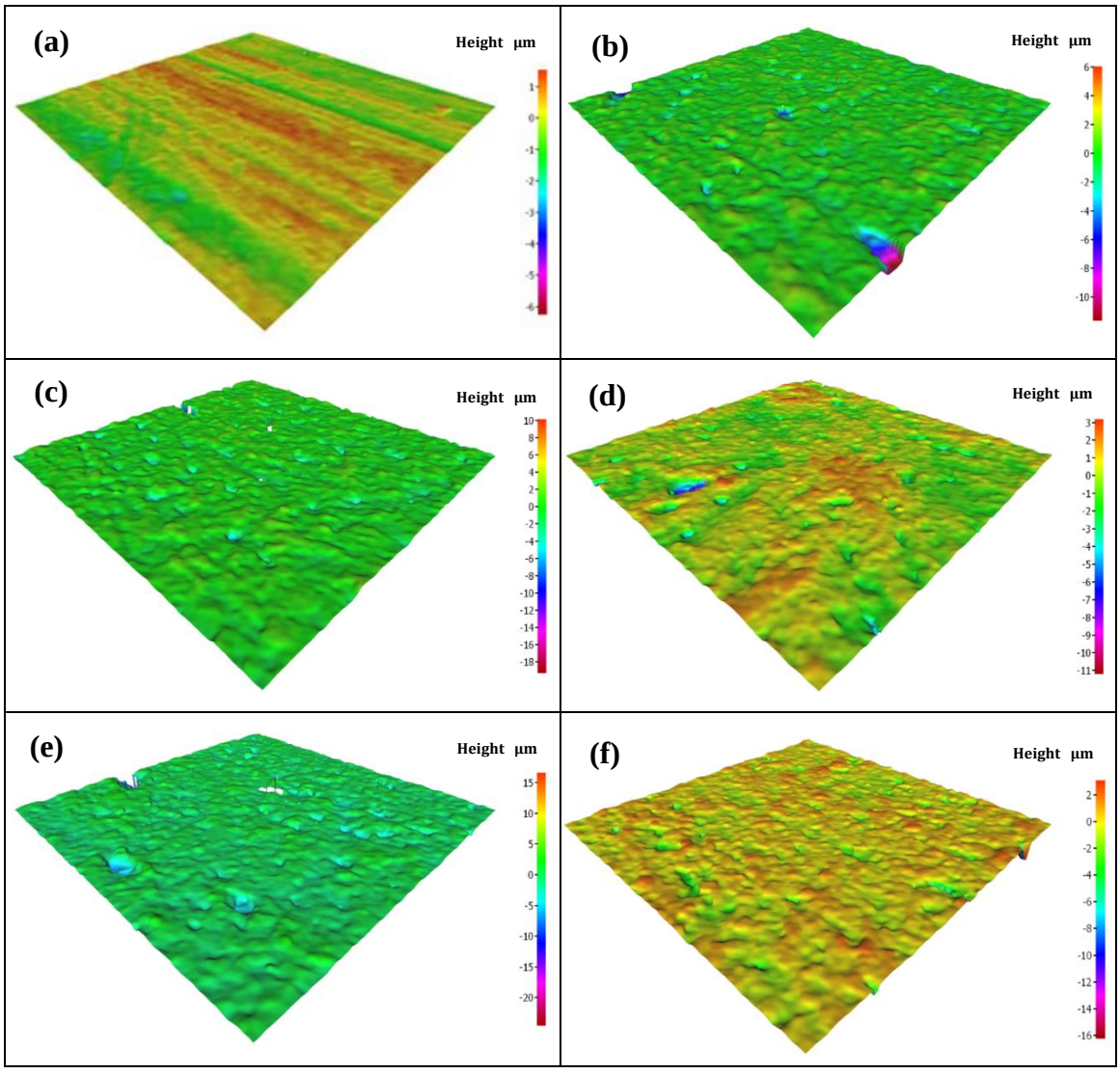

Figure 46: Three-dimensional trace maps of surface roughness (180x180 µm^2) for bone samples ablated at 30 J/cm^2 and various repetition rates under water condition. (a) Untreated surface, (b) 100 kHz, (c) 200 kHz, (d) 400 kHz, (e) 600 kHz, and (f) 800 kHz.

7.2.3.4 Energy dispersive X-ray spectroscopy analysis

The concentrations of C, O, P, and Ca in cavities ablated at 30 J/cm^2 and 100-800 kHz under a water layer were measured as a percentage of the sample's total weight. Ca/P ratios were also calculated for each sample. The results of the analyses are recorded in Table 10, and EDX spectra are shown in Fig. 47. At all repetition rates, no significant change in the concentration of organic elements, including carbon (C) and oxygen (O), was observed under wet conditions. For example, the weight of C was measured to be 17.8 ± 0.7 % for the control sample and 16.2 ± 0.5 % for the 600 kHz sample. Dry ablation increased the weight of calcium (Ca) and phosphorus (P) (Table 8), but wet ablation had no effect on the weights of these elements, nor did it change the Ca/P ratio of any sample. These results show that water cooling can protect bone from chemical changes.

Kimura et al. found similar results using a water spray and an Er,Cr:YSGG laser (wavelength of 2.78 μm, pulse duration of 200 μs, and repetition rate of 20 Hz) [201]. They reported no significant changes in the Ca/P weight ratio between unlased and lased areas. The Ca/P ratio equaled 2.19 ± 0.05 for untreated samples and 2.25 ± 0.03 % for irradiated samples. Under dry conditions, a decrease of Ca/P ratio after the Er:YAG laser irradiation was observed [214].

Table 10: Atomic analyses of bone samples treated at 30 J/cm^2 and various repetition rates under water condition.

Samples	Content (weight %)				
	C	O	Ca	P	Ca/P
	Mean ± SD	Mean ± SD	Mean ± SD	Mean ± SD	Mean ± SD
Control sample	17.8 ± 0.7	30.9 ± 0.7	25.5 ± 0.9	11.5 ± 0.4	2.2 ± 0.1
Treated at 100 kHz	15.8 ± 0.2	31.2 ± 1.0	25.7 ± 0.2	12.2 ± 0.4	2.1 ± 0.1
Treated at 200 kHz	15.2 ± 1.1	32.7 ± 2.5	28.1 ± 1.8	13.4 ± 0.8	2.1 ± 0.1
Treated at 400 kHz	16.1 ± 0.9	31.0 ± 0.4	25.6 ± 0.4	12.0 ± 0.3	2.1 ± 0.1
Treated at 600 kHz	16.2 ± 0.5	31.2 ± 0.7	25.9 ± 0.7	12.6 ± 0.1	2.0 ± 0.1
Treated at 800 kHz	15.9 ± 0.4	30.3 ± 0.9	26.4 ± 0.7	12.6 ± 0.3	2.1 ± 0.1

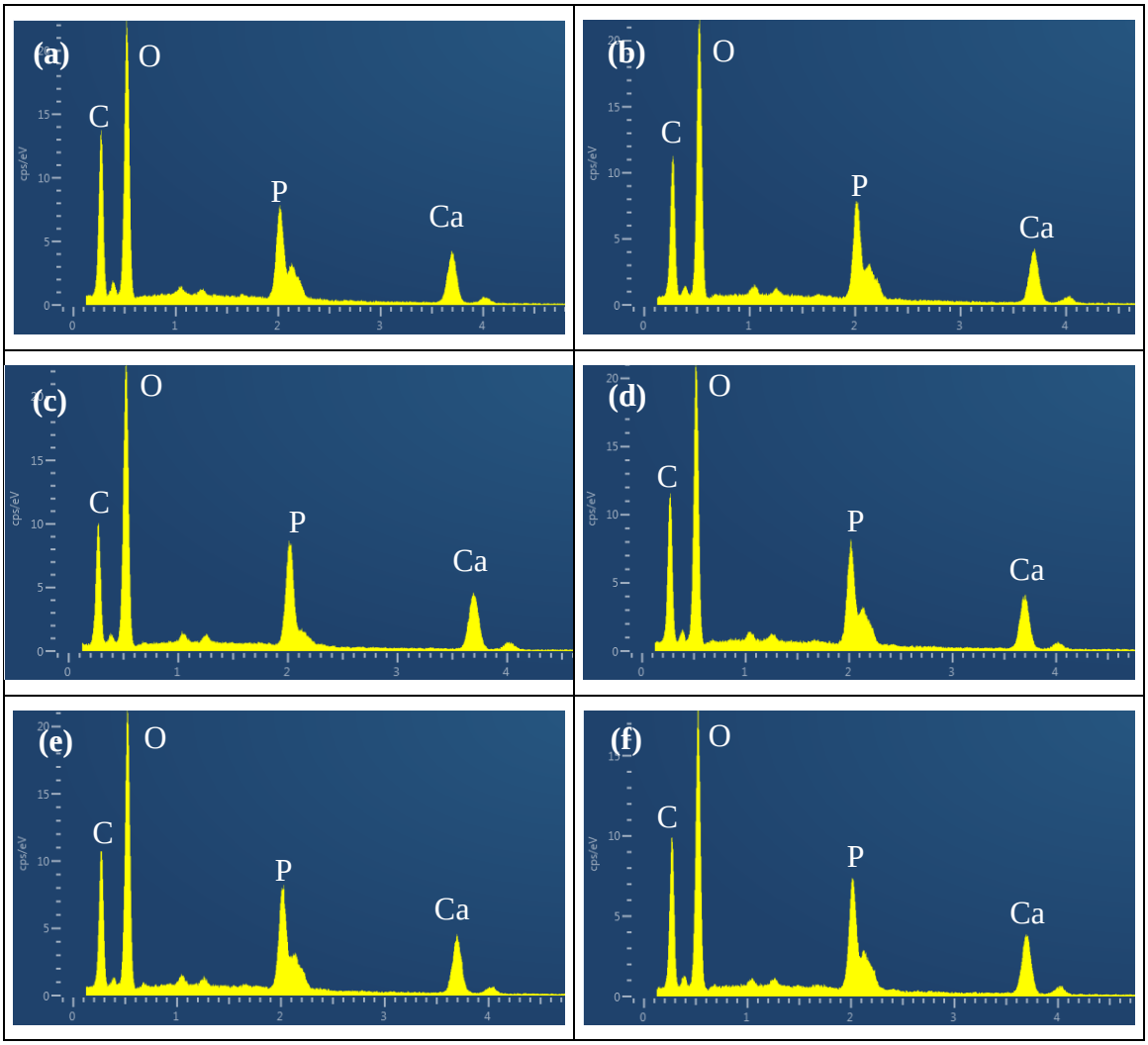

Figure 47: EDX spectra of bone samples ablated using 30 J/cm^2 and various repetition rates under water condition: (a) untreated, (b) 100 kHz, (c) 200 kHz, (d) 400 kHz, (e) 600 kHz, and (f) 800 kHz.

7.2.3.5 Micro-Raman analysis

Cavities ablated in cortical bone at 30 J/cm^2 and various repetition rates (100-800 kHz) were analyzed using Raman spectroscopy, the results of which are shown in Fig. 48. At all repetition rates, all the Raman bands were clearly associated with specific components. The inorganic part of the spectra is dominated by the ν_1 vibration of the phosphate (PO_4^{3-}) internal mode at 960 cm^{-1} [205]. Other markers of mineral elements were detected at 430, 591, 1070, and 1453 cm^{-1}, corresponding with the characteristic ν_2 and ν_4 vibrations of phosphate (PO_4^{3-}), B-type carbonate band (CO_3^{2-}), and bending vibration band of phosphate ions (HPO_4^{2-}) respectively [52, 205]. As for the organic components, the amide bands of proteins were detected at 1250 cm^{-1} (amide III) and 1678 cm^{-1} (amide I) [206]. The carbon-hydrogen (C-H) modes present in collagenous and noncollagenous components is visible at 2940 cm^{-1} [205]. The effect of water on the components of the ablated area can be seen at 800 kHz. Under dry conditions, there were two peaks at 1350 cm^{-1} (D-band) and 1580 cm^{-1} (G-band), corresponding to amorphous carbon, as shown Fig. 43 (grey curve). These peaks were not observed under wet conditions (Fig. 48, grey curve), confirming a lack of excessive heat accumulation.

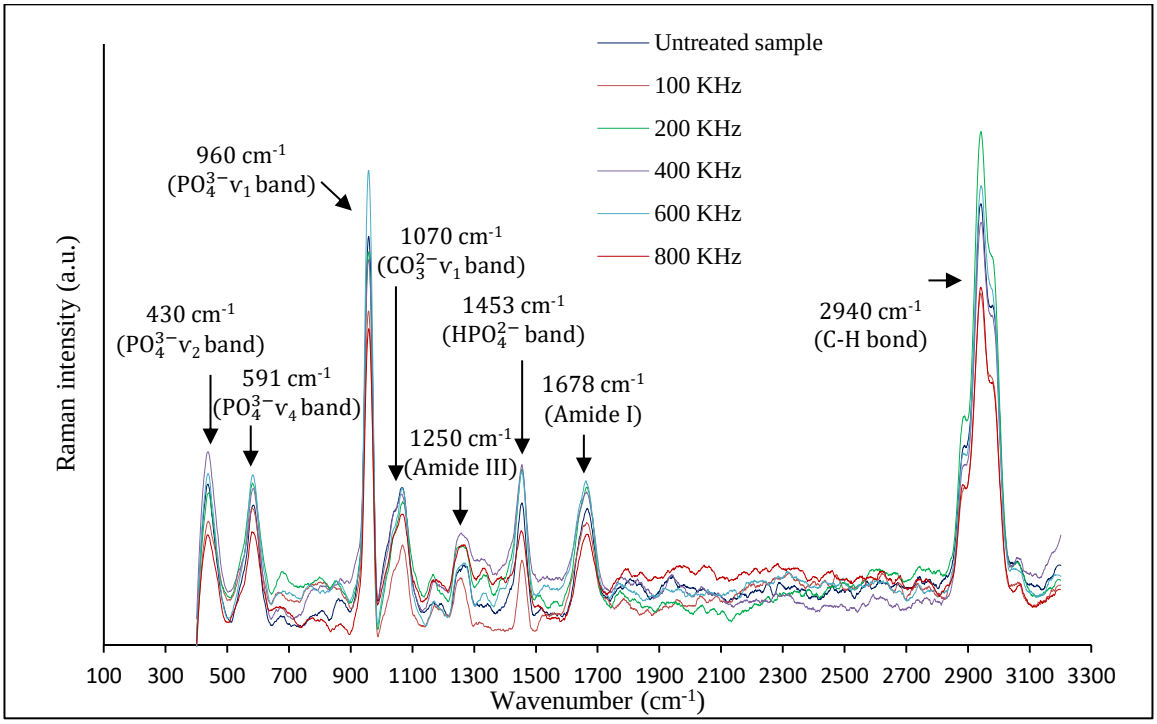

Figure 48: Raman spectra of samples treated at 100-800 kHz under water layer, as well as untreated sample. Ablation experiment used a fiber laser (wavelength 1035 nm, pulse duration 1 ps, fluence 30 J/cm^2).

Chapter 8: Conclusion

8.1 Summary

Ultrashort lasers have the potential to replace mechanical tools in clinical applications where hard tissue ablation is needed, e.g. orthopedic and dental surgeries. One of the key advantages in ultrafast laser ablation of hard tissue is non-thermal based ablation process that allow precise removal of a small volume of tissue through a non-contact process.

Ultrashort laser-tissue interactions have been an active area of research since amplification of ultrashort laser pulses were developed in the late 1980s [215]. This thesis first provided a brief overview of the histology and optical properties of bone, which play a significant role in laser-tissue interactions. A literature review was then conducted to learn how different types of lasers affect the ablation process. It is shown that hard tissue ablation using long pulse lasers (> 10 ps) is often accompanied by collateral damage, thermal or mechanical, which limits the ability for precision ablation. Even with improvements using cooling-assisted methods, thermal side effects causing chemical changes in the tissue were still observed. In contrast, more precise ablation with little or no collateral damage and low ablation efficiency have been reported when ultrashort pulsed lasers were used. Nevertheless, before ultrashort laser ablation can become a clinical reality, a number of issues need to be addressed.

The goal of this study was to study methods to improve ablation efficiency, producing deep structures, while minimizing collateral damage. An amplified Ti: Sapphire

(210 fs, 800 nm, 1 kHz) laser and a fiber laser (1 ps, 1035 nm, 100 kHz - 1 MHz) are used with a motorized laser micromachining setup with bovine cortical bone samples. A first step towards optimization of the ablation efficiency was to determine the most appropriate laser and processing parameters. We investigated the relationship between ablation rate and certain laser parameters, including fluence, repetition rate, scanning speed, and number of successive passes. The results concluded that a low scanning speed and high fluence, repetition rate, and number of successive passes increased the ablation depth in bovine cortical bone.

During large-scale ablation, ablation debris can reduce ablation rate. There are also concerns that high fluence (~10 F_{th}) may also lead to thermal damages to the crater surface. Consequently, the second step was to find the best experimental conditions for achieving high removal efficiency and producing deep structures with minimal collateral damage. Assistive methods such as water or compressed air flow during ablation were studied. We used a Ti:Sapphire laser (210 fs, 800 nm, 1 kHz) at a fluence of 15 J/cm^2 (~10 F_{th}) and scanning speed of 200 µm/s to study the effects of air and water cooling systems on ablation depth, rate, tissue surface morphology, and thermal effects. Under air flow, the results showed an increase in deeper cavities and higher ablation rates than those of water or only air due to removing ablation debris. Water reduced the energy of the beam through plasma shielding and other effects like beam distortion, leading to shallow cavities and low ablation rates. The smoothest inner wall surface was produced with air flow which can be a result of the clean ablation process. In both underwater cases, the inner wall surface of the cavity was rougher presumably due to the hydrodynamic motion of cavitation bubbles

in water. Despite the laser's high fluence and low scanning speed, we observed no thermal damage in any experimental conditions.

Orthopedic surgeons need to ablate large amounts of tissue in a limited time. In other words, they need high ablation efficiency. One of ways to increase ablation efficiency is to use an ultrashort laser with a high repetition rate. The Ti: Sapphire laser has a limited repetition rate at 1 kHz, we explored the application of high-rate fiber laser (1 ps, 1035 nm, 100 kHz - 1 MHz) in hard tissue ablation. The effect of fluence and pulse rate on ablation process including ablation rate, quality, and thermal effects was investigated as the third step. Our findings showed that ablation efficiency increased with fluence and pulse rate, but when the repetition rate exceeded 600 kHz, it caused severe thermal damage, microcracks, and chemical changes in the properties of the sample, indicated by amorphous carbon in adjacent tissue. Pulse rate had no significant effect on surface roughness. The ablation rate was also far lower under wet conditions than dry conditions.

Our collective conclusion to this project is that a significant improvement of laser ablation efficiency with precise tissue cut and minimal or no thermal and mechanical damage can be carried out using ultrashort pulsed laser at high fluence (~10 F_{th}) and repetition rate (few hundreds kHz). At higher pulse rate and to avoid collateral damage of the surrounding tissue, low pulse overlap should be applied by e.g. increasing scanning speed. Furthermore, the experimental condition of hard tissue removal has a high influence on laser ablation process. Using air flow to remove the ablation debris from the cavity during removal process can enhance the ablation efficiency.

8.2 Future experiments

In this project, there are still some important points that can be studied to enhance laser ablation efficiency. First, the material properties of bone affect the ablation process. One material can have several different ablation thresholds for the same laser, depending on the structure of the material. To prevent damage to surrounding tissue, the ablation threshold needs to be as low as possible during orthopedic and dental procedures. Researchers have tried to decrease the ablation thresholds of several materials, but more investigation is needed to understand how material properties such as surface roughness affect ablation thresholds. Second, the energy accumulation effect of multi-pulse ablation on the removal process is also unclear, especially at high repetition rates (>100 kHz) and needs more research. Third, the present study managed to improve ablation efficiency by removing debris from the ablation area with air flow-assisted method. At high aspect ratio (depth/width > 3) and under air flow, some ablation debris accumulated at the bottom of the cavity causing reduction in the removal efficiency was observed. Several air flushing strategies such as setting the air flow angle to be more perpendicular (> 45^{o}) to the tissue surface can be investigated to achieve high ablation efficiency at high aspect ratio. Fourth, regarding severe collateral damage of surrounding tissue resulted from high repetition rate pulse ablation (> 600 kHz), more investigation of cooling systems can be carried out to minimize the damage. For example, the water layer and air jet can be used simultaneously where water limits the tissue temperature increment and is diverted from the ablation area by an air jet, allowing the beam to pass without obstruction. Fifth, higher repetition rate (800 kHz) shows high increasement in tissue temperature, affecting on ablation quality. So,

it is imperative to know the tissue temperature during the ablation process. A numerical model for the heating and heat distribution in tissue under different repetition rate can be made to study the effect of temperature on ablation quality.

Besides enhancement of laser ablation efficiency, some points regarding the laser setup can be improved for gaining clinical relevance. First, given the advances in terms of compact and efficient solid state laser technologies, one might think of a hybrid system, where an ultrafast laser and a longer pulse laser, could be on board with suitable laser parameters such as repetition rate and wavelength, which could be used for the larger material removal rate operations. Second, ultrashort pulse lasers could be also integrated with real-time feedback control systems, making them more precise and less harmful to surrounding tissue. Several real-time feedback control methods could be used, including Laser Induced Breakdown Spectroscopy (LIBS), which can rapidly analyze the ablated area. Other additions, such as a robotic delivery arm, could make laser technology a viable replacement for mechanical tools. The design and construction of these additions are complex, multidisciplinary challenges, but their implementation could make orthopedic and dental procedures safer and more effective.

References

[1] H. Lal, D. Sharma, and D. Mittal, "Intrapelvic migration of hip lag screw of proximal femoral nail-sequele to a paradoxical reverse Z effect and their critical analysis," Journal of Clinical Orthopaedics and Trauma 3, 48 (2012).

[2] A. Nayak, S. Gutierrez, J. Billys, B. Santoni, and A. Castellvi, "Biomechanics of lateral plate and pedicle screw constructs in lumbar spines instrumented at two levels with laterally placed interbody cages," Spine J 13, 1331 (2013).

[3] E. Siebert, "History of lasers in orthopedic medicine," Springer Berlin Heidelberg, ISBN: 978-3-642-56420-8, (2001).

[4] L. Rybak, A. Gangi, X. Buy, R. Rocca, and J. Wittig, "Thermal ablation of spinal osteoid osteomas close to neural elements: technical considerations," AJR Am. J. Roentgenol 195, 293 (2010).

[5] F. Hardeman, H. Vandenneucker, J. Lauwe, and J. Bellemans, "Cementless total knee arthroplasty with profix: A 8- to 10-year follow-up study," The Knee 13, 419 (2006).

[6] M. Davarpanah, and S. Moncler, "Unconventional implant treatment: I. implant placement in contact with ankylosed root fragments. A series of five case reports," Clinical Oral Implants Research 20, 851 (2009).

[7] W. Ward, J. Eckardt, S. Shayestehfar, J. Mirra, T. Grogan, and W. Oppenheim, "Osteoid osteoma diagnosis and management with low morbidity," Clin Orthop Relat Res 291, 229 (1993).

[8] B. Girard, D. Yu, M. Armstrong, B. Wilson, C. Clokie, and R. Miller, "Effects of femtosecond laser irradiation on osseous tissues," Laser Surg Med 39, 273 (2007).

[9] S. Rath, S. Moszko, P. Schaffner, G. Cantone, V. Braun, H. Richter, and G. Antoniadis, "Accuracy of pedicle screw insertion in the cervical spine for internal fixation using frameless stereotactic guidance," J Neurosurg Spine 8, 237 (2008).

[10] K. Firoozbakhsh, M. Moneim, E. Mikola, and S. Haltom, "Heat generation during ulnar osteotomy with microsagittal saw blades," Iowo Orthop J 23, 46 (2003).

[11] S. Sevitt, "Early and delayed oedema and increase in capillary permeability after burns of the skin," J Pathol Bacteriol 75, 27 (1958).

[12] C. Scholz and M. Grothves-Spork, "Angewandte laseredizin IIII," Ecomed, Landsberg, Lech, (1992).

[13] S. Stübinger, "Advances in bone surgery: the Er:YAG laser in oral surgery and implant dentistry," Clin Cosmet Investig Dent 2, 47 (2010).

[14] Y. Liu and M. Niemz, "Ablation of femural bone with femtosecond laser pulses - a feasibility study," Lasers Med Sci 22, 171 (2007).

[15] M. Stanislawki, J. Meister, T. Mitra, M. Ivanenko, K. Zanger, and P. Hering, "Hard tissue ablation with a free running Er:YAG and a Q-switched CO_2 laser: a comparative study," Appl Phys B 72, 1 (2000).

[16] R. Gruber, F. Kramer, H. Merten, and H. Schliephake, "Ultrasonic surgery - an alternative way in orthognathic surgery of the mandible a pilot study," Int J Oral Maxillofac Surg 34, 590 (2005).

[17] X. Zhang, Z. Zhan, H. Liu, H. Zhao, S. Xie, and Q. Ye, "Influence of water layer thickness on hard tissue ablation with pulsed CO_2 laser," J Biomed Opt 17, 038003 (2012).

[18] L. Goldman, R. Rockwell, Z. Naprstek, V. Siler, R. Hoefer, C. Hobeika, K. Hishimoto, T. Polanyi, and H. Bredmeier, "Some parameters of high output CO_2 laser experimental surgery," Nature 26, 1344 (1970).

[19] M. Papadaki, A. Doukas, W. Farinelli, L. Kaban, and M. Troulis, "Vertical ramus osteotomy with Er:YAG laser: a feasibility study," Int J Oral Maxillofac Surg 36, 1193 (2007).

[20] M. Staninec, N. Meshkin, S. Manesh, R. Ritchie, and D. Fried, "Weakening of dentin from cracks resulting from laser irradiation," Dent Mater. 25, 520 (2009).

[21] S. Backus, C. Durfee, M. Murnane, and H. Kapteyn, "High power ultrafast lasers," AIP, Review of Scientific Instruments 69, 1207 (1998).

[22] A. Oraevsky, L. Silva, A. Rubenchik, M. Feit, M. Glinsky, M. Perry, B. Mammini, W. Small, and B. Stuart, "Plasma mediated ablation of biological tissues with nanosecond-to-femtosecond laser pulses: relative role of linear and nonlinear absorption," IEEE Journal of Selected Topics in Quantum Electronics 2, 801 (1996).

[23] X. Liu, D. Du, and G. Mourou, "Laser ablation and micromachining with ultrashort laser pulses," IEEE Journal of Quantum Electronics 33, 1706 (1997).

[24] J. Neev, and J. Squier, "Preliminary characterization of hard dental tissue ablation with femtosecond lasers," International Society for Optics and Photonics,105 (1998).

[25] M. Freebody, "Fiber lasers at the cutting edge of surgery," BioPhotonics 20, (2013).

[26] S. Hall, "Basic biomechanics," 5th ed. London: McGraw-Hill. ISBN: 978-0-071-26041-1 (2007).

[27] Y. Barbara, O. Geraldine, and P. Woodford, "Wheater's functional histology: a text

and colour atlas," 5th ed. Elsevier Health Sciences. ISBN: 978-0-443-06850-8 (2006).

[28] J. Currey, "The mechanical adaptations of bones," Princeton University Press. ISBN: 978-0-691-08342-1 (1984).

[29] H. Gray, "Anatomy of the human body," 20th ed. Philadelphia: Lea & Febiger. ISBN: 1-58734-102-6 (1918).

[30] D. Newton, and M. Nunamaker, "Small animal orthopaedics," J. B. Lippincott & Co. ISBN: 978-0-397-52098-5 (1985).

[31] M. Pittenger, A. Mackay, S. Beck, R. Jaiswal, R. Douglas, J. Mosca, M. Moorman, D. Simonetti, S. Craig, and D. Marshak, "Multilineage potential of adult human mesenchymal stem cells," Science 284, 143 (1999).

[32] B. Noble, "The osteocyte lineage," Arch Biochem Biophys 473, 106 (2008).

[33] J. Rho, L. Kuhn, and P. Zioupos, "Mechanical properties and the hierarchical structure of bone," Med Eng Phys 20, 92 (1998).

[34] X. Feng, "Chemical and biochemical basis of cell-bone matrix interaction in health and disease," Curr Chem Biol 3, 189 (2009).

[35] M. Niemz, "Laser-tissue interactions: fundamentals and applications," Springer-Verlag Berlin and Heidelberg, GmbH & Co. ISBN: 978-3-540-72191-8 (1996).

[36] B. Ivanov, A. Hakimian, G. Peavy, and R. Haglund, "Mid-infrared laser ablation of a hard biocomposite material: mechanistic studies of pulse duration and interface effects," Applied Surface Science 208, 77 (2003).

[37] F. Morgan, L. Barnes, and A. Einhorn, "The bone organ system: form and function. in osteoporosis," 4th ed. San Diego: Academic Press, 26 (2008).

[38] A. Guyton, and J. Hall, "Textbook of medical physiology," 11th ed. Philadelphia: W. B. Saunders. ISBN: 978-0-721-60240-0 (2005).

[39] Y. Doi, T. Aoba, M. Okazaki, J. Takahashi, and Y. Moriwaki, "Analysis of paramagnetic centers in X-ray-irradiated enamel, bone, and carbonate-containing hydroxyapatite by electron spin resonance spectroscopy," Calcif Tissue Int 28, 107 (1979).

[40] R. Brommage, and W. Neuman, "Passive accumulation of magnesium, sodium, and potassium by chick calvaria," Calcif Tissue Int 28, 57 (1979).

[41] D. McConnell, D. Foreman, I. Drew, D. Perkins, and P. Daly, "Texture and composition of bone," Science 172, 971 (1971).

[42] N. Kourkoumelis, I. Balatsoukas, and M. Tzaphlidou, "Ca/P concentration ratio at different sites of normal and osteoporotic rabbit bones evaluated by Auger and energy dispersive X-ray spectroscopy" J Biol Phys 38, 279 (2012).

[43] M. Peacock, "Calcium metabolism in health and disease," Clin J Am Soc Nephrol 5 Suppl 1, S23–S30 (2010).

[44] R. Shapiro, and R. Heaney, "Co-dependence of calcium and phosphorus for growth and bone development under conditions of varying deficiency," Bone 32, 532 (2003).

[45] D. Baltimore, and H. Lodish, "Molecular cell biology," 4th ed. New York: W. H. Freeman, ISBN: 978-0-716-73706-3 (1999).

[46] M. Urist, A. Mikulski, and A. Lietze, "Solubilized and insolubilized bone morphogenetic protein," Proc Natl Acad Sci U.S.A. 76, 1828 (1979).

[47] K. Ishikawa, P. Ducheyne, and S. Radin, "Determination of the Ca/P ratio in calcium-deficient hydroxyapatite using X-ray diffraction analysis," J Mater Sci Mater Med 4, 165 (1993).

[48] F. Neues, and M. Epple, "X-ray microcomputer tomography for the study of biomineralized endo- and exoskeletons of animals," Chem Rev 108, 4734 (2008).

[49] P. Milovanovic, J. Potocnik, M. Stoiljkovic, D. Djonic, S. Nikolic, O. Neskovic, M. Djuric, and Z. Rakocevic, "Nanostructure and mineral composition of trabecular bone in the lateral femoral neck: Implications for bone fragility in elderly women," Acta Biomater 7, 3446 (2011).

[50] K. Akesson, M. Grynpas, R. Hancock, R. Odselius, and K. Obrant, "Energy-dispersive X-ray microanalysis of the bone mineral content in human trabecular bone: a comparison with ICPES and neutron activation analysis," Calcif Tissue Int 55, 236 (1994).

[51] J. Xu, P. Zhu, Z. Gan, N. Sahar, M. Tecklenburg, M. Morris, D. Kohn, and A. Ramamoorthy, "Natural-abundance Ca-43 solid-state NMR spectroscopy of bone," J Am Chem Soc 132, 11504 (2010).

[52] G. Penel, C. Delfosse, M. Descamps, and G. Leroy, "Composition of bone and apatitic biomaterials as revealed by intravital Raman microspectroscopy," Bone 36, 893 (2005).

[53] D. Bradley, M. Farquharson, O. Gundogdu, A. AlEbraheem, E. Ismail, W. Kaabar, O. Bunk, F. Pfeiffer, G. Falkenberge, and M. Bailey, "Applications of condensed matter understanding to medical tissues and disease progression: Elemental analysis and structural integrity of tissue scaffolds," Rad Phys Chem 79, 162 (2010).

[54] R. Hübler, E. Blando, L. Gaião, P. Kreisner, L. Post, C. Xavier, and M. Oliveira, "Effects of low-level laser therapy on bone formed after distraction osteogenesis," Laser Med Sci 25, 213 (2010).

[55] N. Kourkoumelis, and M. Tzaphlidou, "Spectroscopic assessment of normal cortical bone: differences in relation to bone site and sex," Scientific World Journal 10, 402 (2010).

[56] A. Welch, and M. Gemert, "Optical-thermal response of laser-irradiated tissue," Springer Science & Business Media. ISBN: 978-0-306-44926-0 (1995).

[57] S. Lin, L. Wang, S. Jacques, and F. Tittel, "Measurement of tissue optical properties by the use of oblique-incidence optical fiber reflectometry," Appl Opt 36, 136 (1997).

[58] A. Yablon, N. Nishioka, B. Mikic, and V. Venugopalan, "Measurement of tissue absorption coefficients by use of interferometric photothermal spectroscopy," Appl Opt 38, 1259 (1999).

[59] M. Dark, L. Perelman, I. Itzkan, J. Schaffer, and M. Feld, "Physical properties of hydrated tissue determined by surface interferometry of laser-induced thermoelastic deformation," Phys Med Biol 45, 529 (2000).

[60] M. Cloutier, "Healing of calvarial wounds created by Er:YAG laser irradiation in comparison with conventional mechanical and femtosecond laser ablation in presence or absence of BMPs," Master's thesis. Retrieved from University of Toronto (2009).

[61] A. Vogel, and V. Venugopalan, "Mechanisms of pulsed laser ablation of biological tissues, " Chem Rev 103, 577 (2003).

[62] B. Fowler, "Infrared studies of apatites. I. vibrational assignments for calcium, strontium, and barium hydroxyapatites utilizing isotopic substitution," Inorg Chem 13, 194 (1974).

[63] N. Wright, and J. Humphrey, "Denaturation of collagen via heating: an irreversible rate process," Annu Rev Biomed Eng 4, 109 (2002).

[64] A. Aoki, K. Mizutani, A. Takasaki, K. Sasaki, S. Nagai, F. Schwarz, I. Yoshida, T. Eguro, J. Zeredo, and Y. Izumi, "Current status of clinical laser applications in periodontal therapy," Gen Den 56, 674 (2008).

[65] M. Firbank, M. Hiraoka, M. Essenpreis, and D. Delpy, "Measurement of the optical properties of the skull in the wavelength range 650-950 nm," Phys Med Biol 38, 503 (1993).

[66] A. Bashkatov, E. Genina, V. Kochubey, and V. Tuchin, "Optical properties of

human cranial bone in the spectral range from 800 to 2000 nm," Proceedings of the SPIE, 6163, 616310 (2006)

[67] N. Ugryumova, S. Matcher, and D. Attenburrow, "Measurement of bone mineral density via light scattering," Phys Med Biol, 49, 469 (2004).

[68] B. Lange, T. Brendel, and G. Hüttmann, "Temperature dependence of light absorption in water at holmium and thulium laser wavelengths," Appl Opt 41, 5797 (2002).

[69] I. Cilesiz, and A. Welch, "Light dosimetry - effects of dehydration and thermal-damage on the optical properties of the human aorta," Appl Opt 32, 477 (1993).

[70] H. Jellinek, and R. Srinivasan, "Theory of etching of polymers by far-ultraviolet high intensity pulsed laser- and long-term irradiation," J Phys Chem 88, 3048 (1984).

[71] M. Heilmann, "Laser–tissue interactions II." University of Heidelberg. retrieved http://www.umm.uni-heidelberg.de/inst/cbtm/ckm/lehre/basicoptics/6_LASER-Tissue-InteractionsII.pdf (2009).

[72] Berger N, and P. Eeg, "Fundamentals of laser-tissue interaction. in: veterinary laser surgery: a practical guide," Ames, IA: Blackwell 29 (2006).

[73] B. Choi, and A. Welch, "Analysis of thermal relaxation during laser irradiation of tissue," Laser Surg Med 29, 351 (2001).

[74] J. Hayes, and M. Wolbarsht, "Thermal model for retinal damage induced by pulsed lasers," Aerospace Med 39, 474 (1968).

[75] R. Gattass, L. Cerami, and E. Mazur, "Micromachining of bulk glass with bursts of femtosecond laser pulses at variable repetition rates," Opt Express 14, 5279 (2006).

[76] A. Vogel, and V. Venugopalan, "Pulsed laser ablation of soft biological tissues," In optical-thermal response of laser-irradiated tissue. 2nd ed. Springer Science & Business Media. ISBN: 978-9-048-18830-7 (2011).

[77] C. Haffner, M. Folwaczny, R. Hickel, and H. Horch, "Ablation of temporomandibular joint structures of a pig with fiber-guided 308 nm excimer laser light - an in vitro investigation," J Cranio Maxill Surgery 32, 360 (2004).

[78] D. Albagli, "Fundamental mechanisms of pulsed laser ablation of biological tissue," Doctoral thesis. Retrieved from Massachusetts Institute of Technology (1994).

[79] C. Schaffer, A. Brodeur, and E. Mazur, "Laser-induced breakdown and damage in bulk transparent materials induced by tightly focused femtosecond laser pulses," Meas Sci Technol 12, 1784 (2001).

[80] J. Siegel, D. Puerto, W. Gawelda, G. Bachelier, J. Solis, L. Ehrentraut, and J. Bonse,

"Plasma formation and structural modification below the visible ablation threshold in fused silica upon femtosecond laser irradiation," Appl Phys Lett 91, 082902 (2007).

[81] A. Vogel, J. Noack, K. Nahen, D. Theisen, S. Busch, U. Parlitz, D. Hammer, G. Noojin, B. Rockwell, and R. Birngruber, "Energy balance of optical breakdown in water at nanosecond to femtosecond time scales," Appl Phys B 68, 271 (1999).

[82] J. Fischer, T. Juhasz, and J. Bille, "Time resolved imaging of the surface ablation of soft tissue with IR picosecond laser pulses," Appl Phys A Mater Sci Process 64, 181 (1997).

[83] B. Zysset, J. Fujimoto, and T. Deutsch, "Time-resolved measurements of picosecond optical breakdown," Appl Phys B 48, 139 (1989).

[84] P. Byers, "Solitary benign osteoblastic lesions of bone," Cancer 22, 43 (1968).

[85] S. Davidson, and D. James, "Drilling in bone: modeling heat generation and temperature distribution," J Biomech Eng Trans Asme 125, 305 (2003).

[86] A. Eriksson, and T. Albrektsson, "Temperature threshold levels for heat-induced bone tissue injury - A vital microscopic study in the rabbit," J Prosthet Dent 50, 101 (1983).

[87] R. Stern, and R. Sognnaes, "Laser beam effect on dental hard tissues," J Dent Res 43, 873 (1964).

[88] L. Goldman, P. Hornby, R. Mayer, and B. Goldman, "Impact of the laser on dental caries," Nature 203, 417 (1964).

[89] M. Frentzen, W. Gotz, M. Ivanenko, S. Afilal, M. Werner, and P. Hering, "Osteotomy with 80-mu s CO_2 laser pulses - histological results," Lasers Med Sci 18, 119 (2003).

[90] M. Ivanenko, M. Werner, S. Afilal, M. Klasing, and P. Hering, "Ablation of hard bone tissue with pulsed CO_2 lasers," Med Laser Appl, 20, 13 (2005).

[91] R. Boehm, J. Rich, J. Webster, and S. Janke, "Thermal stress effects and surface cracking associated with laser use on human teeth," J Biomech Eng 99, 189 (1977).

[92] S. McCormack, D. Fried, J. Featherstone, R. Glena, and W. Seka, "Scanning electron microscope observations of CO_2 laser effects on dental enamel," J Dent Res 74, 1702 (1995).

[93] M. Forrer, M. Frenz, V. Romano, H. Altermatt, H. Weber, A. Silenok, M. Istomyn, and V. Konov, "Bone-ablation mechanism using CO_2 lasers of different pulse duration and wavelength," Appl Phys B 56, 104 (1993).

[94] A. Rosa, A. Sarma, C. Le, R. Jones, and D. Fried, "Peripheral thermal and mechanical damage to dentin with microsecond and sub-microsecond 9.6 μm, 2.79 μm, and 0.355 μm laser pulses," Lasers Surg Med 35, 214 (2004).

[95] K. Henn, G. Gubaidullin, J. Bongartz, J. Wahrburg, H. Roth, and M. Kunkel, "A spectroscopic approach to monitor the cut processing in pulsed laser osteotomy," Lasers Med Sci 28, 87 (2013).

[96] M. Ivanenko, and P. Hering, "Hard tissue ablation with a mechanically Q-switched CO_2 laser," Proc. SPIE 3565, 110 (1998).

[97] R. George, and L. J. Walsh, "Coaxial water mist spray alters the ablation properties of human radicular dentine for the holmium: YAG laser," J Oral Laser Appl 7, 225 (2007).

[98] D. Fried, N. Ashouri, T. Breunig, and R. Shori, "Mechanism of water augmentation during IR laser ablation of dental enamel," Lasers Surg Med 31, 186 (2002).

[99] D. Fried, J. Featherstone, C. Le, and K. Fan, "Dissolution studies of bovine dental enamel surfaces modified by high-speed scanning ablation with a $\lambda = 9.3$-μm TEA CO_2 Laser," Lasers Surg Med 38, 837 (2006).

[100] L. Kuscer, and J. Diaci, "Measurements of erbium laser-ablation efficiency in hard dental tissues under different water-cooling conditions," J Biomed Opt 18, 108002 (2013).

[101] M. Cardoso, E. Coutinho, R. Ermis, A. Poitevin, K. Landuyt, J. Munck, R. Carvalho, P. Lambrechts, and B. Meerbeek, "Influence of Er,Cr:YSGG laser treatment on the microtensile bond strength of adhesives to dentin," J Adhes Dent. 10, 25 (2008).

[102] A. Tachibana, M. Marques, J. Soler, and A. Matos, "Erbium, chromium:yttrium scandium gallium garnet laser for caries removal: influence on bonding of a self-etching adhesive system," Lasers Med Sci 23, 435 (2008).

[103] M. AbuSerriah, H. Critchlow, C. Whitters, and A. Ayoub, "Removal of partially erupted third molars using an erbium (Er):YAG laser: A randomized controlled clinical trial," Br J Oral Maxillofac Surg 42, 203 (2004).

[104] M. Niemz, L. Eisenmann, and T. Pioch, "Vergleich von drei lasersystemen zur abtragung von," Zahnschmelz. Schweiz. Monatsschr. Zahnmed. 103, 1252 (1993).

[105] S. Corona, A. Souza, M. Chinelatti, M. Borsatto, J. Pecora, and R. Palma-Dibb, "Effect of energy and pulse repetition rate of Er: YAG laser on dentin ablation ability and morphological analysis of the laser-irradiated substrate," Photomed Laser Surg 25, 26 (2007).

[106] T. Harashima, J. Kinoshita, Y. Kimura, A. Brugnera, F. Zanin, J. Pecora, and K.

Matsumoto, "Morphological comparative study on ablation of dental hard tissues at cavity preparation by Er:YAG and Er,Cr:YSGG lasers," Photomed Laser Surg 23, 52 (2005).

[107] A. Charlton, M. Dickinson, T. King, and A. Freemont, "Erbium-YAG and holmium-YAG laser ablation of bone," Lasers Med Sci 5, 365 (1990).

[108] N. Fried, and D. Fried, "Comparison of Er:YAG and 9.6-um TE CO_2 lasers for ablation of skull tissue," Lasers Surg Med 28, 335 (2001).

[109] K. Sasaki, A. Aoki, S. Ichinose, and I. Ishikawa, "Ultrastructural analysis of bone tissue irradiated by Er:YAG laser," Lasers Surg Med 31, 322 (2002).

[110] V. Armengol, A. Jean, and D. Marion, "Temperature rise during Er:YAG and Nd:YAP laser ablation of dentin," J Endod 26, 138 (2000).

[111] H. Kang, and A. Welch, "Effect of liquid thickness on laser ablation efficiency," J Appl Phys 101, 083101 (2007).

[112] E. Sinofsky, "Comparative thermal modeling of Er:YAG, Ho:YAG and COP laser pulses for tissue vaporization," SPIE Lasers in Medicine 712, 188 (1986).

[113] V. Romano, R. Rodriguez, H. Altermatt, M. Frenz, and H. Weber, "Bone microsurgery with IR-lasers: a comparative study of the thermal action at different wavelengths," Proc SPIE 2077, 87 (1994).

[114] M. Niemz, "Cavity preparation with the Nd:YLF picosecond laser," J Dent Res 74, 1194 (1995).

[115] R. Nuss, R. Fabian, R. Sarkar, and C. Puliafito, "Infrared laser bone ablation," Lasers Surg Med 8, 381 (1988).

[116] B. Gaspirc, and U. Skaleric, "Morphology, chemical structure and diffusion processes of root surface after Er:YAG and Nd:YAG laser irradiation," J Clin Periodontol 28, 508 (2001).

[117] M. Ariyaratnam, M. Wilson, and A. Blinkhorn, "An analysis of surface roughness, surface morphology and composite/dentin bond strength of human dentin following the application of the Nd:YAG laser," Dent Mater J 15, 223 (1999).

[118] T. Obara, E. Munin, E. Libert, E. Pompeu, and M. Pacheco, "XeCl excimer laser ablation of rabbit tibia bone: morphology of the irradiated site and self-limiting effect," Photomed Laser Surg 23, 561 (2005).

[119] L. Yow, J. Nelson, and M. Berns, "Ablation of bone and polymethylmethacrylate by an XeCl (308 nm) excimer laser," Lasers Surg Med 9, 141 (1989).

[120] R. Sarkar, R. Fabian, R. Nuss, and C. Puliafito, "Plasma-mediated excimer laser

ablation of bone: a potential microsurgical tool," Am J Otolaryngol 10, 76 (1989).

[121] B. Kim, M. Feit, A. Rubenchik, E. Joslin, P. Celliers, J. Eichler, and L. Silva, "Influence of pulse duration on ultrashort laser pulse ablation of biological tissues," J Biomed Opt 6, 332 (2001).

[122] M. Silva, M. Wehner, P. Cde, F. Lampert, R. Poprawe, M. Hermans, and M. Esteves-Oliveira, "Precise ablation of dental hard tissues with ultra-short pulsed lasers. Preliminary exploratory investigation on adequate laser parameters," Lasers Med Sci 28, 171 (2013).

[123] D. Stern, R. Schoenlein, C. Puliafito, E. Dobi, R. Birngruber, and J. Fujimoto, "Corneal ablation by nanosecond, picosecond, and femtosecond lasers at 532 and 625 nm," Arch Ophthalmol, 107, 587 (1989).

[124] M. Strassl, V. Wieger, D. Brodoceanu, F. Beer, A. Moritz, and E. Wintner, "Ultra-short pulse laser ablation of biological hard tissue and biocompatibles," J Laser Micro Nanoen 3, 30 (2008).

[125] A. Rode, E. Gamaly, B. Davies, B. Taylor, M. Graessel, J. Dawes, A. Chan, R. Lowe, and P. Hannaford, "Precision ablation of dental enamel using a subpicosecond pulsed laser," Aust Dent J 48, 233 (2003).

[126] M. Fahey, O. Onyejekwe, H. Mason, and K. Mitra, "Precise dental ablation using ultra-short-pulsed 1552 nm laser," Int J Heat Mass Transfer 51, 5732 (2008).

[127] L. Cangueiro, and R. Vilar, "Influence of the pulse frequency and water cooling on the femtosecond laser ablation of bovine cortical bone," Appl Surf Sci 283, 1012 (2013).

[128] C. Plotz, F. Schelle, C. Bourauel, M. Frentzen, and J. Meister, "Ablation of porcine bone tissue with an ultrashort pulsed laser (USPL) system," Lasers Med Sci 30, 977 (2015).

[129] T. Petrov, E. Pecheva, A. Walmsley, and S. Dimov, "Femtosecond laser ablation of dentin and enamel for fast and more precise dental cavity preparation," Mater Sci Eng C 90, 433 (2018).

[130] J. Neev, L. Silva, M. Feit, M. Perry, A. Rubenchik, and B. Stuart, "Ultrashort pulse lasers for hard tissue ablation," IEEE J Sel Top Quantum Electron 2, 790 (1996).

[131] Q. Le, R. Vilar, and C. Bertrand, "Influence of external cooling on the femtosecond laser ablation of dentin," Lasers Med Sci 32, 1943 (2017)..

[132] J. Liu, "High energy all fiber mode locked fiber laser," U.S. Patent No. US7907645B1, (2011).

[133] S. Gavrilov, D. Golishnikov, V. Gordienko, A. Savelev, and R. Volkov, "Efficient hard x-ray source using femtosecond plasma at solid targets with a modified surface," Laser and Particle Beams 22, 301 (2004).

[134] C. Serbanescu, J. Chakera, and R. Fedosejevs, "Efficient Ka x-ray source from submillijoule femtosecond laser pulses operated at kilohertz repetition rate," Rev. Sci. Instrum. 78, 103502 (2007).

[135] J. Yu, Z. Jiang, J. Kieffer, and A. Krol, "Hard x-ray emission in high intensity femtosecond laser-target interaction," Physics of Plasmas, 6, 1318 (1999).

[136] Newport. Gaussian Beam Optics, retrieved http://www.rpgroup.caltech.edu/courses/aph162/2007/Protocols/Optics/e3872_Gaussian-Beam Optics.pdf

[137] G. Khader, "Ultrashort laser ablation of cortical bone: literature review and experimental evaluation," Master's thesis. Retrieved from Mcmaster University (2013).

[138] B. Yakar, and R. Byer, "Femtosecond laser ablation properties of borosilicate glass," J Appl. Phys. 96, 5316 (2004).

[139] D. Giguère, G. Olivié, F. Vidal, S. Toetsch, G. Girard, T. Ozaki, J. Kieffer, O. Nada, and I. Brunette, "Laser ablation threshold dependence on pulse duration for fused silica and corneal tissues: experiments and modeling," JOSA A 24, 1562 (2007).

[140] N. Sanner, O. Utéza, B. Bussiere, G. Coustillier, A. Leray, T. Itina, and M. Sentis, "Measurement of femtosecond laser-induced damage and ablation thresholds in dielectrics," Appl. Phys. 94, 889 (2009).

[141] B. Kim, M. Feit, A. Rubenchik, E. Joslin, P. Celliers, J. Eichler, and L. Silva, "Influence of pulse duration on ultrashort laser pulse ablation of biological tissues," J Biomed Opt 6, 332 (2001).

[142] A. Murray, and M. Dickinson, "Tissue ablation-rate measurements with a long-pulsed, fibre-deliverable 308 nm excimer laser," Lasers in Medical Science 19, 127 (2004).

[143] G. Olivié, D. Giguère, F. Vidal, V. Ozaki, J. Kieffer, O. Nada, and I. Brunette, "Wavelength dependence of femtosecond laser ablation threshold of corneal stroma," Optics Express 16, 4121 (2008).

[144] J. Liu, "Simple technique for measurements of pulsed Gaussian beam spot sizes," Opt. Lett. 7, 196 (1982).

[145] Y. Jee, M. Becker, and R. Walser, "Laser-induced damage on single-crystal metal surfaces," J. Opt. Soc. Am. B 5, 648 (1988).

[146] B. Emigh, J. Hayward, R. An, E. Hsu, T. Crawford, H. Haugen, G. Wohl, and Q. Fang, "Porcine cortical bone ablation by ultrashort pulsed laser irradiation," Journal of Biomedical Optics 17, 028001 (2012).

[147] B. Kim, M. Feit, A. Rubenchik, E. Joslin, J. Eichler, P. Stoller, and L. Silva, "Effects of high repetition rate and beam size on hard tissue damage due to subpicosecond laser pulses," Appl Phys Lett 76, 4001 (2000).

[148] G. Nicolodelli, F. Lizarelli, and V. Bagnato, "Influence of effective number of pulses on the morphological structure of teeth and bovine femur after femtosecond laser ablation," J. Biomed. Opt. 17, 048001 (2012).

[149] B. Christensen, and P. Balling, "Modeling ultrashort-pulse laser ablation of dielectric materials," Phys. Rev. B 79, 155424 (2009).

[150] R. An , G. Khadar, E. Wilk, B. Emigh, H. Haugen, G. Wohl, B. Dunlop, M. Anvari, J. Hayward, and Q. Fang, "Ultrafast laser ablation and machining large-size structures on porcine bone," J Biomed Opt. 18, 70504 (2013).

[151] A. Daskalovaa, S. Bashirb, and W. Husinsky, "Morphology of ablation craters generated by ultra-short laser pulses in dentin surfaces: AFM and ESEM evaluation," Applied Surface Science 257, 1119 (2010)

[152] R. Lizarelli, C. Kurachi, L. Misoguti, and V. Bagnato, "A comparative study of nanosecond and picosecond laser ablation in enamel: morphological aspects," J Clin Laser Med Surg. 18, 151 (2000).

[153] M. Correa, G. Nicolodelli, J. Rodrigues, C. Kurachi, and V. Bagnato, "Femtosecond laser ablation on dental hard tissues analysis of ablated profile near an interface using local effective intensity," Laser Phys 21, 965 (2011).

[154] M. Stafe, C. Negutu, and I. Popescu, "Combined experimental and theoretical investigation of multiple-nanosecond laser ablation of metals," J Optoelectron Adv M 8, 1180 (2006).

[155] R. Lizarelli, M. Costa, E. Filho, F. Nunes, and V. Bagnato, "Selective ablation of dental enamel and dentin using femtosecond laser pulses," Laser Phys. Lett. 5, 63 (2008).

[156] A. Rode, E. Gamaly, B. Davies, B. Taylor, J. Dawes, A. Chan, R. Lowe, and P. Hannaford, "Subpicosecond laser ablation of dental enamel," J. Appl. Phys. 92, 2153 (2002).

[157] H. Kang, I. Rizoiu, and A. Welch, "Hard tissue ablation with a spray-assisted mid-IR laser," Phys. Med. Biol. 52, 7243 (2007).

[158] M. Ivanenko, and P. Hering, "Wet bone ablation with mechanically Q-switched

high-repetition-rate CO_2 laser," Appl. Phys. B 67, 395 (1998).

[159] Q. Fang, and X. Hu, "Modeling of skin tissue ablation by nanosecond," IEEE J. Quantum Electron. 40, 69 (2004).

[160] L. Mortensen, C. Alt, R. Turcotte, M. Masek, T. Liu, D. Côté, C. Xu, G. Intini, and C. Lin, "Femtosecond laser bone ablation with a high repetition rate fiber laser source," Biomed. Opt. Express 6, 32 (2014).

[161] H. Liu, F. Chen, X. Wang, Q. Yang, H. Bian, J. Si, and X. Hou, "Influence of liquid environments on femtosecond laser ablation of silicon," Thin Solid Films. 518, 5188 (2010).

[162] G. Daminelli, J. Kruoger, and W. Kautek, "Femtosecond laser interaction with silicon under water confinement," Thin Solid Films. 467, 334 (2004).

[163] W. Liu, O. Kosareva, I. golubtsov, A. Iwasaki, A. Becker, V. Kandidov, and S. Chin, "Femtosecond laser pulse filamentation versus optical breakdown in H_2O," Appl. Phys. B 76, 215 (2003).

[164] J. Sylvestre, A. Kabashin, E. Sacher, and M. Meunier, "Femtosecond laser ablation of gold in water: influence of the laser-produced plasma on the nanoparticle size distribution," Appl. Phys. A 80, 753 (2005).

[165] V. Tangwarodomnukun, J. Wang, and P. Mathew, "A comparison of dry and underwater laser micromachining of silicon substrates," Key. Eng. Mat. 443, 693 (2010).

[166] C. Tulea, J. Caron, H. Wahab, N. Gehlich, M. Hoefer, D. Esser, B. Jungbluth, A. Lenenbach, and R. Noll, "Highly efficient nonthermal ablation of bone under bulk water with a frequency-doubled Nd:YVO_4 picosecond laser," Proc. SPIE. 8565, 85656 (2013).

[167] H. Chen, H. Li, Y. Sun, Y. Wang, and P. Lü, "Femtosecond laser for cavity preparation in enamel and dentin: ablation efficiency related factors," Sci. Rep. 6, 20950 (2016).

[168] J. Kaakkunen, M. Silvennoinen, K. Paivasaari, and P. Vahimaa, "Water-assisted femtosecond laser pulse ablation of high aspect ratio holes," Phys. Proc. 12, 89 (2011).

[169] A. Tamura, T. Sakka, K. Fukami, and Y. Ogata, "Dynamics of cavitation bubbles generated by multi-pulse laser irradiation of a solid target in water," Appl. Phys. A 112, 209 (2013).

[170] N. Krstulovic, S. Shannon, R. Stefanuik, and C. Fanara, "Underwater laser drilling of aluminum," Int. J. Adv. Manuf. Technol. 69, 1765 (2013).

[171] Q. Le, C. Bertrand, and R. Vilar, "Structural modifications induced in dentin by femtosecond laser," J. Biomed. Opt. 21, 125007 (2016).

[172] L. Ji, L. Li, H. Devlin, Z. Liu, J. Jiao, and D. Whitehead, "Ti:sapphire femtosecond laser ablation of dental enamel, dentine, and cementum," Lasers Med. Sci. 27, 197 (2012).

[173] J. Ren, M. Kelly, and L. Hesselink, "Laser ablation of silicon in water with nanosecond and femtosecond pulses," Opt. Lett. 30, 1740 (2005).

[174] W. Charee, V. Tangwarodomnukun, and C. Dumkum, "Laser ablation of silicon in water under different flow rates," Int. J. Adv. Manuf. Technol. 78, 19 (2015).

[175] B. Emigh, "Experimental evaluation of bone drilling using ultrashort pulsed laser ablation," Master's thesis, Retrieved from McMaster University, 2011.

[176] A. Vorobyev, and C. Guo, "Direct observation of enhanced residual thermal energy coupling to solids in femtosecond laser ablation," Appl. Phys. Lett. 86, 011916 (2005).

[177] H. Scheibe, D. Drescher, and P. Alers, "Raman characterization of amorphous carbon films," Fresenius J Anal Chem. 353, 695 (1995).

[178] S. Eaton, H. Zhang, M. Ng, J. Li, W. Chen, S. Ho, and P. Herman, "Transition from thermal diffusion to heat accumulation in high repetition rate femtosecond laser writing of buried optical waveguides," Opt. Express 16, 9443 (2008).

[179] M. Dewhirst, B. Viglianti, M. Michiels, M. Hanson, and P. Hoopes, "Basic principles of thermal dosimetry and thermal thresholds for tissue damage from hyperthermia," Int. J. Hyperthermia 19, 267 (2003).

[180] R. Gill, Z. Smith, C. Lee, and S. Hogiu, "The effects of laser repetition rate on femtosecond laser ablation of dry bone: a thermal and LIBS study" J Biophotonics. 9, 171 (2016).

[181] J. Radtke, and J. Koenig, "Micromachining with short and ultrashort laser pulses," Stuttgarter Lasertage, 2008.

[182] H. Huang, L. Yang, and J. Liu, "Micro-hole drilling and cutting using femtosecond fiber laser," Optical Engineering 53, 051513 (2014).

[183] S. Soares, N. Gutknecht, G. Conrads, F. Lampert, E. Matson, and C. Eduardo, "The bactericidal effect of Ho:YAG laser irradiation within contaminated root dentinal samples," J Clin Laser Med Surg. 18, 81 (2000).

[184] M. Tyas, K. Anusavice, J. Frencken, and G. Mount, "Minimal intervention dentistry-a review," Int Dent J. 50, 1 (2000).

[185] U. Keller, and R. Hibst, "Experimental studies of the application of the Er:YAG laser on dental hard substances: II. Light microscopic and SEM investigations," Lasers Surg Med. 9, 345 (1989).

[186] D. Menezes, C. Harvey, D. Gerbi, J. Smith, D. Smith, J. Ivaldi, A. Phillips, J. Chan, and S. Hogiu, "Fs-laser ablation of teeth is temperature limited and provides information about the ablated components," J. Biophotonics 10, 1292 (2017).

[187] A. Ancona, F. Röser, K. Rademaker, J. Limpert, S. Nolte, and A. Tünnermann, "High speed laser drilling of metals using a high repetition rate, high average power ultrafast fiber CPA system," Opt. Express 16, 8958 (2008).

[188] S. Döring, A. Ancona, S. Hädrich, J. Limpert, S. Nolte, and A. Tünnermann, "Microdrilling of metals using femtosecond laser pulses and high average powers at 515 nm and 1030 nm," Applied Physics A 100, 53 (2010).

[189] J. Schille, R. Ebert, U. Loeschner, P. Regenfuss, T. Suess, and H. Exner, "Micro structuring with highly repetitive ultra short laser pulses," Proceedings of LPM2008-the 9th International Symposium on Laser Precision Microfabrication (2008).

[190] J. Schille, L. Schneider, L. Hartwig, U. Loeschner, R. Ebert, P. Scully, N. Goddard, and H. Exner, "Characterisation of interaction phenomena in high repetition rate femtosecond laser ablation of metals," 31st International Congress on Applications of Lasers & Electro-Optics (ICALEO), At Anaheim, Ca. (USA) (2012).

[191] F. Schelle, S. Polz, H. Haloui, A. Braun, C. Dehn, M. Frentzen, and J. Meister, "Ultrashort pulsed laser (USPL) application in dentistry: basic investigations of ablation rates and thresholds on oral hard tissue and restorative materials," Lasers Med Sci. 26, 1775 (2014).

[192] H. Chen, J. Liu, H. Li, W. Ge, Y. Sun, Y. Wang, and P. Lü, "Femtosecond laser ablation of dentin and enamel: relationship between laser fluence and ablation efficiency," J. Biomed. Opt. 20, 28004 (2015).

[193] B. Sallé, O. Gobert, P. Meynadier, M. Perdrix, G. Petite, and A. Semerok, "Femtosecond and picosecond laser microablation: ablation efficiency and laser microplasma expansion," Appl. Phys. A 69, S381 (1999).

[194] F. Korte, S. Adams, A. Egbert, C. Fallnich, A. Ostendorf, S. Nolte, M. Will, J. Ruske, B. Chichkov, and A. Tuennermann, "Sub-diffraction limited structuring of solid targets with femtosecond laser pulses," Optics Express 7, 4 (2000).

[195] G. Willems, P. Lambrechts, M. Braem, and M. Vanherle, "The surface roughness of enamel-to-enamel contact areas compared with the intrinsic roughness of dental resin composites," J Dent Res. 70, 1299 (1991).

[196] D. Gerke, "Pulpal integrity of anterior teeth treated with composite resins. A long-

term clinical evaluation," Aust. Dent. J. 33, 133 (1988).

[197] V. Armengol, O. Laboux, P. Weiss, A Jean, and H. Hamel, "Effects of Er:YAG and Nd:YAP laser irradiation on the surface roughness and free surface energy of enamel and dentin: an in vitro study," Oper Dent. 28, 67 (2003).

[198] K. Ozono, and M. Obara, "Tailored ablation processing of advanced biomedical hydroxyapatite by femtosecond laser pulses," Appl. Phys. A 77, 303 (2003).

[199] O. Kazue, O. Minoru, and S. Jun, "Ablation processing of biomedical materials by ultrashort laser pulse ranging from 50 fs through 2 ps," Proceedings of the SPIE 4978, 208 (2003).

[200] D. Devi, M. Shekhar, and A. Ahmad, "Energy dispersive x-ray analysis of bovine bone," International Journal of Science, Environment and Technology 5, 2616 (2016).

[201] Y. Kimura, D. Yu, A. Fujita, A. Yamashita, Y. Murakami, and K. Matsumoto, "Effects of Erbium,Chromium:YSGG laser irradiation on canine mandibular bone," J Periodontol. 72, 1178 (2001).

[202] Z. Junbiao, L. Yonggui, L. Nianqing, Z. Guoqing, W. Minkai, W. Gan, Y. Xuepin, H. Yuying, H. Wei, D. Ynmei, and G. Xuejun, "Primary experimental studies on mid-infrared FEL irradiation on dental substances at BFEL," Nuclear Instruments and Methods in Physics Research A 475, 630 (2001).

[203] S. Kuroda, and B. Fowler, "Compositional, structural, and phase changes in in vitro laser-irradiated human tooth enamel," Calcif Tissue Int. 36, 361 (1984).

[204] B. Fowler, and S. Kuroda, "Changes in heated and in laser-irradiated human tooth enamel and their probable effects on solubility," Calcif Tissue Int. 38, 197 (1986).

[205] M. Kozielski, T. Buchwald, M. Szybowicz, Z. Blaszczak, A. Piotrowski, and B. Ciesielczyk, "Determination of composition and structure of spongy bone tissue in human head of femur by Raman spectral mapping," J Mater Sci Mater Med. 22, 1653 (2011).

[206] V. Dritsa, D. Sgouros, K. Pissaridi, P. Bochlogyros, M. Kyriakidou, and V. Mamareli, "Enamel structure on children with down syndrome - an FT-IR spectroscopic study, in: theophile th (ed.), infrared spectroscopy - anharmonicity of biomolecules, crosslinking of biopolymers, food quality and medical applications," InTech Open, Croatia, ch6 (2015).

[207] T. Cangueiro, R.Vilar, A. Rego, and V. Muralha, "Femtosecond laser ablation of bovine cortical bone," J Biomed Opt. 17, 125005 (2012).

[208] T. Lippert, E. Ortelli, J. Panitz, F. Raimondi, J. Wambach, J. Wei, and A.Wokaun,

"Imaging-XPS/Raman investigation on the carbonization of polyimide after irradiation at 308 nm," Appl. Phys. A 69, S651 (1999).

[209] J. Hoke, E. Burkes, E. Gomes, and M. Wolbarsht, "Erbium:YAG (2.94 um) laser effects on dental tissues," J. Laser Appl. 2, 61 (1990).

[210] H. Kang, H. Lee, S. Chen, and A. Welch, "Enhancement of bovine bone ablation assisted by a transparent liquid layer on a target surface," IEEE J. Quantum Elect. 42, 633 (2006).

[211] H. Kang, J. Oh, and J. Welch, "Investigations on laser hard tissue ablation under various environments," Phys. Med. Biol. 53, 3381 (2008).

[212] G. Daminelli, J. Kruger, and W. Kautek, "Femtosecond laser interaction with silicon under water confinement," Thin Solid Films 467, 334 (2004).

[213] S. Zhu, Y. Lu, M. Hong, and X. Chen, "Laser ablation of solid substrates in water and ambient air," J. Appl. Phys. 89, 2400 (2001).

[214] L. Andrade, J. Pelino, R. Lizarelli, V. Bagnato, and O. Oliveira, "Caries resistance of lased human enamel with Er:YAG laser – morphological and ratio Ca/P analysis," Laser Phys. Lett. 4, 157 (2007).

[215] D. Strickland and G. Mourou, "Compression of amplified chirped optical pulses," Optics Communications 55, 447 (1985).